DEVELOPING AN OPTIMAL EMS FOR A FUEL CELL ELECTRIC VAN

DEVELOPING AN OPTIMAL AND REAL-TIME IMPLEMENTABLE ENERGY MANAGEMENT SYSTEM FOR A FUEL CELL ELECTRIC VAN WITH ENHANCED FUEL CELL AND BATTERY LIFE AND PERFORMANCE

By TIAGO SUEDE MIRANDA, BS

A Thesis Submitted to the School of Graduate Studies in Partial Fulfillment of the Requirements for the Degree Master of Applied Science

McMaster University

MASTER OF APPLIED SCIENCE (2024)

Hamilton, Ontario, Canada (Mechanical Engineering)

TITLE:	Developing an Optimal and Real-time Implementable Energy Management System for a Fuel Cell Electric Van with Enhanced Fuel Cell and Battery Life and Performance
AUTHOR:	Tiago Suede Miranda BS (Mechanical Engineering), McMaster University, Hamilton, Canada
SUPERVISOR:	Ali Emadi
NUMBER OF PAGES:	xx, 177

Abstract

This research presents a two-part study on a fuel cell electric van (FCEV), focusing on vehicle modeling and developing different control strategies for the modeled vehicle.

The modelling phase accounts for the aging effects on the fuel cell (FC) and battery, analyzing FCEV behavior over time. This includes estimating and integrating the degradation impacts on characteristic curves, such as the FC's polarization and efficiency curves, the battery's charging and discharging resistance curves, and the open-circuit voltage curve. A simplified fuel cell system (FCS) model is designed to consider power losses in multiple components, including the FC stack, air compressor, and others. The dynamic limits of the FC are also included to yield more realistic results. The model is based on the vehicle Opel Vivaro FC specifications, incorporating parameters like maximum FC power, battery capacity, vehicle weight, and tire dimensions.

Subsequently, various control strategies are applied to analyze their effectiveness in FC and battery State-of-Health (SOH) degradation and hydrogen consumption. A rule-based energy management system (EMS) is implemented first, which operates with five different operational modes dependent on the vehicle's state. This is followed by a look-up table (LUT) based strategy, which uses two two-dimensional tables generated by a Neural Network (NN). The network is trained with discretized optimal

trajectories derived from dynamic programming (DP) code developed based on the modelled FCEV. The DynaProg MATLAB toolbox is used to develop the code.

The study concludes by comparing the results of these strategies in terms of components' SOH degradations and hydrogen consumption.

Dedicated to Justino, Tania, Lorena, and Dom.

Acknowledgements

Firstly, I want to thank Jesus Christ, who has guided me along my master's journey and my life.

I want to thank my academic supervisor, Dr. Ali Emadi, for the leadership and the unique opportunity to come to the McMaster Automotive Resource Centre to pursue my master's studies; such a special place filled with talented and unique people who have helped me grow professionally and as a human being and have rekindled some of my childhood dreams.

Thank you to my parents and sister, who have supported me daily and done everything possible to provide me with the best principles and education.

I also want to thank Dr. Paula Frassinetti Cavalcante and her research group for the opportunity to join them. Her encouragement, the experiences they provided, and their support were essential for me to come to MARC.

I am also thankful to Dr. Biswas for his insights and support.

A special thanks goes to Hao Wang for his constant support since the beginning of my master's, with a collaborative spirit, encouraging words, patience, academic support, and friendship along this journey.

Thank you to the friends and colleagues inside and outside MARC who have supported me in these two years.

This research was undertaken, in part, thanks to funding from the Natural Sciences and Engineering Research Council of Canada (NSERC) and Canada Research Chair in Transportation Electrification and Smart Mobility.

Table of Contents

List of Figures

List of Tables

Notation, Definitions, and Abbreviations

Abbreviations

ANL	Argonne National Laboratory
BEV	Battery Electric Vehicle
BOL	Beginning-of-Life
CDCS	Charge-depleting-Charge-sustaining
CTCBC	China Typical City Bus Cycle
DOE	Department of Energy
DDPG	Deep Deterministic Policy Gradient
DP	Dynamic Programming
DQN	Deep Q-Network
ECSA	Electrochemically Active Surface Area

EM	Electric Motor
EMS	Energy Management System
EOL	End-of-Life
EV	Electric Vehicle
FC	Fuel Cell
FCB	Fuel Cell Electric Bus
FCS	Fuel Cell system
FCEV	Fuel Cell Electric Vehicle
FLC	Fuzzy Logic Controller
GA	Genetic Algorithm
HEV	Hybrid Electric Vehicle
HWFET	Highway Fuel Economy Test
ICE	Internal Combustion Engine
LHV	Lower Heating Value
LUT	Look-up Table
NEDC	New European Driving Cycle
NREL	National Renewable Energy Laboratory
OCV	Open Circuit Voltage

PEMFC	Polymer Electrolyte Membrane Fuel Cell
PID	Proportional-Integral-Derivative
PMP	Pontryagin's Minimum Principle
RIPPER	Repeated Incremental Pruning to Produce Error Reduction
SMES	Superconducting Magnetic Energy Storage
SOC	State-of-Charge
SOH	State-of-Health
TD3	Twin Delayed Deep Deterministic Policy Gradient
UDDS	Urban Dynamometer Driving Schedule
WLTP	Worldwide Harmonized Light Vehicle Test Procedure

Chapter 1

Introduction

1.1 Background and motivations

The transportation sector is a significant contributor to global environmental pollution [4]. The combustion of fossil fuels within this sector releases numerous pollutants that affect the global environment and public health [5]. Therefore, it is necessary to find solutions to overcome this problem.

Rapid advancements in vehicle component technology have boosted interest in adopting electrified vehicles in recent years [6]. Notably, advances in battery technology have led to substantial reductions in the cost of Electric Vehicles (EVs) [7]. For instance, the 'cell to pack' cost ratio, which compares the price of battery cells alone to the complete battery pack price — including costs related to housing, cooling, and safety components — has steadily decreased [8]. This trend is expected to continue until at least 2030 [8]. Consequently, these developments support the ongoing expansion of electrified vehicle adoption.

Fuel Cell Electric Vehicles (FCEVs) are a promising solution in the electrified vehicle market. Although Hybrid Electric Vehicles (HEVs) emit fewer pollutants than conventional Internal Combustion Engine (ICE) vehicles, they still produce greenhouse gases during operation. Besides, fully EVs require large battery packs, for which the disposal is still concerning [9] and needs longer recharging than HEVs and FCEVs [10] [11]. Thus, FCEVs offer considerable advantages, including quick refuelling time, smaller battery packs and higher energy density compared to fully EVs, and no tailpipe emissions compared to HEVs.

Further, it can be seen the continuous growth of investments in FCEVs. In Canada, for example, FCEVs have faced an interest increase. Companies such as Nikola and Toyota are establishing partnerships across the country [12] [13], indicating that growth in the number of FCEVs in the market must happen in the following years. In recent years, Stellantis has developed and introduced the Opel Vivaro Fuel Cell (FC), used as a reference to model the FC electric van in the present study.

Nevertheless, FCEVs have drawbacks and challenges ahead. The production process for hydrogen fuel is yet to be improved [14], as the pollutant methods are predominant. Moreover, the FC degradation still being an issue. Among the main causes, the FC sensitivity to rapid power fluctuations can lead to significant operational degradation [15], limiting the power fluctuations the FC can suffer. Furthermore, a study made by the National Renewable Energy Laboratory (NREL) a few years ago [16] on more than 230 vehicles revealed an operational lifespan of the investigated models typically being between 1,500 to 2,000 hours, which is far from the Department of Energy (DOE) target of 8,000 operational hours for FCEVs [16]. These findings reveal the need for ongoing improvements in FCEV technology and more studies on

improving these systems' longevity.

Lastly, the hydrogen infrastructure is still in its early stages. In North America, most refuelling stations are located in California, while in Canada, they are mainly found in Vancouver, but even in these locations, few are available [17]. Expanding the infrastructure and increasing the range of FCEVs will help to reduce range anxiety, making FCEVs more appealing to customers.

1.2 Thesis contributions

The contributions of this thesis can be summarized as follows:

1) A comprehensive summary of the main FCEV architectures examined in the literature.

2) The development of an FCEV model featuring an FC/battery topology capable of estimating hydrogen consumption and the degradation of the FC and the battery.

3) The implementation of dynamic performance curves within the model to account for changes in FC and battery performance over their respective lifespans.

4) A review of publications focusing on applying rule-based and Dynamic Programming (DP) Energy Management Systems (EMSs) in FCEVs with an FC/battery topology.

5) The development and integration of a real-time, rule-based strategy within the FCEV model.

6) The development and implementation of a look-up table (LUT) based, real-time EMS within the FCEV model.

7) Estimation of range decay and operational hour limits in the modelled FCEV as the FC and battery degrade while the vehicle is controlled by each of the two

developed real-time control strategies.

1.3 Thesis outline

The outline of the proposed study is organized as follows:

Chapter 2 introduces various topologies for FCEV powertrains, as documented in the existing literature. This chapter explores different ways FCs can be integrated with other devices within FCEVs. It discusses the advantages and disadvantages of each topology and provides specifications of real FCEVs, both from past production and current models.

Chapter 3 delves into the modelling of a proposed FCEV minivan. It estimates the decay of the FC and battery State-of-Health (SOH), as well as the hydrogen consumption of the vehicle. This chapter details how the performance curves of the FC and battery change as their SOH deteriorates. These curves, which include charging and discharging resistance, Open Circuit Voltage (OCV) of the battery, efficiency curves of the FC, and polarization curves, are crucial for later estimates of range depletion and the FC's and battery's degradation over time under various EMSs.

Three models are utilized. The first two models generate LUTs used in the third model. The third model is the main model developed for the FCEV. Fig. 1.1 illustrates this logic.

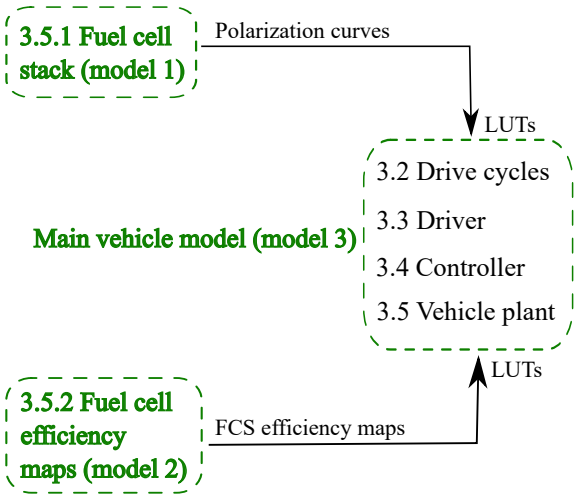

Figure 1.1: Detailed modelling of a fuel cell electric van fluxogram

Chapter 4 presents a literature review of EMSs applied to FCEVs, focusing on rule-based and DP approaches for vehicles with an FC/battery topology — the topology utilized in this study. It also highlights significant findings from other researchers.

Chapter 5 describes the EMSs developed for the modelled FCEV. It introduces two real-time implementable strategies: One based on operation modes and another using LUTs derived from DP code results. A feed-forward Neural Network (NN) is presented, which uses the DP results as training samples to create the mentioned LUTs. The chapter then examines the impact of these EMSs on FC and battery SOH degradation and hydrogen consumption by applying them to the main vehicle model discussed in Chapter 3.

The modelled FCEV is operated until the FC reaches its End-of-Life (EOL). During this period, the vehicle's operational hours and the decrease in range due to aging are analyzed. A flowchart illustrating the main steps described in this chapter

is presented in fig. 1.2.

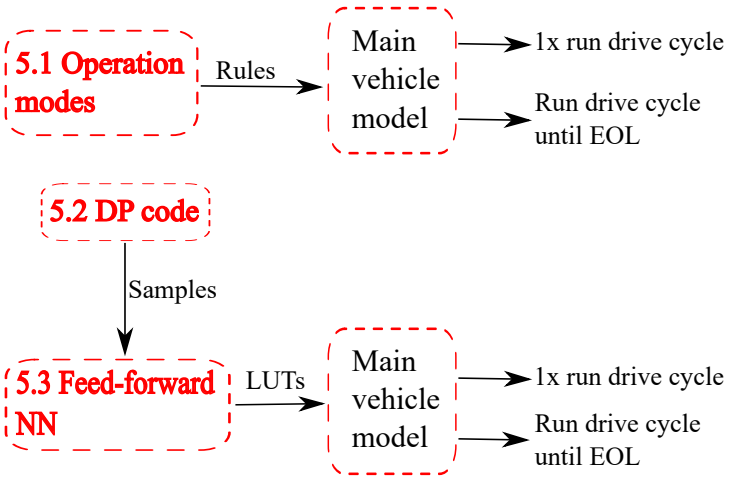

Figure 1.2: State-of-health aware energy management system for the fuel cell electric van fluxogram

Chapter 6 concludes the study by summarizing the main findings and suggesting areas for future research.

Chapter 2

Fuel cell electric vehicle architectures

Distinct FCEVs architectures have undergone investigation since their introduction into automotive powertrains. The literature predominantly recognizes integrating an FC with a high-voltage battery as the most used configuration in real FCEVs, even though integrating with another component also has distinct advantages. Besides, the integration with ultracapacitors (or supercapacitors) is constantly investigated in the literature. When faced with the choice between employing a battery or an ultracapacitor, it becomes evident that batteries exhibit a higher specific energy than ultracapacitors, enabling them to deliver additional power over an extended duration. On the other hand, ultracapacitors demonstrate superior specific power, heightened efficiency, and an extended operational lifespan as indicated by their superior number of charge and discharge cycles before reaching the EOL [18]. A general FC powertrain configuration scheme can be seen in fig. 2.1.

Furthermore, as shown in fig. 2.1, numerous topologies are documented in the

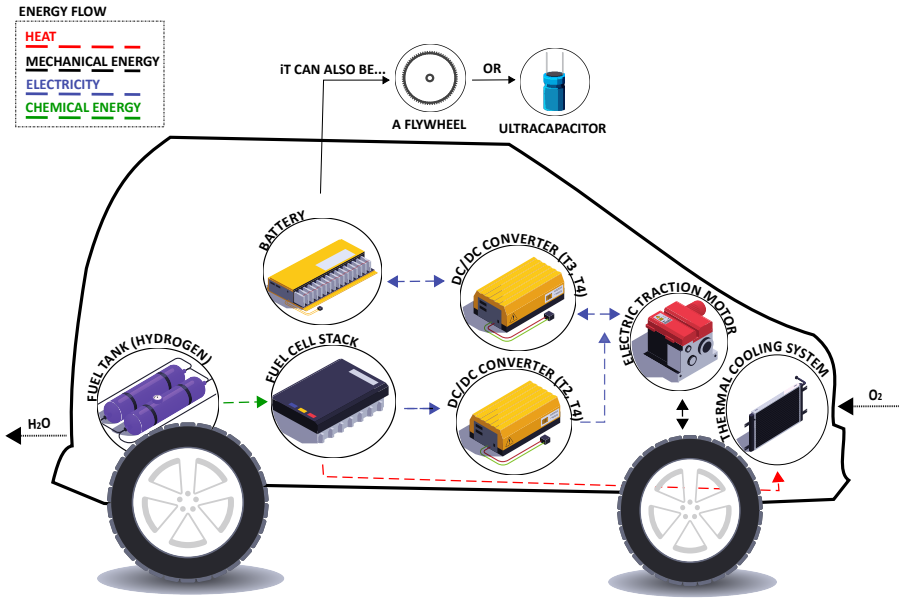

Figure 2.1: FCEVs with 2 energy sources

literature, demonstrating how an FC stack can be integrated with various devices. These configurations include combinations with batteries and supercapacitors, flywheels, and photovoltaic systems. Some topologies may be found with a standalone FC stack [19].

2.1 Full FCEV

A powertrain featuring a standalone FC stack, often called a 'full FCEV', offers several advantages. These include an extended driving range, quick refuelling capacity, cold-start functionality, and low emissions. Such attributes make it suitable for specific applications, including low-speed vehicles like forklifts, buses, airline ground support vehicles, trams, and marine vessels.

2.2 Fuel cell/Ultracapacitor topology

When the FC is integrated with an ultracapacitor, the ultracapacitor only assists the FC during transient power demands when sudden changes occur. Due to the ultracapacitors' relatively low energy density, they are not used as a permanent energy source [19].

2.3 Fuel cell/Flywheel topology

Beyond the configurations discussed previously, integrating flywheels with an FC stack is also feasible. In this setup, the FC stack is the primary energy source, while the flywheel acts as a mechanical energy storage device operating at high rotational speeds. This stored mechanical energy is converted to electrical energy through a generator, which supports the electric motor (EM) during high-energy demands. Flywheels are notable for their high efficiency, rapid charging capabilities, and significant power output, surpassing conventional batteries. Additionally, they are environmentally beneficial, offering a broad operational temperature range, robust energy storage capacity, and an extended operational lifespan [19].

However, combining flywheels with an FC stack generally does not yield the best fuel economy compared to configurations that use ultracapacitors or batteries [20].

2.4 Fuel cell/Superconducting magnetic energy storage topology

The prospect of integrating superconducting magnetic energy storage (SMES) with FCs has also garnered consideration for potential applications in FCEVs. Although its implementation has not been explored much in FCEVs, it should be subjected to more rigorous inspection in the forthcoming years [19]. Regarding its operational principles, SMES stores energy via a magnetic field generated by a direct current that flows through a superconducting coil. SMES has shorter charging and discharging times when compared to alternative energy storage technologies. However, the high cost associated with SMES currently imposes constraints on its practical application within FCEV powertrains [19].

2.5 Fuel cell/Battery topology

The hybridization of FCs and Batteries represents the most used topology. In the most conventional configuration, the FC connects to the DC bus via a unidirectional DC-DC converter (in literature, cases without a DC/DC converter can be found), while the battery may or may not be coupled to a bi-directional DC-DC converter, depending on the nominal voltages of the battery pack and the EM. This topology can be seen in vehicles such as the 2016 Toyota Mirai [21], the Honda Clarity FC, and the Opel Vivaro minivan, shown in fig. 2.2 [1], the car used as reference in this thesis. In the operational process of FC and battery hybridization, an attractive characteristic is that a startup with the battery prevents the FC from operating within a low-efficiency operating range [19].

Figure 2.2: Opel Vivaro FC [1]

Fuel cell/battery FCEVs can be further categorized into four primary types, depending on the presence and location of a DC/DC converter within the system, classified as T1, T2, T3, or T4. In the T1 category, no DC/DC converter is integrated; the T2 includes a single DC/DC converter between the Fuel Cell System (FCS) and the DC bus; the T3 uses a solitary DC/DC converter positioned after the battery. Finally, the fourth configuration (T4) incorporates two DC/DC converters positioned after the battery and the [22].

The T2 topology is widely adopted because it facilitates efficient power distribution between the battery and the FC, while the T3 topology is associated with higher losses than the T2 configuration [22].

2.6 Fuel cell/Battery/Ultracapacitor topology

Topologies with three energy sources, as shown in fig. 2.3, can also be found in the literature. The concurrent integration of a battery and an ultracapacitor alongside the FC is also studied. In the Fuel cell/Battery/Ultracapacitor topology, the FC

connects with the DC bus through a unidirectional DC-DC converter, while both the battery and the ultracapacitor access the DC bus via bidirectional DC-DC converters. This configuration offers enhanced energy density, quick dynamic response, and the capacity for energy regeneration. However, it is complex to implement, and developing control strategies is challenging [23] [24].

2.7 Fuel cell/Battery/photovoltaic panels topology

An additional architectural configuration involves the integration of an FC stack and a battery with photovoltaic panels. In this architecture, the FC serves as the primary energy source, while the panels assume the role of an auxiliary energy generator. The FC and the panels are connected to the DC bus via unidirectional converters, while the battery is connected to the DC bus using a bidirectional converter.

It is important to note that the power output from the photovoltaic panels is subject to variations based on factors such as solar radiation intensity, temperature, and orientation. Furthermore, it is worth mentioning that the photovoltaic panels can either directly power the EM or charge the battery [19].

Besides the physical factors, multiple considerations exist when selecting the optimal architectural configuration for a given application. Key parameters encompassing performance, fuel efficiency, and powertrain costs must be carefully assessed. In a previous study, these three parameters were incorporated into an objective function to investigate the most favourable choice among the FC/battery, FC/ultracapacitor, and FC/battery/ultracapacitor topologies. The resultant conclusion suggests that the

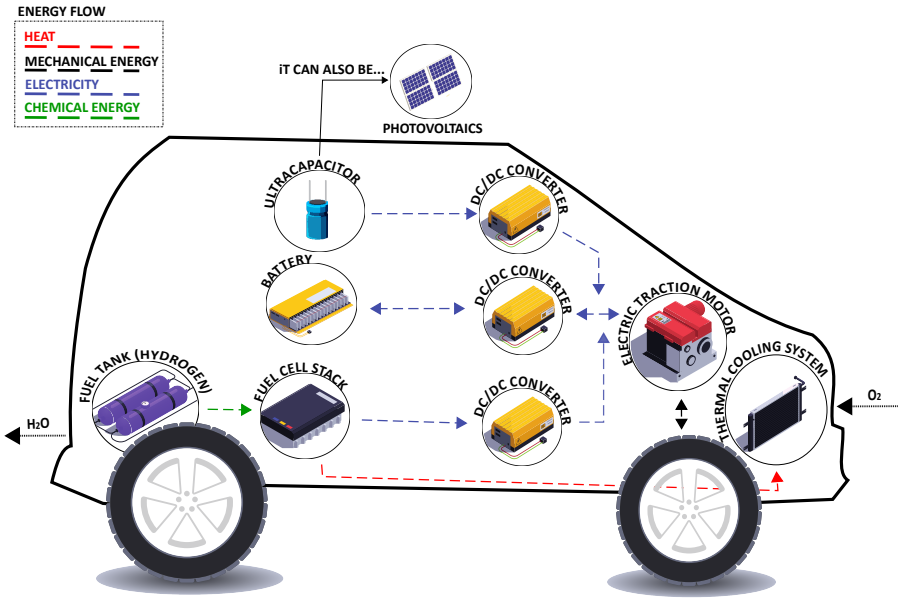

Figure 2.3: FCEVs with 3 energy sources

FC/battery and FC/battery/ultracapacitor configurations emerge as closely competing options, with the former exhibiting lower cost implications and the latter displaying superior fuel economy [18]. This investigation was conducted many years ago, but the fact is that nowadays, most FCEVs produced use the fuel cell/battery topology, even though the size of each energy source can vary widely. Therefore, this is the topology under investigation in this thesis.

Table 2.1 displays various specifications of FCEVs currently in production. This selection includes passenger cars and duty-focused vehicles, such as the American long-haul truck Nikola FCEV and the Opel Vivaro.

It can be observed that even for vehicles of similar sizes, FC stacks typically have a maximum power output exceeding 100 kW. However, the Opel Vivaro deviates from this trend. Some factors justify this deviation. The first is because its powertrain can be integrated into the existing battery electric vehicle (BEV) platform of the BEV

Vehicle	**Fuel cell**	**Battery**	**Range**	**Price**	**Reference**
Opel Vivaro	45 kW	10.5 kWh	400 km	−−	[25]
Hyundai Nexo	95 KW	1.56 kWh	611 km	60,000 USD	[26]
Toyota Mirai 2	128 kW	1.24 kWh	647 km	50,000 USD	[27]
Honda Clarity 2021	103 kW	−−	579 km	58,000 USD	[28]
Nikola FCEV	200 kW	164 kWh	804 km	750,000 USD	[29]

Table 2.1: FCEVs available in the market and their specifications

Opel Vivaro without modifying the car's body, then preserving the vehicle's cargo space and payload capacity. Moreover, the mid-power concept offers better system durability than a full-power system. Additionally, with a larger battery pack, the vehicle can achieve an electric-only range of up to 50 km, and the battery can be recharged from an external source, like in BEVs [30].

Chapter 3

Detailed modelling of a fuel cell electric van

As previously elucidated, the Opel Vivaro fuel cell, shown in fig. 3.1, was used as a reference in crafting this thesis' FC electric van model. Therefore, many of Vivaro's parameters have been adopted, such as the overall mass of hydrogen stored in the tanks, the vehicle weight, the maximum power of the FC stack, and beyond.

The software used to model the FCEV were MATLAB and Simulink, and the general platform of the vehicle is shown in fig. 3.2. Further explanation of the model logic will be given in the next subsections.

Before delving into the details of the FCEV modelled, it is essential to outline a few key aspects. Three distinct Simulink models were developed. The first is the "FC stack model," designed to generate polarization curves and produce LUTs from these curves. The second model, the "FCS model," is used for creating the FC efficiency map curves, which are used as LUTs in the third model. Lastly, the third model, called here "main vehicle model," mentioned previously as the general platform of

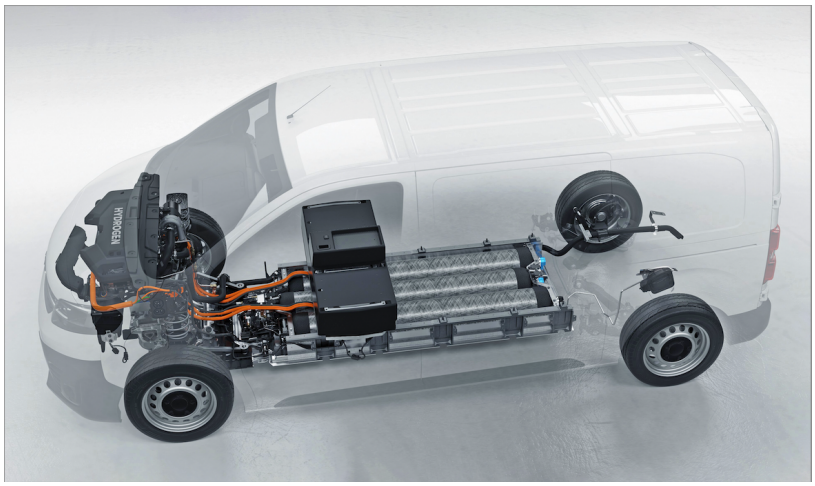

Figure 3.1: Opel Vivaro fuel cell powertrain [2]

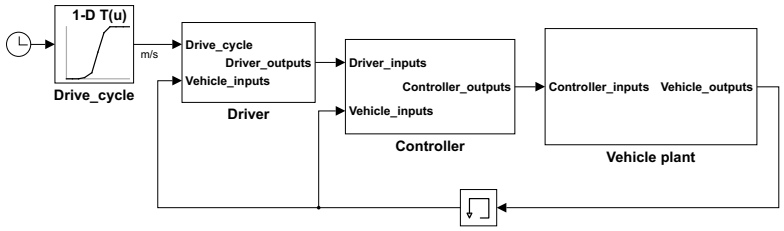

Figure 3.2: Main vehicle model overview

the vehicle, has all the FCEV components and is used to investigate the vehicle's behaviour.

3.1 Opel Vivaro parameters

The FC stacks of the Vivaro are manufactured by the company Symbio. Among the FC stacks available on Symbio's site, the H_2motive stack 40 is the model closest to Vivaro's, as no stacks with the same maximum power output are available. Specifications of the H_2motive stackpack 40 are shown in table 3.1 [31].

Additionally, tables 3.2, 3.3, and 3.4 display the specifications of the Vivaro FCS

Parameter	**Quantity**	**Unit**
Power	40	kW
Stack power density	3.9	kW/liter
Voltage output range	250-450	V
Maximum output current	300	A
Dimension	530 x 350 x 230	mm
Weight	72	kg
Maximum coolant temperature	80	C

Table 3.1: Specifications of the H_2motive stackpack 40

and battery pack, part of its EM characteristics, along with all other details of the Vivaro used to model this thesis's FC van [25].

Parameter	**Quantity**	**Unit**
Fuel cell system		
Total hydrogen mass in tanks	4.4	kg
Pressure	70	MPa
Number of hydrogen tanks	3	–
Fast hydrogen refueling	3	min
FC gross power	45	kW
Ambient operating temperature	-20 - 45	C
Battery pack		
Energy capacity	10.5	kWh
Maximum power	90	kW
Maximum charging power	11	kW
Charging time (empty to full)	∼60	min
Chemistry	Li-ion	–

Table 3.2: Opel Vivaro FCS and battery pack specifications

3.2 Drive cycles

Three distinct drive cycles were used to guarantee a more comprehensive analysis, enabling the examination of various driving patterns. The simulations were conducted

Parameter	**Quantity**	**Unit**
Type	PMSM	–
Power (eco mode)	60	kW
Maximum power	100	kW
Maximum torque	260	Nm

Table 3.3: Opel Vivaro electric motor specifications

Parameter	**Quantity**	**Unit**
Range	>400 (WLTP)	km
Curb weight	1952	kg
Pure electric range	50	km
0 - 100 km/h	15	s
Top speed	130	km/h
Width	2010	mm
Height	1890	mm

Table 3.4: Opel Vivaro's other specifications

using the Worldwide Harmonized Light Vehicle Test Procedure (WLTP), Highway Fuel Economy Test (HWFET), and Urban Dynamometer Driving Schedule (UDDS). The speed profiles of these drive cycles are depicted in fig. 3.3, fig. 3.4, and fig. 3.5, respectively.

The WLTP driving cycle is divided into four distinct phases, according to its average speed, which faces a continuous increase until the cycle's completion. Emerging in 2017, the WLTP represents a significant advance from its predecessor, the New European Driving Cycle (NEDC), which was developed in the 1980s and became obsolete by modern standards. Unlike the NEDC, formulated through theoretical data, the WLTP was built from real-world driving data, increasing its authenticity and aligning it more closely with actual on-road performance [32]. The WLTP was developed to assess light-duty vehicles' emissions and fuel consumption, offering a comprehensive approach to regulatory standards [33].

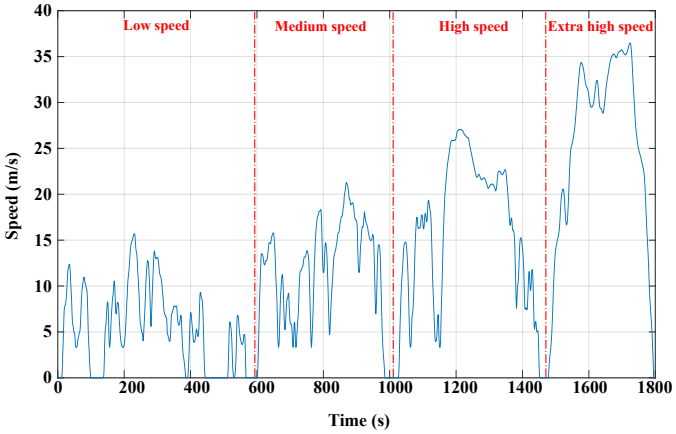

Figure 3.3: WLTP drive cycle speed profile

Discussing the other drive cycles, the HWFET emphasizes highway scenarios, with stops only in the initial phase and at the end of the driving mission, while the UDDS mirrors urban driving conditions, with lower average speed and frequent stops.

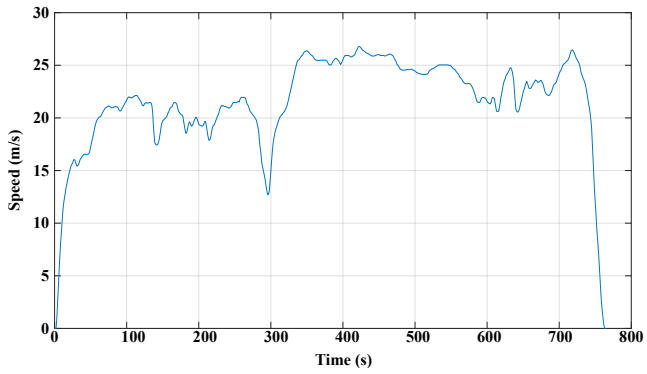

Figure 3.4: HWFET drive cycle speed profile

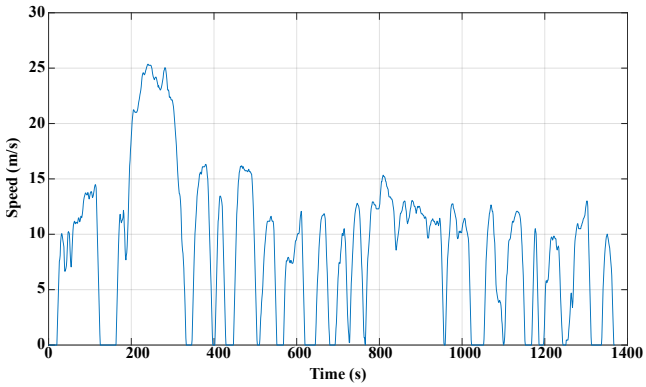

Figure 3.5: UDDS drive cycle speed profile

3.3 Driver

The three primary subsystems of the main vehicle model are the driver, the controller, and the vehicle plant. The driver subsystem, which works as the operation's brain, has two inputs and two outputs. Its inputs are the vehicle speed demand and the actual vehicle speed. The vehicle speed demand, derived from the drive cycle speed profile, specifies the target speed for a given time step. The driver must adjust the vehicle's speed to meet this demand. The subsystem outputs include the acceleration and braking torque demands requested when the vehicle has to speed up or slow down, respectively.

The outputs are governed by a Proportional-Integral-Derivative (PID) controller that adjusts the output torques based on speed error—the difference between the demanded and actual vehicle speed. This dynamic adjustment ensures precise control over vehicle performance, allowing it to reach the speed demands closely. The specific PID parameters, detailed in table 3.5, are chosen for their accuracy in achieving this goal.

Table 3.5: Driver PID controller coefficients

Coefficient	**Value**
Proportional	2000
Derivative	10
Integral	0.5

The PID controller calculates the delta torque and subsequently adds to the torque required to overcome the resistance of the vehicle's demanded state, as detailed in eq.3.3.1. In this equation, m_v represents the vehicle's mass, a_v denotes its acceleration, and α symbolizes the road's incline. Additionally, F_{Dd} and F_{rd} are the drag force and the rolling resistance force at the demanded speed, respectively, while r_w refers to the deformed radius of the wheels.

$$T_{loss} = \frac{(m_v \cdot a_v) \cdot (m_v \cdot g \cdot sin(\alpha)) + F_{Dd} + F_{rd}}{r_w} \tag{3.3.1}$$

Therefore, the output torques are defined by eq. 3.3.2. In this equation, ΔT represents the delta torque the previously mentioned PID controller calculates. T_{drv_accel} represents the torque required to accelerate the vehicle, while T_{drv_brk} specifies the torque necessary for braking.

$$\begin{cases} T_{drv\_accel} = \Delta T + T_{loss},\ \Delta T + T_{loss} >= 0 \\ T_{drv\_brk} = \Delta T + T_{loss},\ \Delta T + T_{loss} < 0 \end{cases} \tag{3.3.2}$$

3.4 Controller

The controller subsystem is designed with seven inputs and five outputs to optimize vehicle performance. The inputs include acceleration and brake torque demands, vehicle speed demand, battery State-of-Charge (SOC), vehicle power demand (or power request), current vehicle speed, and FC power output from the previous time step. The outputs include the controller torque demand, friction brake command, operation mode, and the FC's upper and lower power limits for the current time step. Inside the controller, there is an EMS subsystem, that is responsible for defining the operation mode of the vehicle. A subsequent chapter will provide a more detailed exploration of this EMS subsystem.

The first output, the controller torque demand, is specified in eq. 3.4.1, where $T_{ctrl\_brk\_rg}$ is the portion of the total braking torque demand $T_{ctrl\_dmd\_brk}$ that will be utilized to recharge the battery.

$$T_{ctrl\_dmd} = T_{ctrl\_dmd\_accel} + T_{ctrl\_brk\_rg} \tag{3.4.1}$$

As previously discussed, the initial two inputs come from the driver subsystem, while the drive cycle dictates the speed demand. The vehicle's capacity to deliver the required acceleration torque is analyzed using the acceleration torque demand alongside the actual vehicle speed. If the vehicle cannot provide the demand, the maximum available torque will be adopted as the new acceleration torque demand. Conversely, if the vehicle can meet the demand, the acceleration torque will be equal to the controller's acceleration torque demand. This logic is summarized in eq.3.4.2.

$$T_{ctrl\_dmd\_accel} = min(T_{mot\_lim}, \frac{T_{drv\_accel}}{f_d}, T_{fric\_lim}) \tag{3.4.2}$$

The EM's torque limit T_{mot_lim} is established based on its torque curve, utilizing a 1-D LUT. The term T_{fric_lim} denotes the torque limit the wheels can sustain without slipping. This parameter is detailed in eq.3.4.3, where μ represents the tire friction coefficient, r_w is the wheel radius accounting for deformation due to vehicle weight, m_v is the vehicle mass, and f_d is the final drive ratio. The quantification of these values will be explored later in this chapter. The tire friction coefficient is derived from a 1-D LUT, as illustrated in fig.3.6.

$$T_{fric\_lim} = \frac{\mu \cdot r_w \cdot m_v \cdot g}{f_d} \tag{3.4.3}$$

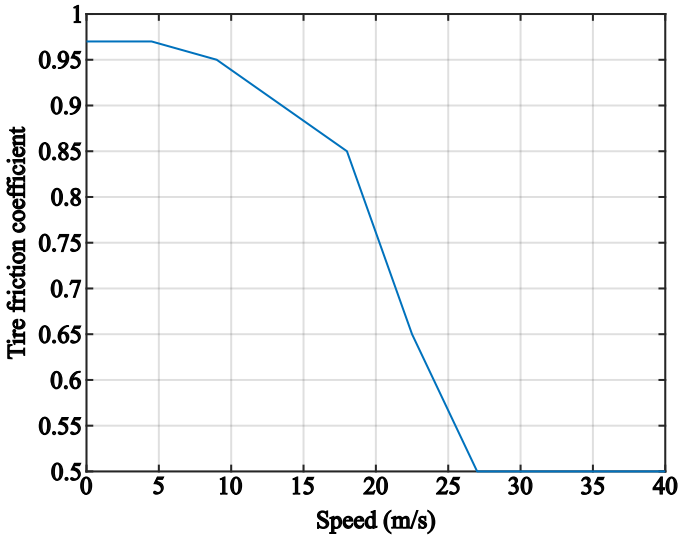

Figure 3.6: Tires friction coefficient map

The regenerated torque $T_{ctrl\_brk\_rg}$ is defined by eq.3.4.4. The fraction of torque

that can be regenerated, denoted as f_{rgn}, varies depending on the vehicle's speed. This amount is measured from a 1-D LUT based on the data in fig.3.7.

$$\begin{cases} T_{ctrl\_brk\_rg} = 0, SOC >= 0.95 \\ T_{ctrl\_brk\_rg} = max(T_{rgn\_lim}, T_{mot\_rgn\_lim}), SOC < 0.95 \end{cases} \tag{3.4.4}$$

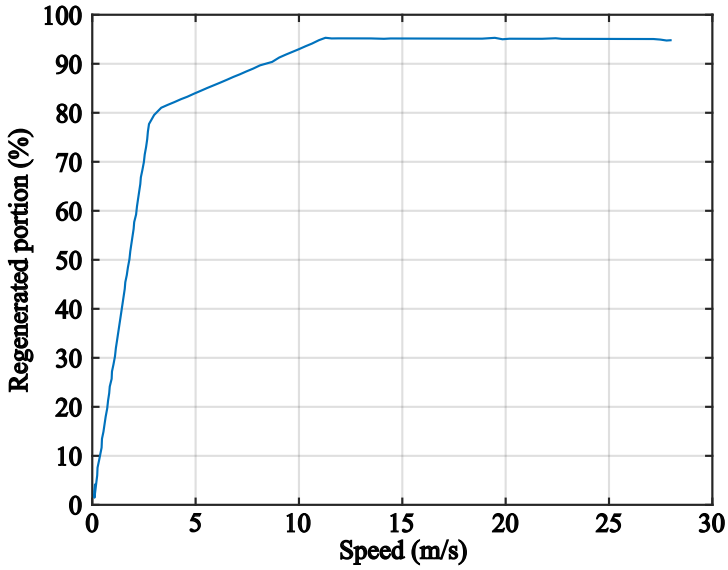

Figure 3.7: Braking torque regenerated portion

The term T_{rgn_lim} is calculated from eq. 3.4.5, while $T_{mot\_rgn\_lim}$ is derived from a 1-D LUT. This table is defined as the inverse torque map of the EM, where for each angular speed input, the torque values mirror those of the EM's torque map but with a reversed sign. This map will be shown when discussing the EM later in this chapter.

$$T_{rgn\_lim} = \frac{f_{rgn} \cdot T_{drv\_brk}}{f_d} \tag{3.4.5}$$

The friction brakes support the portion of the braking torque T_{drv_brk} that can not be regenerated, as shown in eq. 3.4.6. This constitutes the second output of the controller subsystem.

$$T_{ctrl\_dmd\_brk\_fric} = T_{drv\_brk} - T_{ctrl\_brk\_rg} \tag{3.4.6}$$

FCs are significantly influenced by their power dynamics, and imposing power dynamics restrictions is essential for a more realistic analysis of the FC behavior. Researchers in [34] have concluded that implementing power dynamics restrictions for a 40 kW FC, can enhance its durability by 294% compared to an analysis that overlooks this restriction. Moreover, even neglecting the FC SOH degradation, this characteristic must be considered due to the inertia of the air compressor of the FCS, which is a dominant factor limiting the capacity of an FC to change its output power quickly [35].

For the reasons above, this study employs the FC's upper and lower power dynamic limits, which define the maximum and minimum power outputs the FC can produce at each time step during the simulation. These constraints are determined based on the power output from the previous time step and are described by eq. 3.4.7 below. Here, $\dot{P}_{FC}$ denotes the rate of change in FC power output over time. Previous research has utilized similar parameters, as noted in studies [36], and [37]. In other words, eq. 3.4.7 shows that the FC power cannot increase by more than 10% of the FC maximum power P_{FC_max} per second, nor can it decrease by more than 30% of P_{FC_max} per second.

$$-0.3P_{FC\_max} <= \dot{P}_{FC} <= 0.1P_{FC\_max}, \tag{3.4.7}$$

The model that dynamically updates these FC power limits is depicted in fig.3.8. In this model, the "from workspace" block labelled '*act_FC_stack_max_pow*' is responsible for updating the FC maximum power after each run of a drive cycle. This adjustment is important, as it accounts for the decreased FC power output limit due to the FC SOH degradation over time.

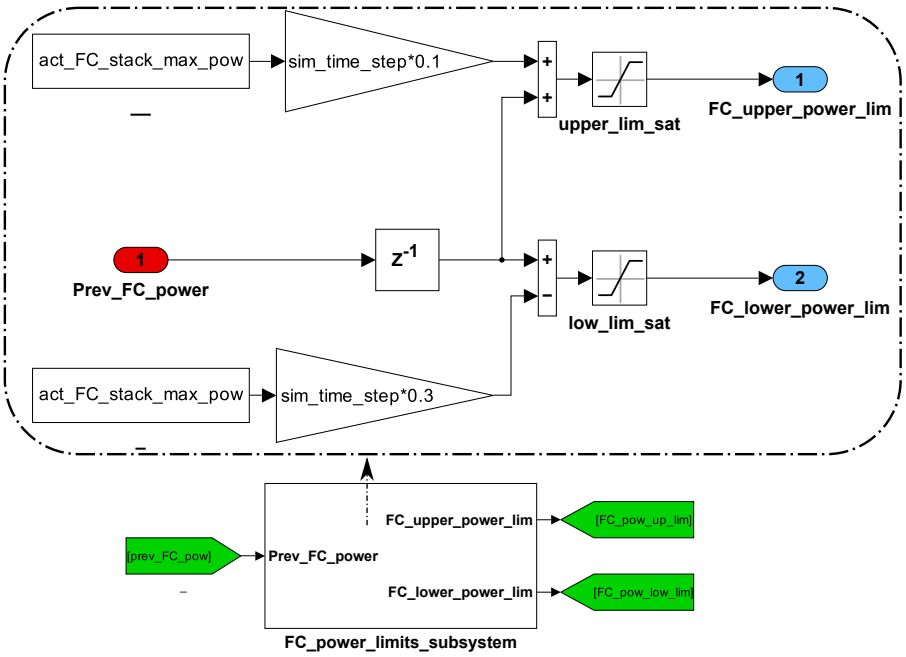

Figure 3.8: Fuel cell power dynamics limits modelling

3.5 Vehicle plant

3.5.1 Fuel cell stack

The FCS model will be divided into two parts: the FC stack and the FC accessories. Additionally, the integration of these models into the main vehicle model will be explained further.

Fuel cell stack model

The Nernst equation, shown in eq. 3.5.1, must be used to calculate the reversible voltage of a fuel cell [38]. The reversible voltage represents the maximum potential the FC can generate across its terminals when there is no current flow. In this equation, P^0 refers to the standard pressure (100 kPa), $P_{\mathrm{H_2O}}$ is the pressure of the water produced in the reactions, $P_{\mathrm{H_2}}$ is the pressure of the hydrogen supplied to the FC, and $P_{\mathrm{O_2}}$ is the pressure of the oxygen provided to the FC. The water pressure is considered equal to the atmospheric pressure in standard conditions (approximately 100 kPa). Therefore, eq. 3.5.1 can be simplified to eq. 3.5.2. Besides, R represents the universal gas constant ($8.314\,\frac{\mathrm{J}}{\mathrm{mol\cdot K}}$), T is the operating temperature of the FC stack, F is the Faraday constant ($96,485\,\frac{\mathrm{C}}{\mathrm{mol}}$), and V_r^0 is the standard cell voltage.

$$V_r = V_r^0 + \frac{RT}{2F} ln \left(\frac{\frac{P_{H_2}}{P^0} \left(\frac{P_{O_2}}{P^0} \right)^{1/2}}{\frac{P_{H_2O}}{P^0}} \right) \tag{3.5.1}$$

$$V_r = V_r^0 + \frac{RT}{2F} ln \left(\frac{P_{H_2}}{P^0} \left(\frac{P_{O_2}}{P^0} \right)^{1/2} \right) \tag{3.5.2}$$

There are two methods to calculate V_r^0. The first method uses eq. 3.5.3, while the second is used in [39] and employs an empirical parameter, as described in 3.5.4. Using the first method, an LUT must be generated for the FC stack Simulink model using the data from table 3.6 [38]. In contrast, the second method simplifies the process by defining V_r^0 using only the fuel cell‘s operating temperature as input and was the method approached here. In eq. 3.5.4, the term k_e is an empirical parameter equal to 0.00085, and V_{r0}^0 is another empirical parameter equal to 1.227 [39].

$$V_r^0 = \frac{-\Delta\overline{g_f}}{2F} \tag{3.5.3}$$

Form of water product	**Temperature** (°C)	**Delta** $\Delta\overline{g_f}$($\mathrm{kJ \cdot mol^{-1}}$)
Liquid	25	-237.2
Liquid	80	-228.2
Gas	80	-226.1
Gas	100	-225.2
Gas	200	-220.4
Gas	400	-210.3
Gas	600	-199.6
Gas	800	-188.6
Gas	1000	-177.4

Table 3.6: $\Delta\overline{g_f}$ for water formation at various temperatures

$$V_r^0 = V_{r0}^0 - k_e(T - 298) \tag{3.5.4}$$

The voltage produced by the cells is not entirely converted into usable energy due to various losses occurring within the FCs. As the current generated by the FC increases, these losses become more pronounced. As found in the literature, three main types of losses are associated with FCs: activation losses, ohmic losses, and concentration losses. Considering these losses, 3.5.5 [39] defines the FC's output voltage.

$$V_{cell} = V_r - V_{act,cell} - V_{ohm,cell} - V_{conc,cell} \tag{3.5.5}$$

As the current density increases, the voltage of the FC tends to drop continuously due to the aforementioned losses. In the polarization curve, different regions are dominated by different types of losses [40], as illustrated in fig. 3.9.

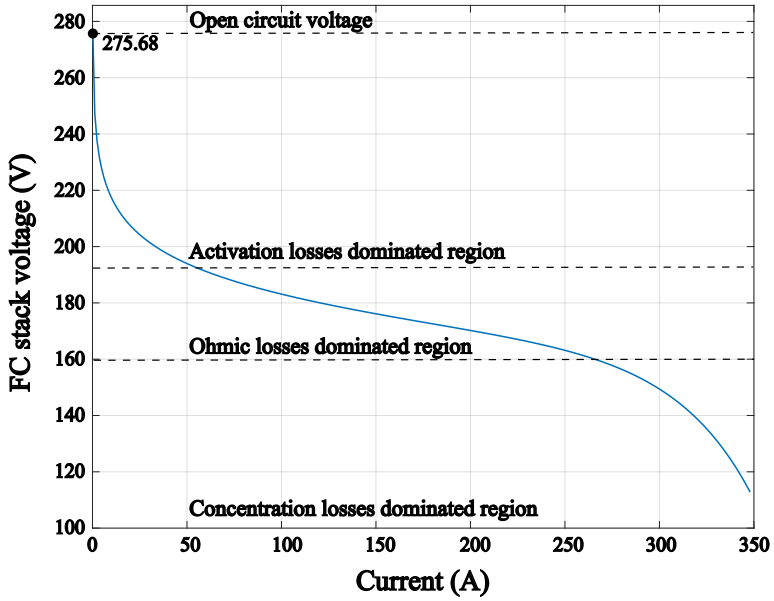

Figure 3.9: Polarization curve and areas of dominance of different losses

Activation losses arise from the slow kinetics of the reactions occurring on the electrode surfaces. This voltage drop is non-linear, with more pronounced effects in the low current region of the polarization curve [41]. It is represented by the Tafel equation, shown here as eq. 3.5.6. The constant A in eq. 3.5.6 is defined by eq. 3.5.7, where α is the 'charge transfer coefficient' and equals 0.5. The term i_0 depends on the material used in the acid electrolyte. Since platinum is the most commonly used material in FCs, its corresponding value is provided in Table 3.7 [41]. Finally, i is the current density flowing through the FC. To consider the losses in both the cathode and the anode, eq. 3.5.6 must be multiplied by 2.

$$V_{act,cell} = Aln(\frac{i}{i_0}) \tag{3.5.6}$$

$$A = \frac{RT}{2\alpha F} \tag{3.5.7}$$

Material	i_0 $(\mathrm{A \cdot cm^{-2}})$
Pb	2.5×10^{-13}
Fe	1×10^{-6}
Ag	4×10^{-7}
Ni	6×10^{-6}
Pt	5×10^{-4}
Pd	4×10^{-3}

Table 3.7: i_0 for different materials

Ohmic losses result from the resistance of electrons flowing through the electrodes and ions moving through the electrolyte. It varies linearly as the current density increases and can be represented by eq. 3.5.8. In this case, r is the area-specific resistance is equal to 30×10^{-6} (kΩ cm^2) for Polymer Electrolyte Membrane Fuel Cells (PEMFCs) [41].

$$V_{ohm,cell} = ir \tag{3.5.8}$$

Lastly, concentration losses occur when the concentration of reactants on the electrode surface diminishes as they are consumed. As it is caused by inefficiency in transporting enough reactants to the surface of the electrodes, it is also known as mass-transport loss [41]. The concentration losses are represented by eq. 3.5.9, where m and n are empirical parameters equal to 3×10^{-5} V and 8×10^{-3} cm$^2 \cdot$ mA^{-1}.

$$V_{conc,cell} = m \exp(ni) \tag{3.5.9}$$

The FC stack model overview is shown in fig. 3.10. As the main vehicle model

must be run multiple times in a loop to investigate how the FC and the battery SOH will change, the results of the FC stack model were inserted as LUTs in the main vehicle model to decrease the complexity and save time when running the loop. This approach significantly reduces complexity and enhances efficiency during the simulation runs.

From the figure, some of the parameters chosen for the stack can be seen, such as the pressures of the cathode and the anode and the total number of cells in the stack. Researchers define that an FCEV typically requires 250 to 400 cells [42]. To get operating values close to the Opel Vivaro', 230 cells were used. This number is realistic, mainly when considering the powertrain modelled as a mid-power configuration, where the FC is smaller than in conventional FCEVs, and the battery is bigger than in other FCEVs, such as the Toyota Mirai.

The pressures were defined as 180 kPa and 250 kPa for the Cathode and Anode, respectively, close to those found in [43] that were also used for an FCEV minivan. The Anode pressure was changed to increase the voltage generated by each single FC. Even though this value is acceptable, as it is not high enough to cause mass transport issues through the PEMFC membrane, that should happen when this pressure goes over 4 bar (400 kPa) [44]. The signal builder used runs current values from 0 to 300 A, which is enough to guarantee that the peak power point can be found.

Defining the cell-active area is crucial for calculating the losses in the FC stack. According to the study [42], the active area of each FC typically ranges from 250 to 400 cm. In the present model, the active area is set to 315 cm, as shown in fig. 3.11. This value was determined through calibration by trial and error to achieve power outputs closely matching those of Vivaro's FC stack and simultaneously avoiding

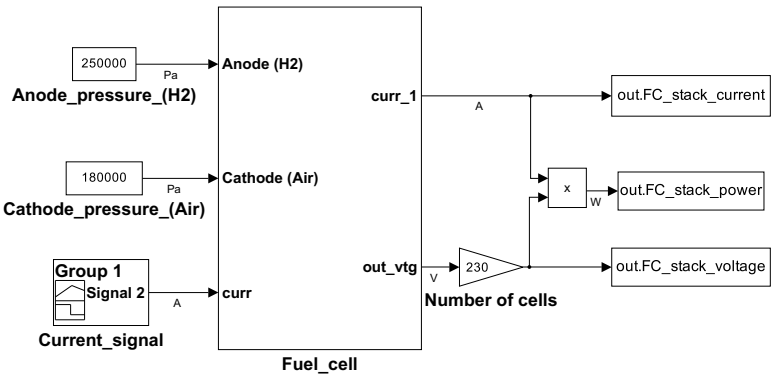

Figure 3.10: Fuel cell stack model overview

excessive losses.

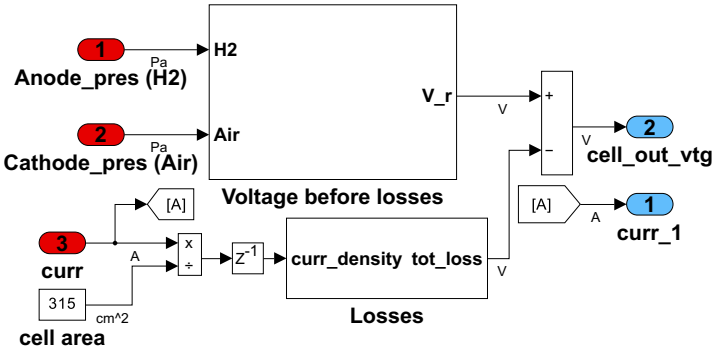

Figure 3.11: Fuel cell model

Figs. 3.12 and 3.13 illustrate the models developed to represent the subsystems "Voltage before losses" and "Losses" in 3.11, respectively. The operating temperature of the FC is set to 80 C. PEMFCs typically operate around this temperature, facilitating quick startup and enhancing durability [45].

Figs. 3.14 and 3.15 presents the power curve and polarization curve for the designed FC stack. These figures also highlight the peak power and voltage achieved by the stack, displaying its performance characteristics.

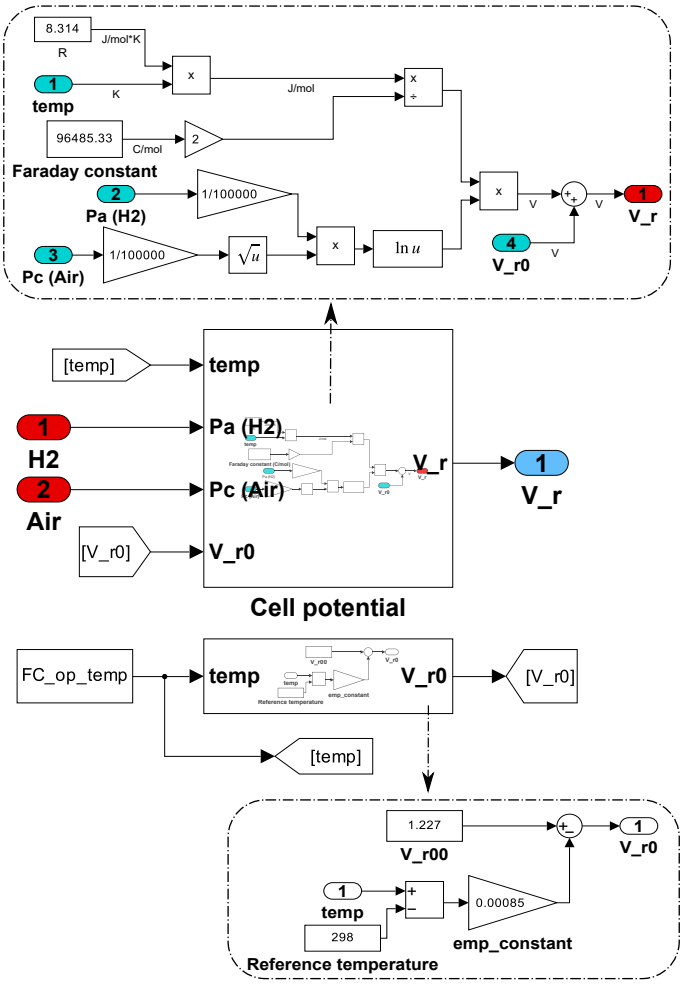

Figure 3.12: Voltage before losses

Fuel cell SOH degradation model

As this thesis focuses on optimizing an FCEV by considering the FC voltage degradation, it is essential to employ a method to quantify it. Numerous mechanisms can degrade an FC stack, but the primary factors identified in the literature regarding FC aging can be summarized into four key elements: the number of start-stop cycles, the duration the FC remains idle, the duration the FC operates at high power, and

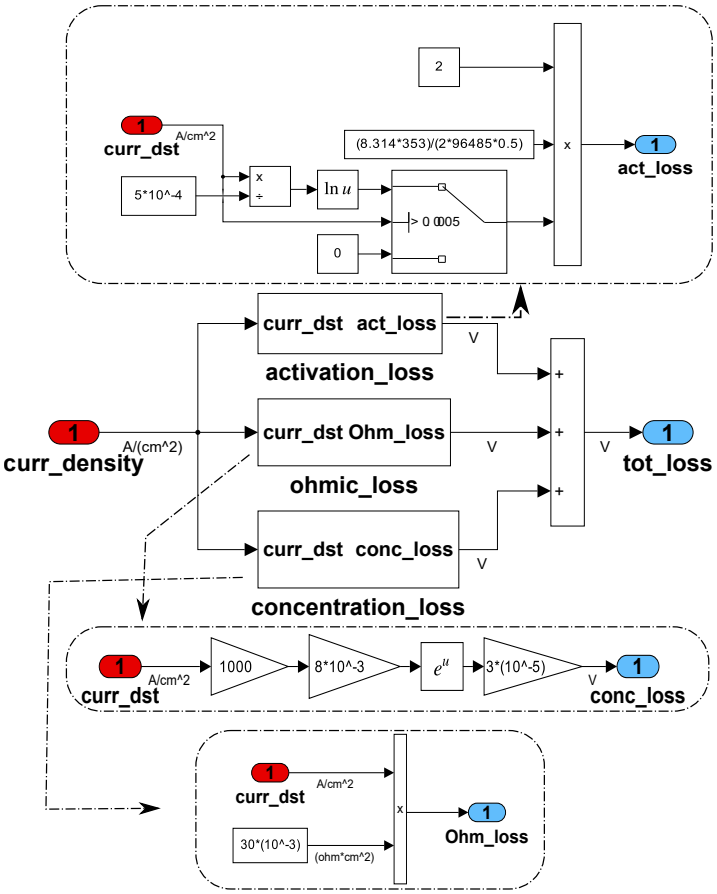

Figure 3.13: Fuel cell voltage losses

the variation of power output faced by the FC.

Pei et al. [46] provided a comprehensive methodology for quantifying the degradation caused by each of these events. Their results have been widely adopted in studies related to FC aging [47] [48]. Subsequently, the same research group conducted another study to quantify these degradation mechanisms [49], and the most recent data are used here. The findings from [50] for two degradation mechanisms are also used, as these results were used in developing the 2nd generation Toyota Mirai.

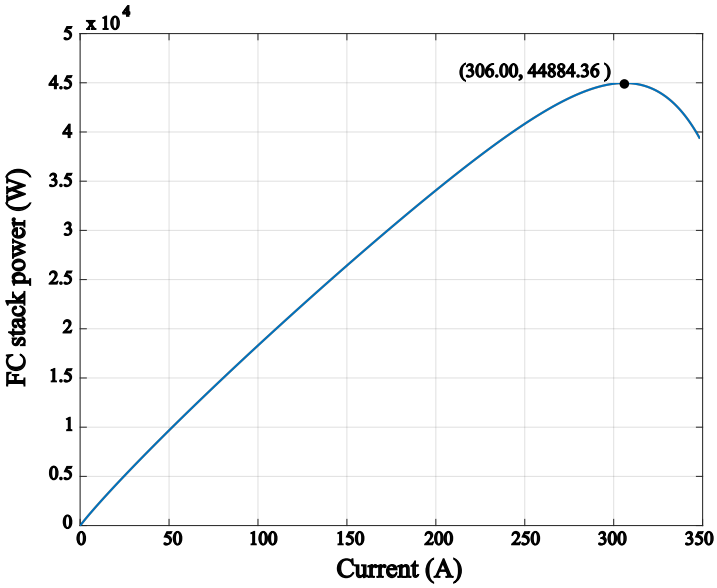

Figure 3.14: Fuel cell stack power curve

Start-stops cycles

The findings presented in [50] reveal that for each start-stop cycle (one start and one-stop), a degradation of 3.3×10^{-7} V occurs in the polarization curve at the point where the FC power density is at its maximum (rated power). It is also shown that at this point, before any aging, the FC voltage is 0.63 V, resulting in a degradation of $5.2381 \times 10^{-4}\%$ per cycle.

Idling condition operation

An FC should also avoid operating under low load power conditions (idling) that usually occur at around 5% of the rated power [51]. According to [49], after one hour of idling, the FC experiences a voltage drop of $8.662 \times 10^{-4}\%$ at the rated current point of the polarization curve (the current value that generates the rated power).

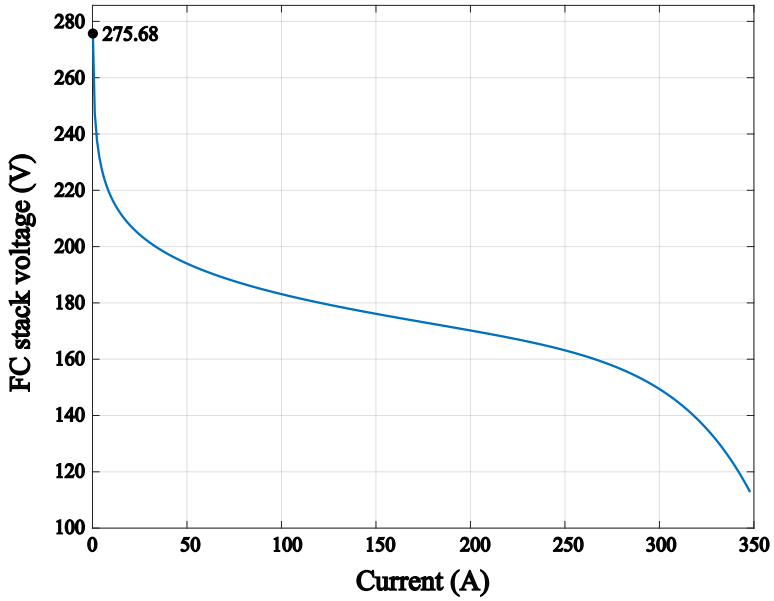

Figure 3.15: Fuel cell stack polarization curve

Load changing operation

The variation in output power of an FC is one of the main issues to consider when designing a control strategy for an FCEV due to its resulting FC degradation. According to findings presented in [50], each cycle of the FC's output power ramping from 0 kW to the rated power and back to 0 kW leads to an SOH degradation of $6.51 \times 10^{-5}\%$ in the polarization curve voltage at the current density level corresponding to the rated power.

High power load operation

The final factor considered is the degradation of the FC when operating under high power conditions (output power exceeding 90% of the rated power). According to Pei et al. [49], operating the FC in high power conditions for one hour results in a voltage

degradation of 10^{-5} %.

The eq. 3.5.9 quantifies the total voltage degradation in the polarization curve of the FC at the rated current. FCs degrade faster in on-road conditions than in laboratories due to variations in operating conditions and air quality [46]. The constant k_p in eq. 3.5.10 is quantified as 1.72 [46], accounting for the additional degradation caused by the on-road operation. n_1, n_2, t_1, and t_2 in eq. 3.5.10 represent the number of start-stop cycles, the number of load-changing cycles, the total time in idling mode, and the total time in high power mode, respectively. k_1,k_2,k_3, and k_4 are the empirical parameters mentioned in the same order.

$$\Delta V\% = k_p \cdot [(t_1 \cdot k_2) + (t_2 \cdot k_4)] + (n_1 \cdot k_1) + (n_2 \cdot k_3) \tag{3.5.10}$$

Then, the FC SOH can be determined through eq. 3.5.11

$$SOH_{FC} = 100 - \Delta V\% \tag{3.5.11}$$

The Simulink models used to calculate FC voltage degradation are in detail illustrated in fig. 3.16, fig. 3.17, and fig. 3.18.

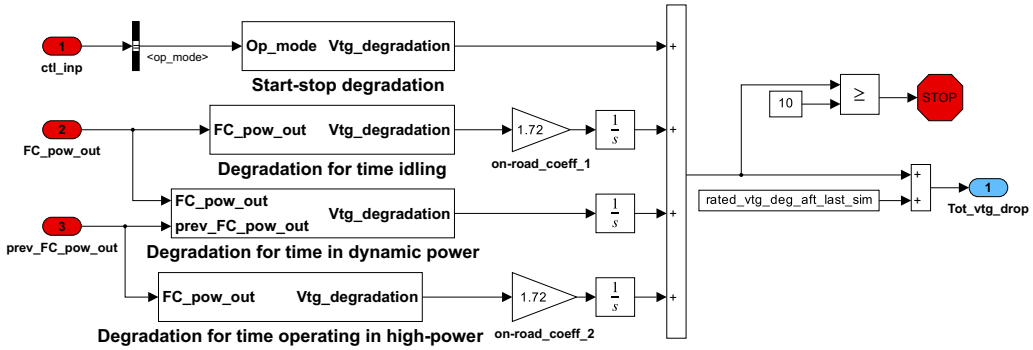

Figure 3.17: Fuel cell aging subsystem - Layer 1

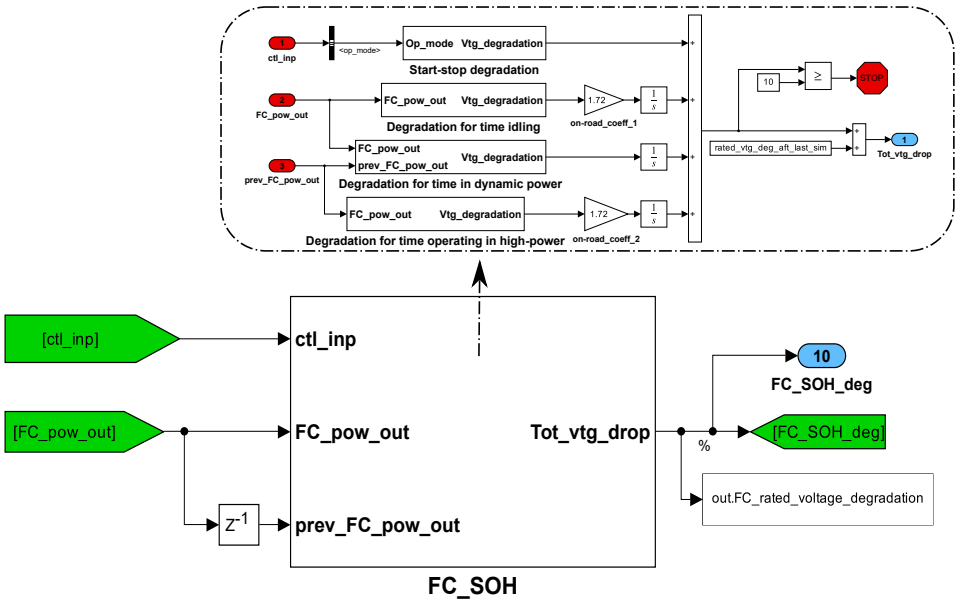

Figure 3.16: Fuel cell aging subsystem overview

Once the degradation of the FC is calculated, its impact on the polarization curve can be estimated. Moreover, updating the polarization curve as the FC degrades can provide more accurate simulation results.

The degradation of the FC voltage is a function of its SOH and current, as shown in eq. 3.5.12. Researchers in [52] discovered that the voltage decrease is linear concerning the current when comparing the polarization curve before and after aging, as described by eq. 3.5.13. These findings have been successfully utilized in other studies, such as [53].

The authors also noted that the model was validated using a 40 kW FC stack. Fig. 3.19 illustrates the predicted curve and the test results, highlighting their remarkable similarities.

In eq. 3.5.13, ΔU_0 represents the change in the FC's OCV, I is the current at

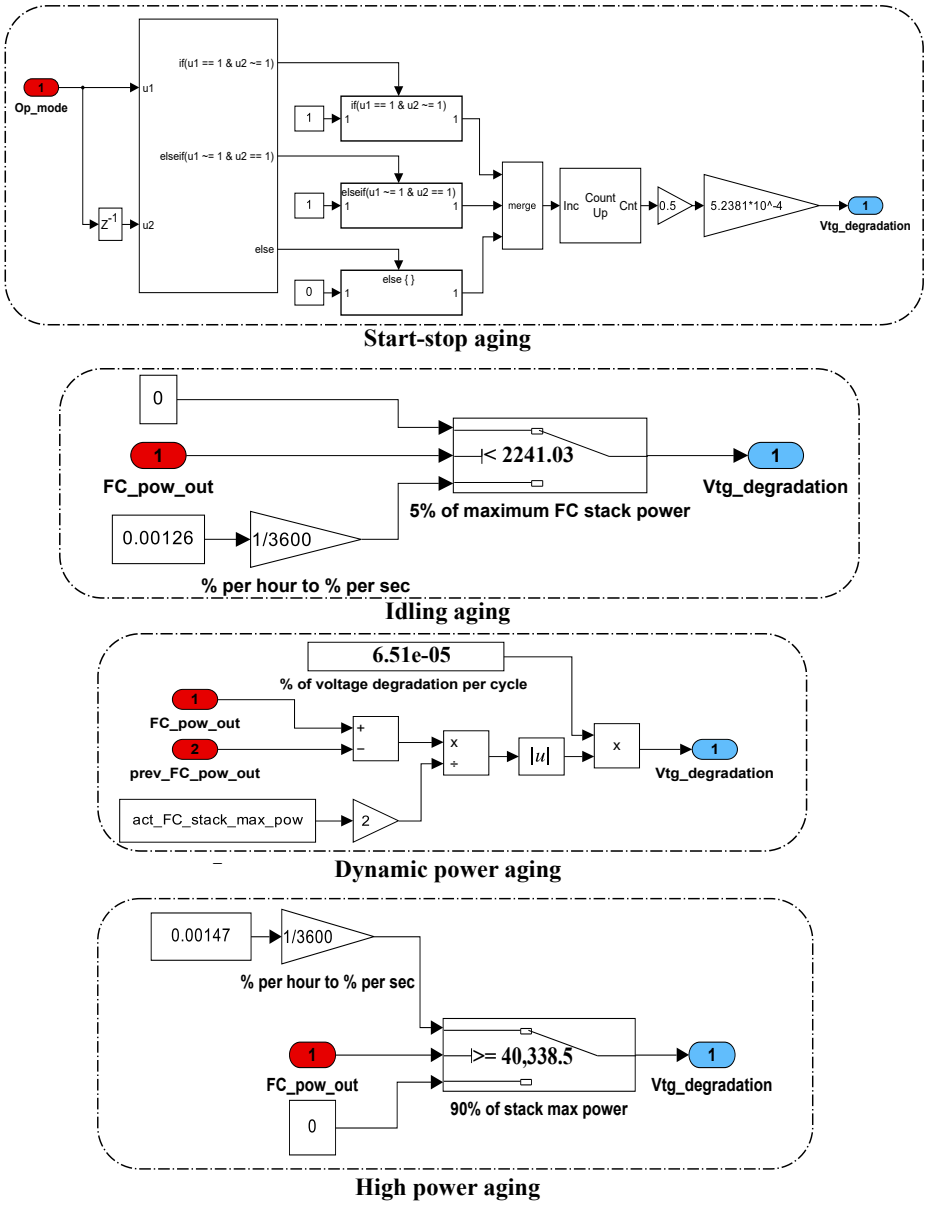

Figure 3.18: Fuel cell aging subsystem - Layer 2

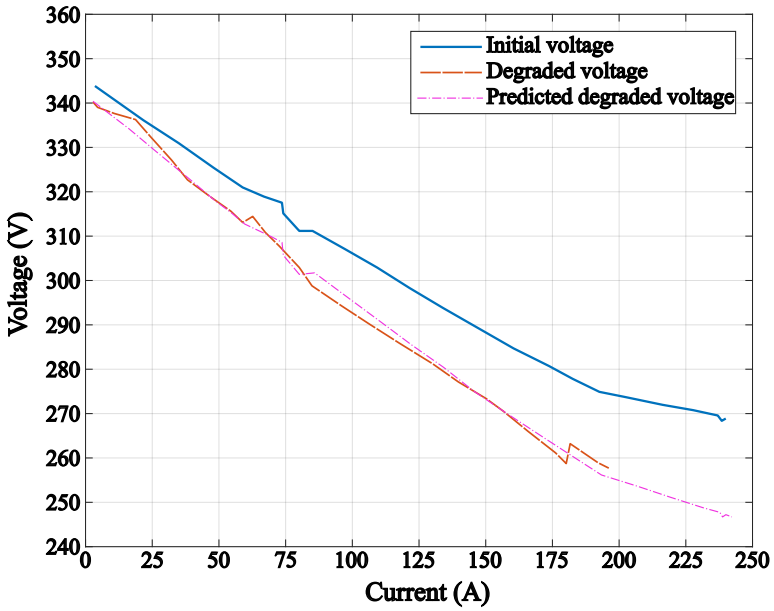

Figure 3.19: Validation of degradation model

which the voltage of the polarization curve is calculated, I_{rated} is the rated current, and U_{rated} is the change in the rated voltage after the FC degrades. This formula determines the polarization curve voltage ΔU for different currents and FC SOH levels.

$$\Delta U = f\left(SOH, I\right) \tag{3.5.12}$$

$$\Delta U = \Delta U_0 + \left(\frac{\Delta U_{rated} - \Delta U_0}{I_{rated}}\right) \cdot I \tag{3.5.13}$$

In the main vehicle model, the FC voltage is derived from a 2-D map that inputs the current and FC SOH. To accurately model this, it is essential to incorporate polarization curves for different SOH levels. The mentioned equations generated polarization curves from the non-aged baseline curve. A total of eleven polarization

curves, ranging from 0% to 10% FC voltage degradation, were created. These generated curves are illustrated in fig. 3.20.

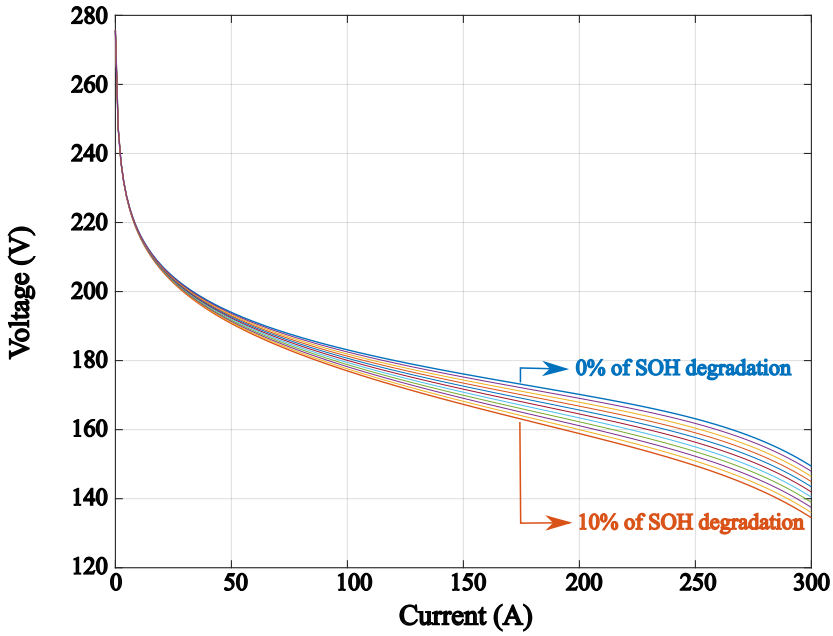

Figure 3.20: Polarization curves after SOH degradation

3.5.2 Fuel cell efficiency maps

The efficiency maps of an FC are essential for estimating its consumption with accuracy. These maps vary significantly based on factors such as cathode and anode pressure, operating temperature, and other conditions. Unfortunately, many studies fail to explain the methodology for obtaining these efficiency maps. A common practice is to scale existing maps to implement in different FC stack models, but this approach often ignores that different maps are created using specific values for the factors above, which can lead to inaccuracies.

In [54], researchers utilized an efficiency map of an FC stack with a peak current of 500 A, which is considerably higher than the one used in the present study. Similarly, in [55], another efficiency map presents anode and cathode pressures of 2.4 and 2.5 bar, respectively. While the anode pressure is close to the value of the FC model developed here, the cathode pressure is significantly higher. The Argonne National Laboratory (ANL) published valuable testing data on the Toyota Mirai FC, including its efficiency map [56]. However, the operating temperature in the Mirai varies continuously, which differs substantially from the FC developed here, which operates at a constant temperature. Numerous other efficiency maps can be found in the literature [57] [58] [59] [60], but none of them match the operating parameters of the FC developed here.

Besides, papers can be found proposing efficiency contour maps for FCs, similar to those used for EMs, as seen in [61], instead of conventional 1-D efficiency maps. Inspired by all the previously mentioned factors and by the fact that the efficiency curves of an FC change as it ages, as shown by [53], a custom FCS model was developed to generate a more accurate efficiency map tailored to the conditions of the FC in different stages of degradation.

Before discussing how the methods were obtained, it is essential to distinguish between the two types of FC efficiencies. The first type is the FC stack efficiency, which accounts for the energy released by the hydrogen reacting within the stack that is not converted into electricity. This efficiency, when plotted against different current levels, mirrors the shape of the polarization curve. The second type is FCS efficiency, which includes the energy consumption of the FC's auxiliary systems and is typically used to estimate hydrogen consumption in FCEV. A figure is shown in [62] where

both efficiency curves can be seen together.

Like the FC stack model, the FCS model was developed in a separate Simulink environment. This approach generated FC efficiency maps used as LUTs in the main vehicle model. This way, it was possible to simplify the main vehicle model and save time during simulations, particularly when investigating the FC and battery degradation when the main vehicle model has to be run continuously in a loop. An overview of the FCS model is shown in fig.3.21.

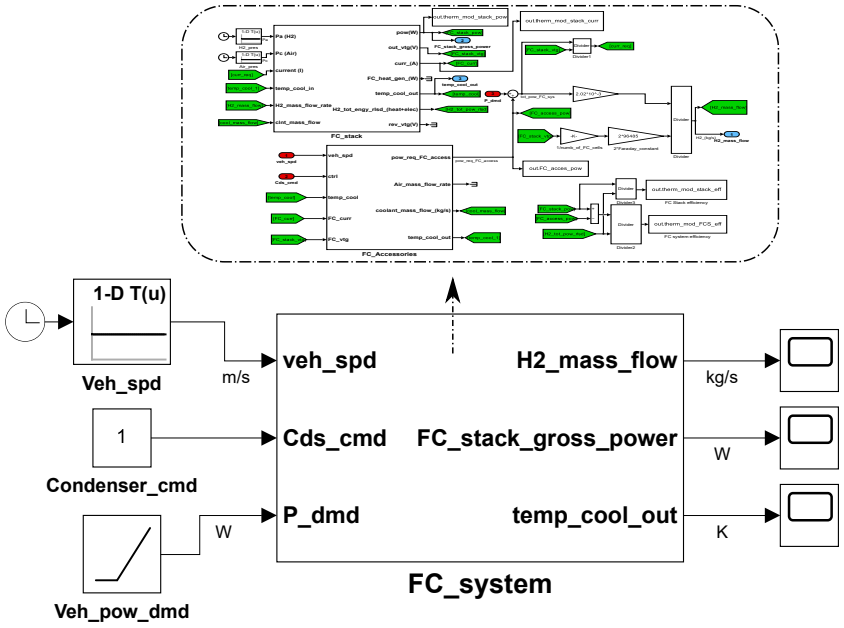

Figure 3.21: Fuel cell system model overview

The developed FCS takes as inputs the vehicle speed, the condenser turn-on command, and a ramp block to test the model under various power demand levels. This setup makes it possible to obtain efficiency results across the FC stack's current range and create an efficiency map similar to the ones found in the literature. Researchers in [63] developed a thermal model considering that the condenser consumes constant power when the FC operates. This assumption was used here, so the condenser is

always on when the FC operates (This is why the condenser command is a constant value).

The heat transfer through the FCS radiator varies significantly at different vehicle speeds. The frequency of accelerations and decelerations further impacts the cooling system's performance. Therefore, instead of creating an efficiency map based on LUTs, the FCS model should be integrated into the main vehicle model to consider the speed's influence on the system's efficiency.

Integrating the FCS model into the main vehicle model would increase complexity, leading to higher computational costs when running simulations to estimate FC and battery degradation. Additionally, it would raise the computational demands of the developed DP code. To overcome this issue, a constant speed equal to 20 m/s was used to calculate the efficiencies, balancing the model accuracy and computational cost.

The details inside the FCS can be seen in fig. 3.22. The explanation of this model is split into some parts to make it clearer.

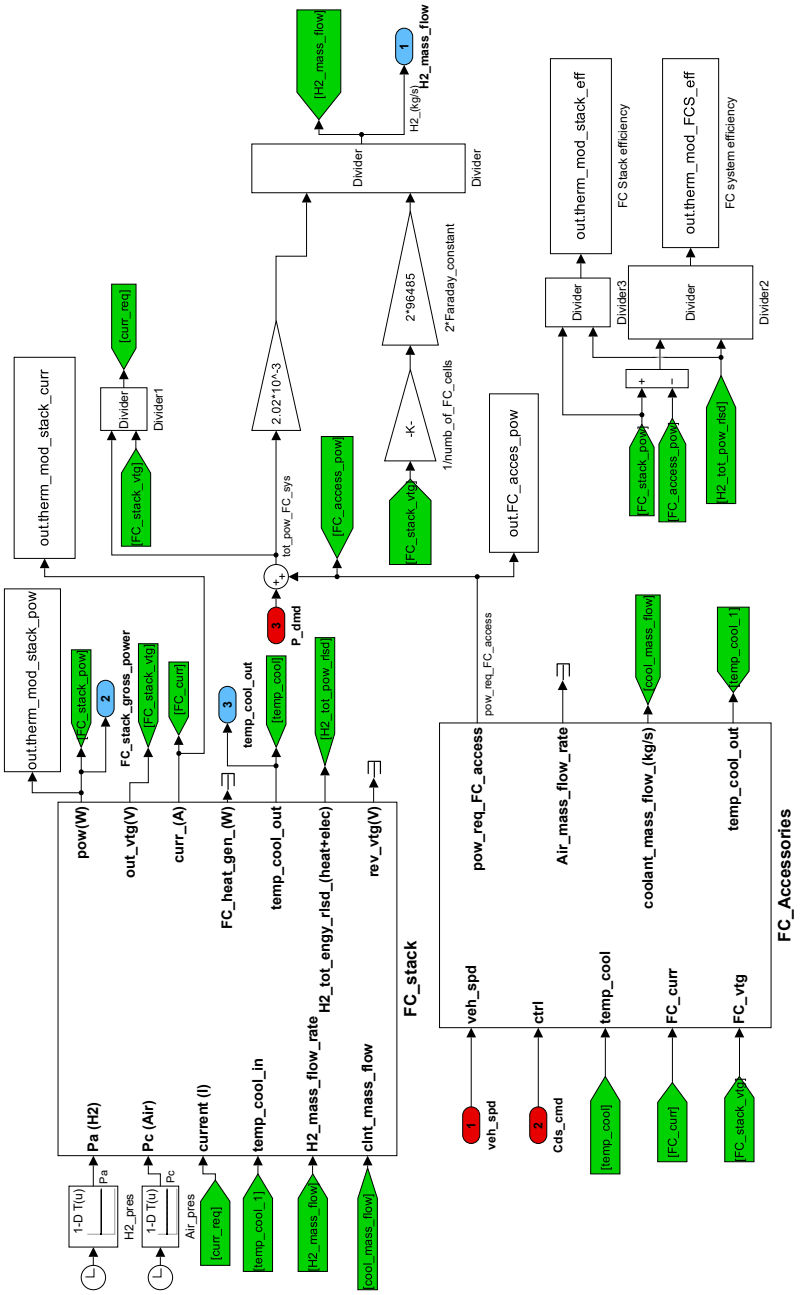

Figure 3.22: Fuel cell system model - Layer 1

Fuel cell stack

Firstly, the "*FC_stack*" subsystem will be explained, which can be seen in more detail in fig. 3.23. In this figure, a subsystem called "*Fuel_cell*" is very similar to the one used to generate the polarization curves, so only the differences will be explained here.

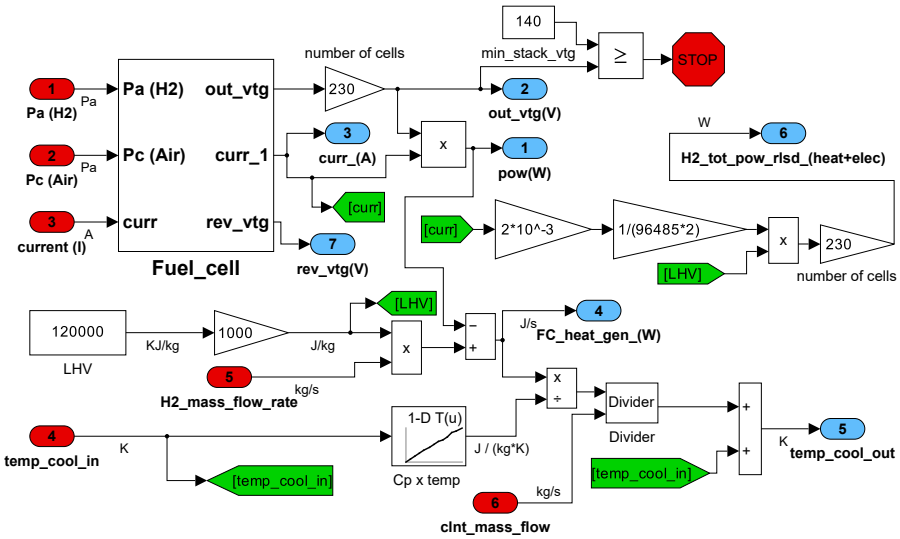

Figure 3.23: Fuel cell stack subsystem of the thermal model

The FC's temperature is maintained at a constant 80°C from the start of the simulation. It means that the heat generated by the stack must be dissipated by the cooling liquid in the cooling system, as estimated by Eq. 3.5.14. In this equation, C_p represents the specific heat capacity at constant pressure, m_{cool} is the mass flow rate of the coolant passing through the FC stack, ΔT_{cool} is the temperature variation of the coolant within the FC stack, $\dot{m}_{H_2}$ is the hydrogen mass flow rate, LHV is the lower heating value (LHV) of the H_2 (120 MJ/kg [64]), and n_{cells} is the number of cells of the stack.

$$C_p \cdot \dot{m}_{cool} \cdot \Delta T_{cool} = (\dot{m}_{H_2} \cdot LHV) - (V_{cell} \cdot I \cdot n_{cells}) \tag{3.5.14}$$

Therefore, the temperature of the coolant varies inside the "FC_stack" subsystem, according to the heat generated by the chemical reactions in the FC stack, as shown by eq.3.5.15, where T_{cool_out} and T_{cool_in} are the temperature of the coolant when getting in and when leaving the FC stack, respectively.

$$T_{cool\_out} = T_{cool\_in} + \Delta T_{cool} \tag{3.5.15}$$

The C_p is a temperature-sensitive value, so a 1-D LUT determines its number from the model's ΔT_{cool}. The coolant used is the $EG60W40$, a mix of 60% Ethylene Glycol and 40% water. The solution's specific mass was assumed to be equal to 1.05 kg/l, and the data of the 1-D LUT mentioned is presented in table 3.8 [65].

Temperature (K)	**Specific heat (J/mol·K)**
253	3541.4
263	3566.5
273	3595.8
283	3620.9
293	3646
303	3671.1
313	3700.4
323	3725.5
333	3750.7
343	3775.8
353	3805.1
363	3830.2
373	3855.3

Table 3.8: EG60W40 specific heat for various temperatures

Finally, the total power generated (or energy per second) by the H_2 chemical

reactions equals the sum of heat and electric power, as shown in eq.3.5.16, which can be determined from the FC current using eq.3.5.17. In eq.3.5.16, Q is the heat generated. In eq.3.5.17, F represents the Faraday constant, and the factor $2 \cdot 10^{-3}$ is used to convert the Faraday constant from C/mol of H_2 to C/kg.

$$P_{H_2\_rlsd} = [Q + (V_{cell} \cdot I)] \cdot n_{cells} \tag{3.5.16}$$

$$P_{H_2\_rlsd} = \frac{2 \cdot 10^{-3} \cdot LHV \cdot I \cdot n_{cells}}{2 \cdot F} \tag{3.5.17}$$

As mentioned, the "$Fuel\_cell$" subsystem is similar to the one previously explained. More specifically, the V_cell is obtained similarly when the FC is at the Beginning-of-Life (BOL). As done previously, the FCS model is used in a loop in its corresponding MATLAB script to test degradation levels from 0% to 10% (such as done to get the polarization curves), and then get efficiency curves for different FC SOH degradation levels.

Instead of outputting the V_cell directly, the output of the "$Fuel\_cell$" subsystem is defined according to eq.3.5.18. Therefore, the voltage will not depend only on the current but also on the FC SOH degradation. In this equation, i represents the degradation level (from 0% to 10%), I_{rated} is the current that generates the rated power at the BOL of the FC, and I_{-1} is the current in the previous time step of the simulation. The value of I_{rated} is defined from the maximum point of the power curve shown in fig.3.14.

$$V_{cell_i} = V_{cell} \cdot \left[1 - \left(\left(\frac{I_{-1}}{I_{rated}}\right) \cdot \left(\frac{i}{100}\right)\right)\right] \tag{3.5.18}$$

The *Fuel_cell* subsystem can be seen in fig.3.24

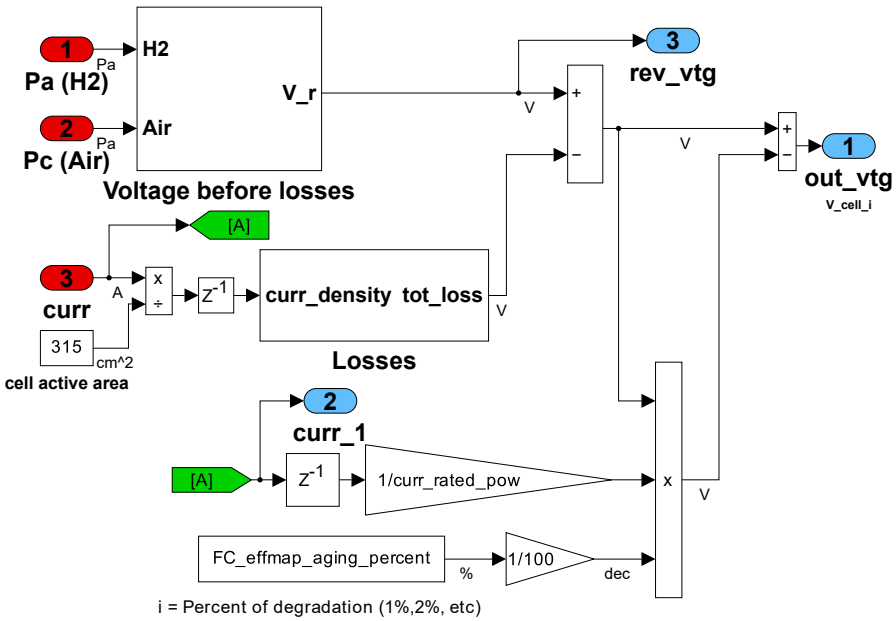

Figure 3.24: Single fuel cell within the FC stack subsystem of the thermal model

Fuel cell accessories

According to [63], modelling an FCS and its thermal behaviour involves six major components: The FC stack, air compressor, coolant pump, radiator, condenser fan, and humidifier. However, the role of humidifiers in FCEVs is no longer considered crucial. Modern FC stacks can self-humidify, recycling the water produced within the cells and thus eliminating the need for a separate humidifier [66]. Due to this, the humidifier was not included as one of the FC accessories. Consequently, the humidifier has not been considered as one of the accessories here. An illustrated overview of the modelled FC accessories subsystem is presented in fig.3.25.

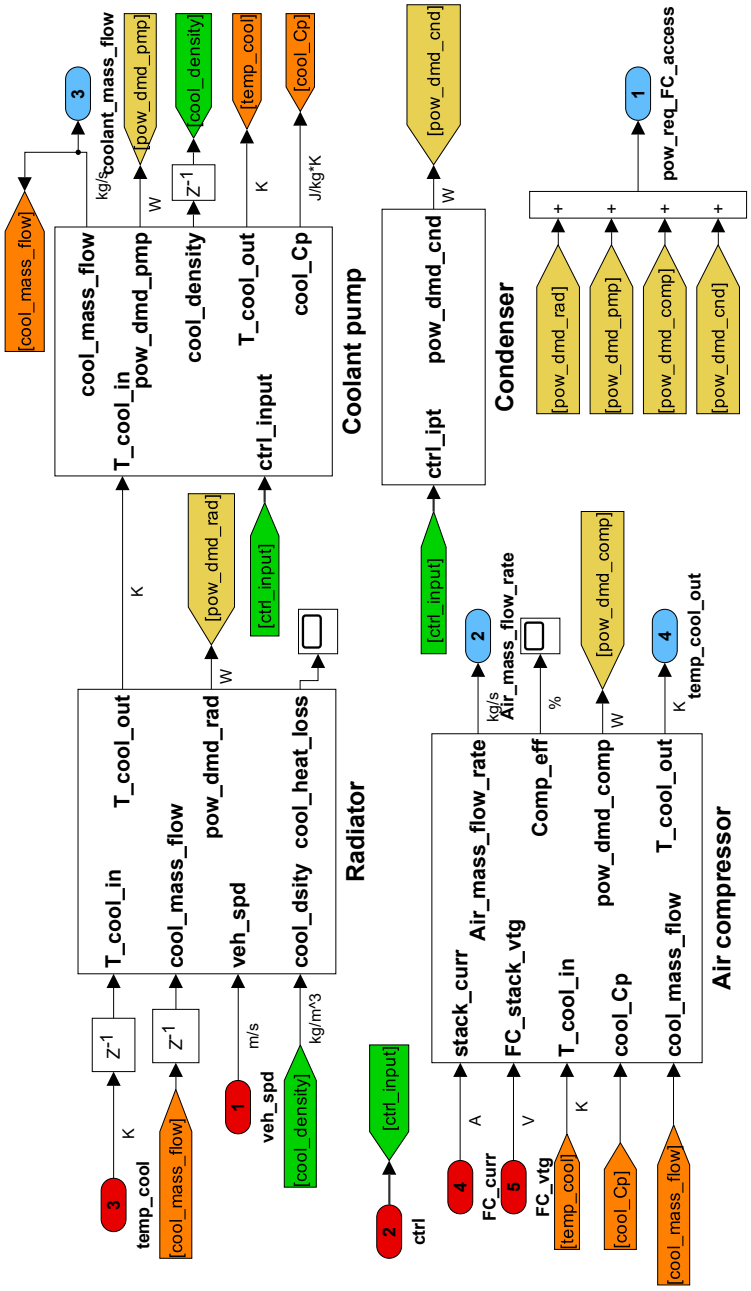

Figure 3.25: Fuel cell accessories subsystem overview

Air compressor Researchers in [67] have conducted a comprehensive review of air compressors used in FCEVs and concluded that compressors manufactured by

Rotrex provide a robust maximum airflow of 90 g/s, a versatile flow range, and good efficiency, with a peak of over 75%. Specifically, the models EK-10 and EK-40 are designed for FCSs ranging from 20-100 kW and 100-400 kW, respectively [68]. Given that the FC stack modelled in this study has a peak power output of approximately 45 kW, data from the EK-10 will be utilized. Additional details are available in the datasheet referenced in [68].

Two variations of the EK-10 model are available, differing by their recommended air mass flow and pressure ratio ranges. For this study, the model EK-10C-1220 was selected due to its capability to cover a broad mass flow range, effectively meeting the air pressure requirements.

To calculate the air mass flow required from the compressor, the eq.3.5.19 is utilized. In this equation, $28.97 \cdot 10^{-3}$ is the molar mass of air in $\frac{kg}{mol}$, γ represents the stoichiometric ratio (the ratio of mols of hydrogen to mols of oxygen), that is equal to 2. This ratio reflects the chemical reactions within the FC, where every two hydrogen molecules react with one oxygen molecule, as detailed in eq.3.5.20.

P_e represents the power generated by the FC stack, the value 0.21 denotes the molar proportion of oxygen in the air, V_c is the voltage of each cell, indicating the electrical potential across it, and the constant 4 accounts for the total number of electrons involved in the chemical reactions.

$$\dot{m}_{air} = \frac{28.97 \cdot 10^{-3} \cdot \gamma \cdot P_e}{0.21 \cdot 4 \cdot V_c \cdot F} \tag{3.5.19}$$

$$2\,H_2 + O_2 \longrightarrow 2\,H_2O \tag{3.5.20}$$

The efficiency of the subsystem is linked to two key components: the adiabatic efficiency of the air compressor and the efficiency of the EM powering it. The air mass flow rate is a pivotal factor influencing this efficiency, as detailed in eq. 3.5.21. The pressure ratio, defined as output to input air pressure, is crucial in determining the adiabatic efficiency, as outlined in eq. 3.5.22.

As the air suffers compression, the adiabatic efficiency drops. The efficiency of the EM is set as constant and equal to 98%. Meanwhile, the adiabatic efficiency is determined using a 2-D efficiency map. The map for the EK-10C-1220 has been scaled to align more accurately with the required mass flow range. The air compressor efficiency map is demonstrated in fig. 3.26.

$$\eta_{air\_sub} = \eta_{adiab}(\dot{m}_{air}, p_{ratio}) \cdot \eta_{elec} \tag{3.5.21}$$

$$P_{ratio} = \frac{P_{out}}{P_{in}} \tag{3.5.22}$$

Understanding each accessory's power consumption is essential to accurately calculate the FCS efficiency. This is particularly crucial for the air compressor, a critical accessory that demands significantly more power than the other accessories. The compressor's power consumption is determined using eq. 3.5.23. In this equation, C_{p_air} represents the specific heat capacity at constant pressure, for which 1005 (1005 $\frac{J}{kg \cdot K}$ is utilized.

Although the specific heat capacity of air C_{p_air} varies with temperature, its value at $300K$ is used because its variation across temperatures is minimal. The constant k represents the ratio of the specific heat at constant pressure to that at constant

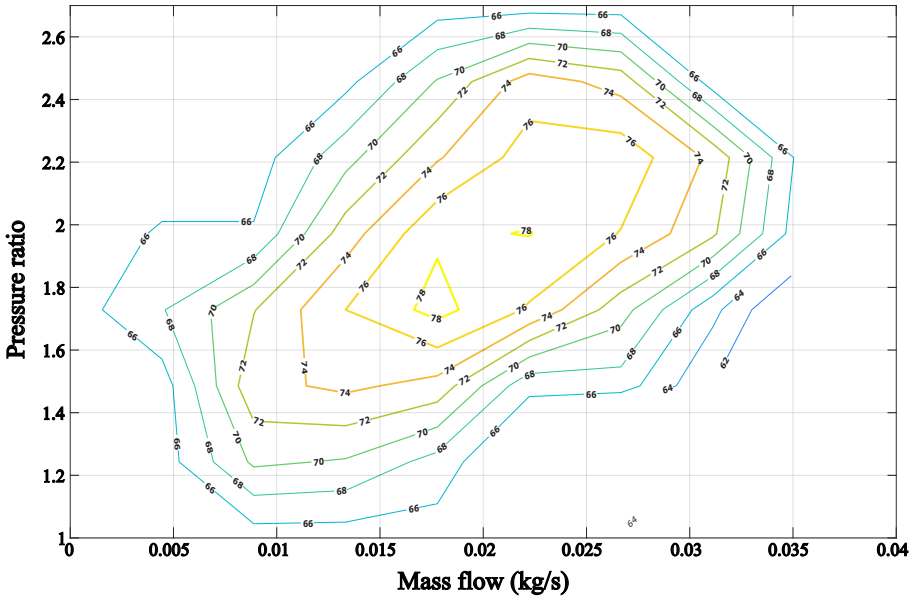

Figure 3.26: Fuel cell air compressor efficiency map

volume, as outlined in eq.3.5.24. The specific heat at constant volume C_{v_air} is 718 $\frac{J}{kg \cdot K}$ at 300 k, and this value was adopted for the calculations. The T_{amb} is assumed to be 25 °C.

$$P_{comp}(\dot{m}_{air}, T_{amb}, p_{ratio}) = \frac{\dot{m}_{air} \cdot C_{p\_air}(T_{amb}) \cdot T_{amb} \cdot P_{ratio}^{\frac{k-1}{k}-1}}{\eta_{adiab} \cdot \eta_{elec}} \tag{3.5.23}$$

$$k = \frac{C_{p\_air}}{C_{v\_air}} \tag{3.5.24}$$

As the efficiency issue suggests, not all the energy the air compressor consumes is utilized in pressurizing the air. The residual energy is transformed into heat, dissipating through the liquid coolant. Consequently, it is crucial to calculate the heat generated and the temperature variation of the coolant within the air compressor subsystem. The eq. 3.5.25 and eq. 3.5.26 are used to estimate the heat generated and

the temperature variation of the coolant, respectively.

$$Q_{comp} = P_{comp} \cdot [1 - (\eta_{adiab} \cdot \eta_{elec})] \tag{3.5.25}$$

$$T_{cool\_out\_comp} = \frac{C_{p\_air}\dot{m}_{cool}}{Q_{comp}} + T_{cool\_in\_comp} \tag{3.5.26}$$

Finally, the air compressor model can be seen in fig.3.27.

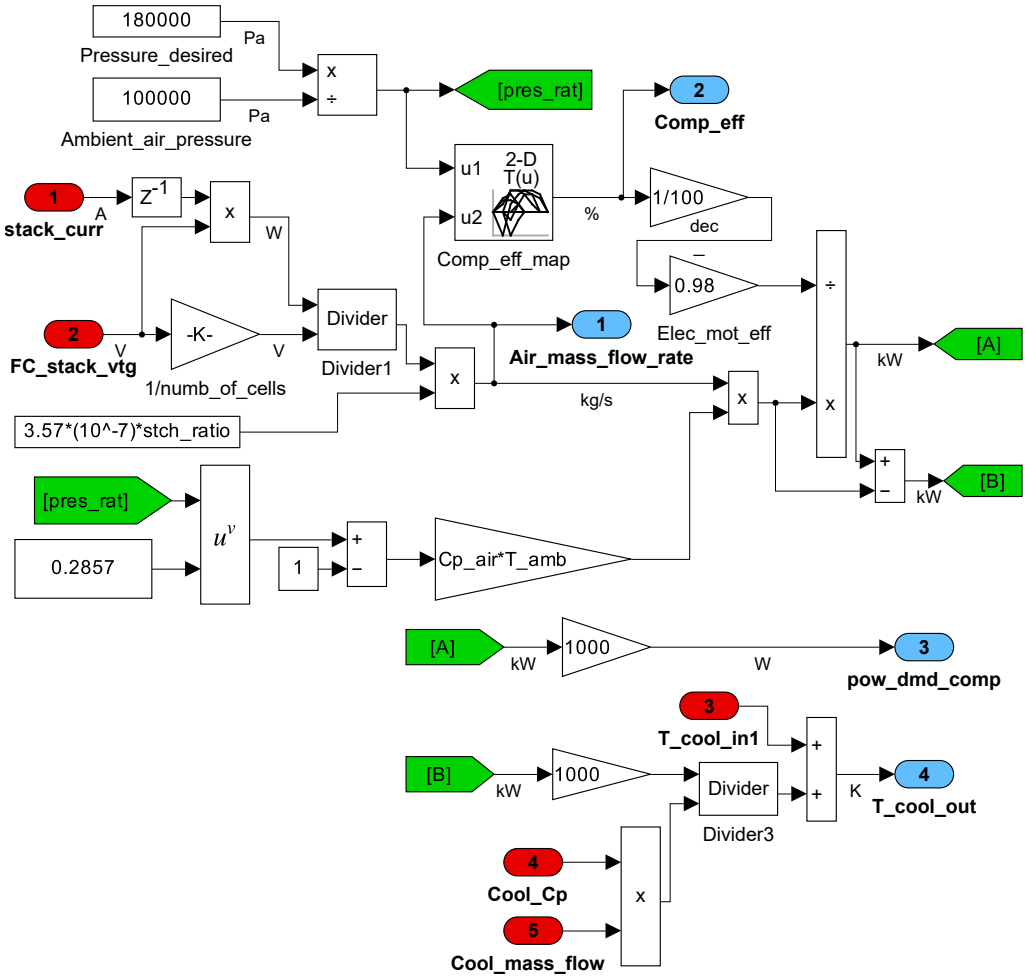

Figure 3.27: Fuel cell air compressor subsystem

Coolant pump The coolant pump subsystem has one input and five outputs. The input is the temperature of the coolant from the output side of the radiator, and the outputs are: The coolant mass flow, coolant pump power demand, coolant density, the updated temperature of the coolant, and the coolant specific heat at constant pressure.

Between the inlet and outlet sides of the coolant in the pump, the fluid experiences a pressure drop influenced by its temperature and mass flow rate. Calculating this value is essential for determining the volumetric flow of coolant through the pump. To prevent an algebraic loop, the pressure drop is defined based on the coolant's mass flow rate from the previous time step, as specified in eq. 3.5.27. Additionally, the data of fig. 3.28 [69] serves as a LUT for this purpose.

$$\Delta P_{\text{cool}} = P_{\text{cool\_in}} - P_{\text{cool\_out}} = f(T_{\text{cool}}, \dot{m}_{\text{cool-1}}) \tag{3.5.27}$$

The volumetric flow rate of the coolant generated by the pump depends on the pressure drop and the rotational speed of the pump rotor. In the FCS model, the rotational speed is defined as constant when the FC operates, set at 1500 RPM. Consequently, the data presented in fig. 3.29 [69] determines the coolant flow rate.

The density of the EG60W40 coolant is derived from the output of the radiator subsystem by eq. 3.5.28. Given that this value varies significantly with temperature, a LUT based on fig. 3.30 [65] is employed to update the density value based on the coolant temperature from the radiator subsystem at each time step.

$$\rho_{cool} = f(T_{cool\_rad\_out}) \tag{3.5.28}$$

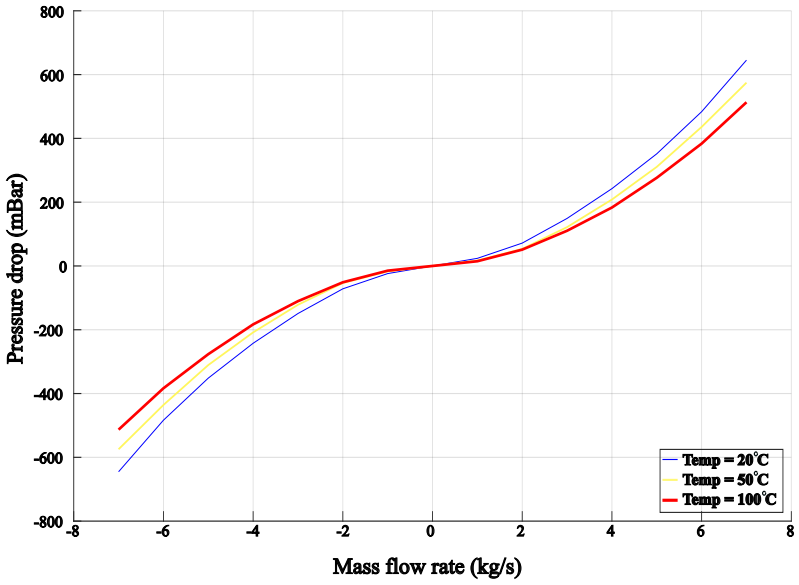

Figure 3.28: Coolant pressure drop for different conditions

The mass flow rate of the coolant is calculated using eq. 3.5.29, where $\dot{V}_{cool}$ represents the volumetric flow rate of the coolant. This calculation is derived from the known values of the volumetric flow rate and the mass density of the coolant.

$$\dot{m}_{cool} = \rho_{cool} \cdot \dot{V}_{cool} \tag{3.5.29}$$

The volumetric flow rate of the coolant is utilized to estimate the efficiency of the coolant pump and the power consumed. The plots shown in fig.3.31, referenced in [70], serve as LUTs for calculating these values.

The electric power consumed by the pump is partially converted into mechanical energy and partially dissipated as heat. Within the coolant pump subsystem, this generated heat must be effectively removed by the coolant, so eq. 3.5.30 must be satisfied. In this equation, C_{p_cool} represents the specific heat of the coolant at constant

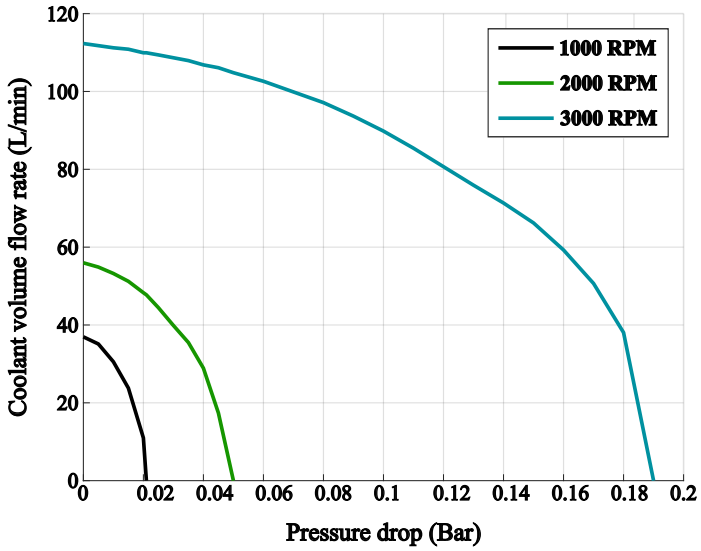

Figure 3.29: Coolant pump volume flow output for multiple rotor speeds

pressure, η_{pump} denotes the efficiency of the pump, P_{cool_pump} is the power consumption of the coolant pump and $\dot{m}_{cool}$ is the mass flow rate of the coolant. The specific heat C_{p_cool} is recalculated using table 3.8 data.

$$T_{cool\_out} = T_{cool\_in} + \frac{P_{cool\_pump} \cdot (1 - \eta_{pump})}{\dot{m}_{cool} \cdot C_{p\_cool}} \tag{3.5.30}$$

Finally, the coolant pump subsystem is shown in fig.3.32.

Radiator Heat generation occurs in the other components of the FCS. The radiator is responsible for dissipating the heat the coolant absorbs, thereby maintaining the FC within its optimal operating temperature range. Four inputs and three outputs characterize the radiator subsystem modelled.

The inputs include the temperature of the coolant on the inlet side, the mass flow of the coolant, the density of the coolant, and the vehicle speed. The first three inputs

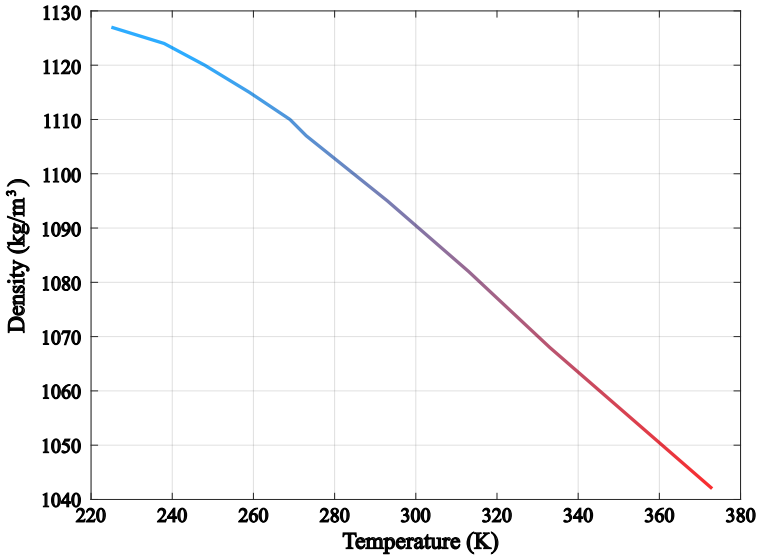

Figure 3.30: Coolant EG60W40 specific mass at different temperatures

correspond to the values from the previous time step of the simulation, as depicted in fig. 3.25. The outputs consist of the temperature of the coolant on the outlet side, the power demanded by the radiator fan, and the heat loss.

The heat that the coolant removes when passing through the radiator depends on the volume flow rate and the speed of air moving through the radiator, as described by eq. 3.5.31. This value is determined using a 2-D LUT derived from the radiator heat loss map in reference [69]. To satisfy the requirements of the FCS, this map was scaled by a factor of 2.1. This scaling was necessary because the radiator used in the cited study was too small for the FC stack developed in this work.

$$Q_{cool\_rad} = f(\dot{V}_{cool}, v_{air}) \tag{3.5.31}$$

The airspeed varies by region, as illustrated in fig. 3.33, which depicts a ventilated

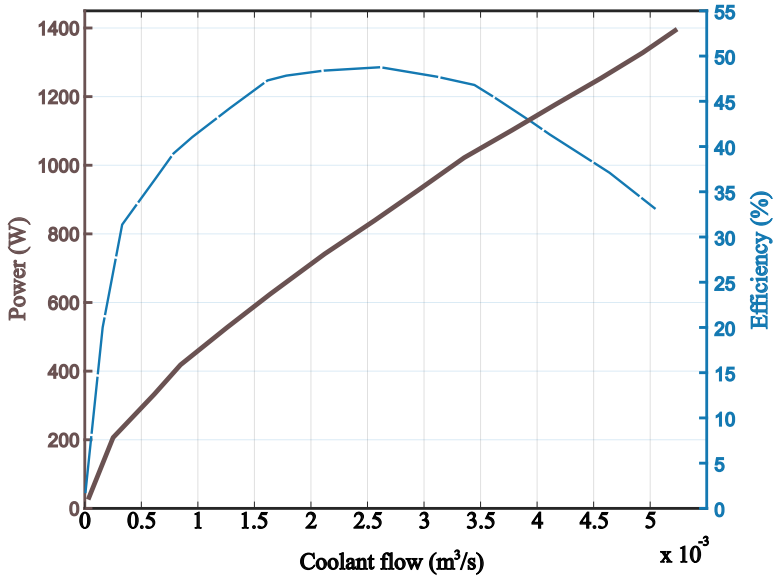

Figure 3.31: Coolant pump efficiency and power map

and a non-ventilated area on the radiator surface. When the radiator fan is active, the airspeed increases by 4 m/s in the ventilated area. Conversely, if the fan is not operating, the airspeed remains uniform across both regions.

The operation of the radiator fan is governed by eq. 3.5.33. A relay block stabilizes the radiator's operational state and prevents frequent changes. Once activated, the radiator remains on until the coolant temperature reaches 338 K. The radiator's dimensions for ventilated and non-ventilated areas are shown in fig. 3.33. It is assumed that the radiator fan consumes 300 W when operating.

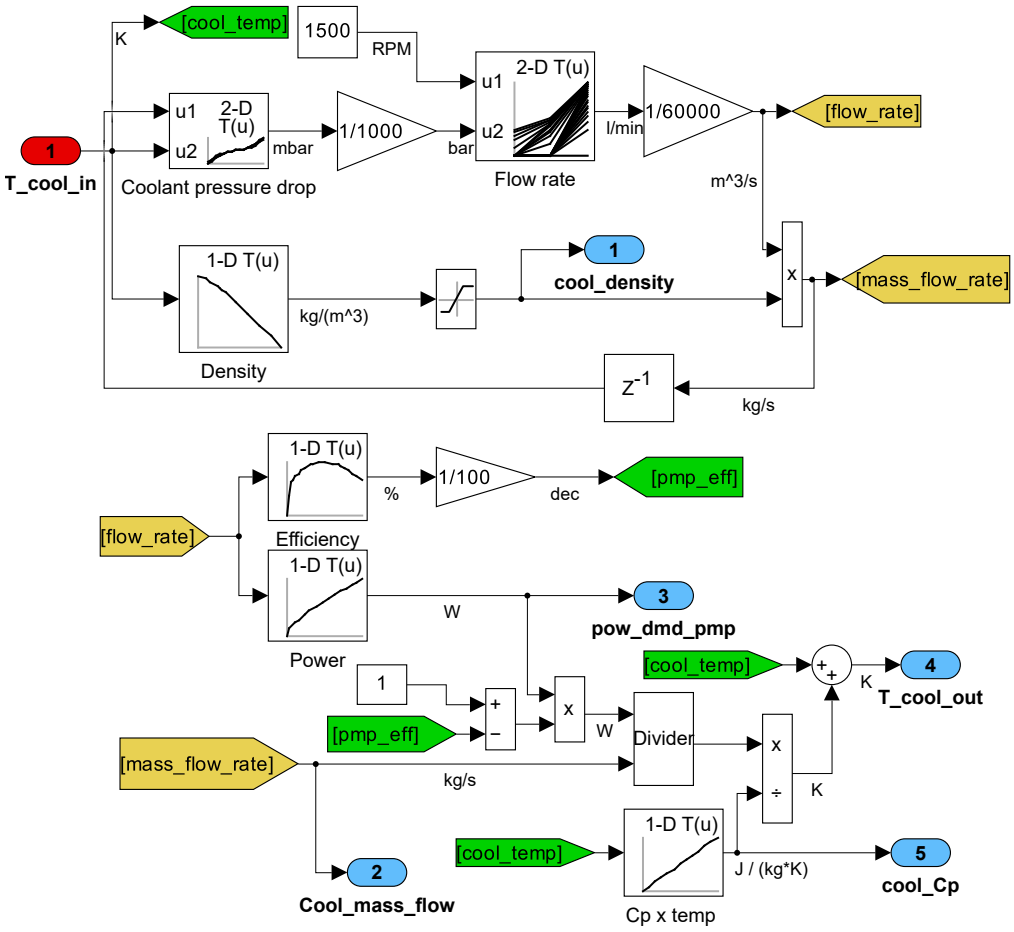

Figure 3.32: Fuel cell coolant pump subsystem

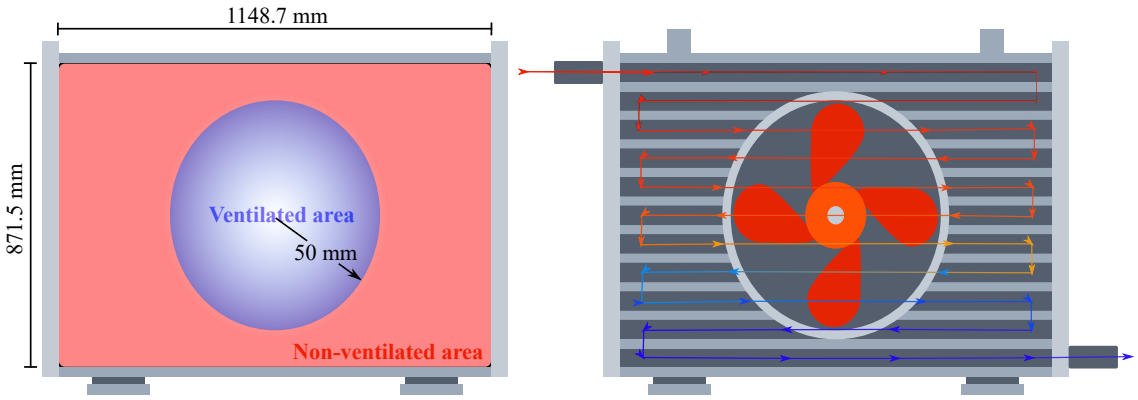

Figure 3.33: FCS radiator and its dimensions

$$\begin{cases} T_{rad\_cool\_in} - 353 >= 15, fan\_on \\ T_{rad\_cool\_in} - 353 <= -15, fan\_off \end{cases} \tag{3.5.32}$$

In certain scenarios, the coolant temperature may decrease excessively even when the radiator fan is inactive. Under such conditions, the coolant does not circulate through the radiator; instead, it utilizes a bypass valve to conserve heat. This phenomenon is described in eq. 3.5.33. To prevent frequent change of states, a relay block is employed. Once the bypass valve is closed, it reopens only when the coolant temperature falls to 348 K.

$$\begin{cases} T_{rad\_cool\_in} >= 353, by\_pass\_closed \\ T_{rad\_cool\_in} <= 348, by\_pass\_opened \end{cases} \tag{3.5.33}$$

It is important to note that the airspeed passing through the radiator is 0.15 times the vehicle speed. This speed reduction is attributed to the vehicle's grid at the front. Although higher airspeed enhances heat dissipation efficiency, it is essential to balance air drag and cooling performance [69], and that's why this grid is used. The radiator subsystem is shown in detail in fig. 3.34, which is located at the end of this chapter.

Condenser fan The condenser is assumed to operate continuously when the FCS is active. Furthermore, researchers in [63] employed a reasonable estimate of $300W$ for the power consumption of the condenser fan. This same value has been adopted here.

Fuel cell system

After calculating the FC accessories' power consumption, the FC stack's required power can be estimated using eq. 3.5.34. The power demand of the FC accessories is determined by eq. 3.5.35.

$$P_{stack\_req} = P_{veh\_dmd} + P_{acces\_dmd} \tag{3.5.34}$$

$$P_{acces\_dmd} = P_{dmd\_rad} + P_{dmd\_comp} + P_{dmd\_pmp} + P_{dmd\_cnd} \tag{3.5.35}$$

The hydrogen mass flow rate can be determined from the FC stack power, as defined in eq. 3.5.36.

$$\dot{m}_{H_2} = \frac{2 \cdot 10^{-3} \cdot P_{stack\_req} \cdot n_{cells}}{2 \cdot F \cdot V_{stack}} \tag{3.5.36}$$

The FC stack and FCS efficiencies can be estimated using equations eq. 3.5.37 and eq. 3.5.38, respectively. By implementing the FCS model across all 11 polarization curves, which range from 0% to 10% FC SOH degradation, the efficiency curves were derived for both the FCS and FC stack, as illustrated in fig. 3.35 and fig. 3.36.

$$\eta_{FCS} = \frac{P_{FC\_stack} - P_{FC\_acces}}{P_{H_2\_rlsd}} \tag{3.5.37}$$

$$\eta_{stack} = \frac{P_{FC\_stack}}{P_{H_2\_rlsd}} \tag{3.5.38}$$

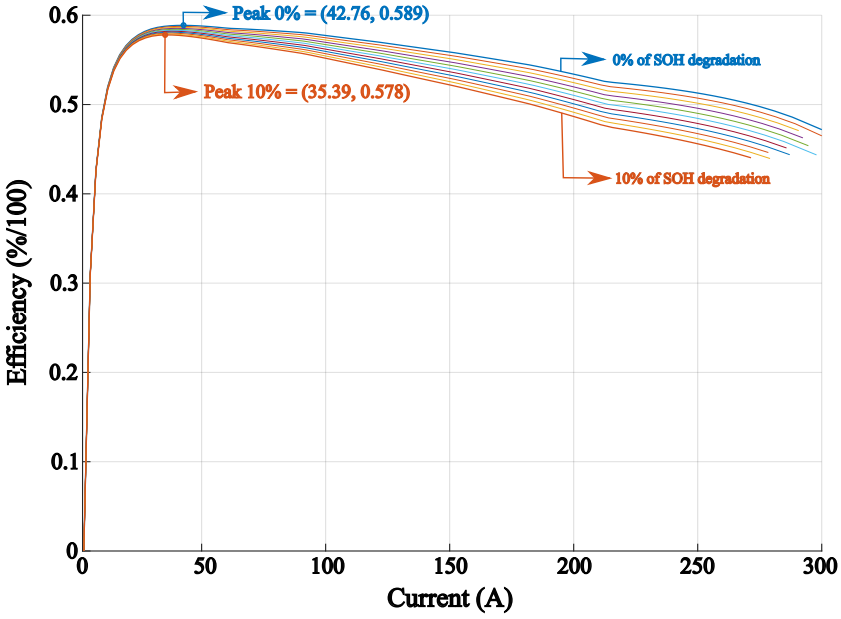

Figure 3.35: FCS efficiency curves at different stages of SOH degradation

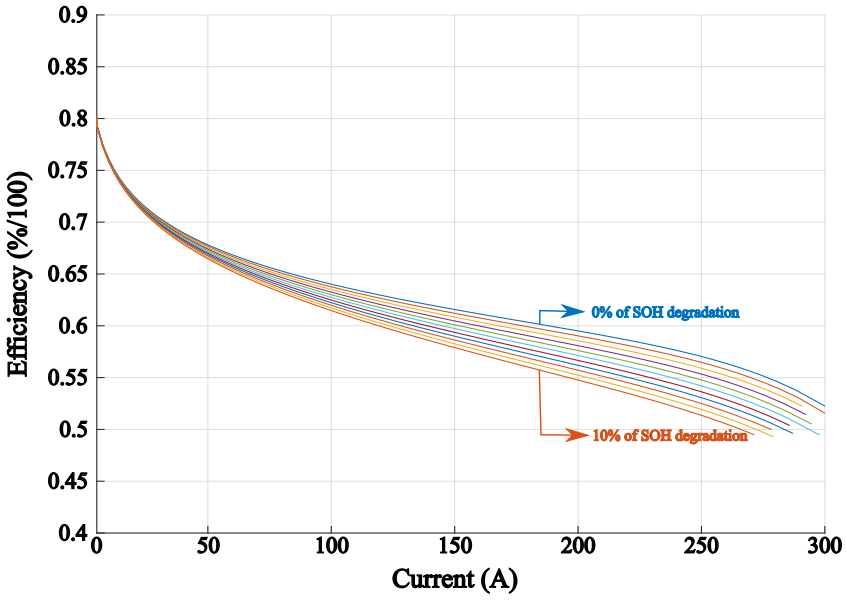

Figure 3.36: FC stack efficiency curves at different stages of FC SOH degradation

Besides utilizing the polarization curves as a 2-D LUT and incorporating the previously described FC SOH model, the FC stack subsystem calculates the total energy generated by the FC stack using eq.3.5.39.

$$E_{FC\_stack} = \int I_{stack} \cdot V_{stack}\, dt \tag{3.5.39}$$

3.5.3 Hydrogen tanks

The hydrogen tank subsystem was modelled to estimate the vehicle's hydrogen consumption. To calculate the total hydrogen consumption for each run of a drive cycle, eq. 3.5.40 derived from reference [71], was employed, where the number 0.98 is used to consider the FC converter efficiency. A 2-D LUT generated from the FCS efficiency curves was also used.

In the main vehicle model, the efficiency, denoted as η_{FCS} in the main vehicle model depends on the FC stack current and its SOH degradation level, as shown in eq.3.5.41.

$$m_{H_2} = \int_0^{t_{dc}} \frac{P_{FC\_stack}}{\eta_{FCS} \cdot 0.98 \cdot LHV} dt \tag{3.5.40}$$

$$\eta_{FCS} = f(I, FC_{SOH}) \tag{3.5.41}$$

Given that the vehicle's total hydrogen carrying capacity is 4400 g, the percentage of remaining hydrogen is calculated using eq.3.5.42.

$$H_2\% = \left[1 - \left(\frac{m_{H_2}}{4400}\right)\right] \cdot 100 \tag{3.5.42}$$

The total chemical energy derived from the hydrogen consumed during the drive cycle run is utilized to calculate the model error, which will be explained in the subsection "Main vehicle model validation". This value is determined using eq. 3.5.43. Lastly, the hydrogen tanks subsystem modelled can be seen in fig. 3.37.

$$E_{chem\_H_2} = \int_0^{t_{dc}} \frac{P_{FC\_stack}}{\eta_{FCS} \cdot 0.98} dt \tag{3.5.43}$$

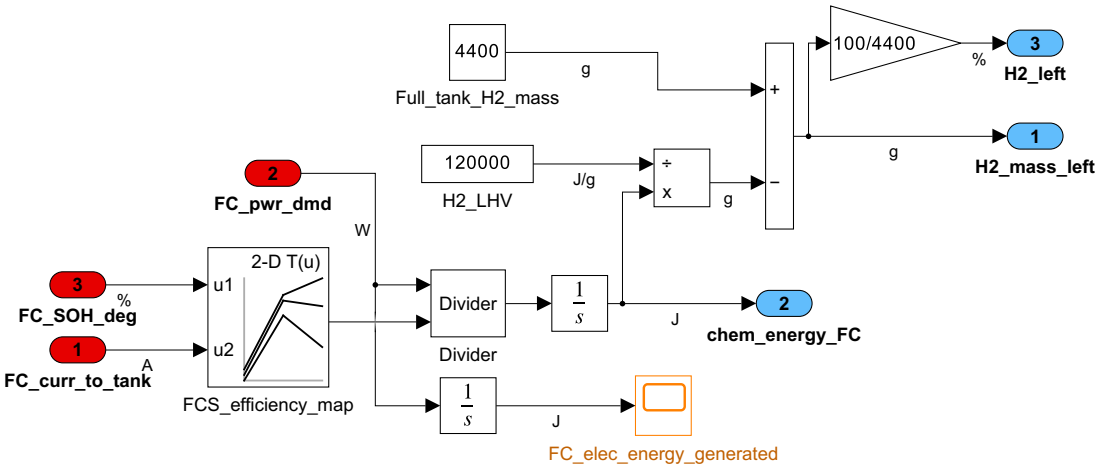

Figure 3.37: Hydrogen tanks subsystem

3.5.4 Battery pack

The battery pack subsystem is designed with four inputs and three outputs. The inputs consist of the total power demand, the operation mode, the overall power generated by the FC stack, and the specific portion of FC power dedicated to charging the battery. On the output side, the subsystem calculates the battery voltage, the SOC, and the total energy the battery produces. This subsystem calculates the battery's SOH degradation, which is used to estimate the outputs.

The total power demand of the vehicle is the sum of the electric accessories and the EM power demands. The quantification of these values will be explained further. The controller subsystem determines the operation mode and will be thoroughly detailed in a subsequent chapter. All these inputs compute the total power output required from the battery. This is called the battery power P_{batt}.

The well-known eq. 3.5.44 calculates the battery voltage. Meanwhile, the battery current, denoted as I_{batt}, is determined using the voltage from the previous time step of the simulation, as elucidated in eq. 3.5.45.

$$V_{batt} = V_{OCV} - (I_{batt} \cdot R_{batt}) \tag{3.5.44}$$

$$I_{batt} = \frac{P_{batt}}{V_{batt\_-1}} \tag{3.5.45}$$

The battery's resistance and OCV are meticulously calculated using 2-D LUTs that depend on the battery's SOC and SOH. The curves of these values were obtained experimentally using the Samsung 30-T cell. The parameters of this cell type are shown in table 3.9 [72].

Table 3.9: Samsung 30T cell specifications

Cell parameter	**Value**	**Unit**
Nominal voltage	3.6	V
Maximum voltage	4.2	V
Nominal capacity	3000	mAh
Maximum discharge continuous current	35	A

The battery pack was modelled by combining cells to get a peak voltage close to 400 V and an energy capacity close to the one shown in table 3.2 (10.5 kWh). The battery pack specifications are shown in table 3.10.

Table 3.10: Battery pack specifications

Parameter	**Value**	**Unit**
cells in series	96	-
cells in parallel	10	-
Peak voltage	403.2	V
Energy capacity	10.8	kWh

Figs. 3.38, 3.39, and 3.40 illustrate the OCV map, the discharging resistance map, and the charging resistance map, respectively. These are maps for the battery pack after using the simple formulas shown in eq. 3.5.46, where n_s and n_p represent the number of cells in series and parallel in the battery pack.

$$\begin{cases} V_{OCV} = V_{cell\_OCV} \cdot n_s \\ R_{batt} = \frac{R_{cell} \cdot n_s}{n_p} \end{cases} \tag{3.5.46}$$

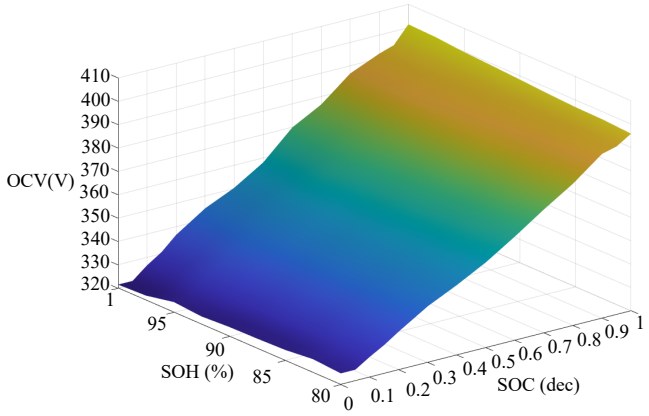

Figure 3.38: Battery pack OCV for multiple SOH degradation levels

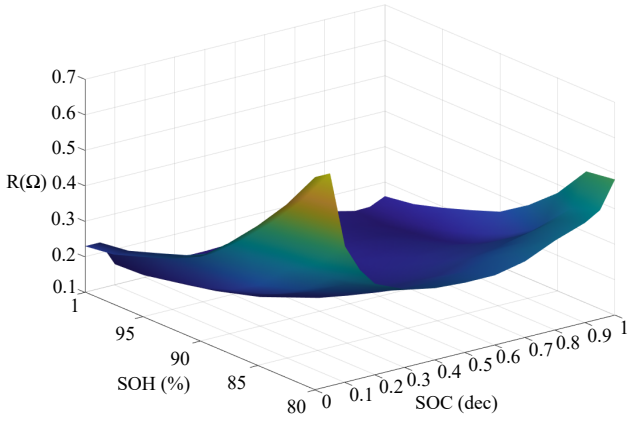

Figure 3.39: Battery pack discharge resistance curves for multiple SOH degradation levels

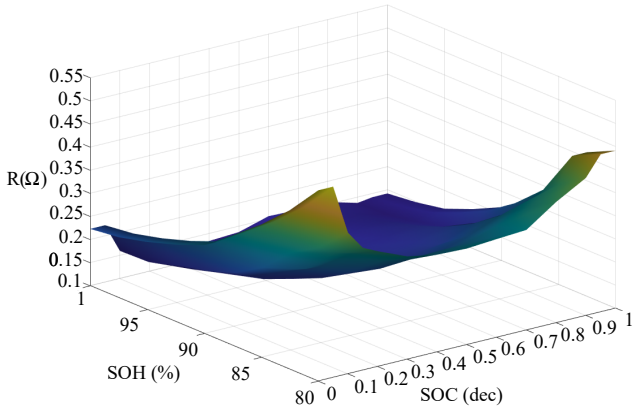

Figure 3.40: Battery pack charge resistance curves for multiple SOH degradation levels

To estimate the SOC of the battery eq. 3.5.47 below is used, where C_i is the initial capacity of the battery pack, and SOC_{batt_i} is the battery pack SOC at the beginning of the simulation.

$$SOC_{batt} = \frac{(C_i \cdot SOC_{batt\_i}) - \int I_{batt}\, dt}{C_i} \tag{3.5.47}$$

The Ah-throughput method, based on the Arrhenius equation, dynamically updates the battery's SOH degradation over time. This approach has been effectively employed in several studies, notably referenced in [73], [74], and [75]. Notably, the empirical parameters utilized here were derived from [75], where a lithium-ion cell with a chemical composition similar to the Samsung 30T was used to extract these parameters.

According to the method described, the SOH degradation of battery cells is influenced by the c-rate c and the operating temperature T, as detailed in eq. 3.5.48. In this equation, SOH_i (100%) is the SOH of the battery at the BOL, while the

term $S\dot{O}H(c,T)$ inside the integral is defined by eq. 3.5.50 and represents the SOH depletion after each simulation time step.

$$SOH_{batt} = SOH_i - \int S\dot{O}H(c,T)\, dt \tag{3.5.48}$$

In eq. 3.5.50, the number 0.2 is used for considering that the EOL of the battery occurs when the battery SOH (SOH_{batt}) reaches 0.8 (20% of degradation). Moreover, the factor 3600 converts the time unit from h^{-1} to s^{-1}.

To effectively apply the proposed degradation estimation method, it is crucial to calculate the number of cycles $N(c,T)$ the battery can undergo before reaching its EOL. This involves determining the battery capacity loss percentage, which can be performed using eq. 3.5.49. This degradation equation must be solved for Ah_{tp} by substituting $\Delta Ah_{batt\%}$ for 0.2, representing the maximum allowable capacity loss. $B(c)$ represents an empirical pre-exponential factor estimated from the data presented in 3.11 [75], and z and A_f are the power law factor and ageing factor, respectively, defined in the same table.

$$\Delta Ah_{batt\%} = B(c) \cdot e^{\frac{-A_f(c)}{T}} \cdot Ah_{tp}^{z} \tag{3.5.49}$$

Table 3.11: Lithium-ion cell SOH degradation empirical parameters

Parameter	**Value**	**Unit**
Ageing factor	3814.7 - 44.6c	K
Power law factor	0.55	-
Temperature	298	K

The term $N(c,T)$ can now be measured using eq. 3.5.51, where Ah_{batt} represents the battery nominal capacity defined from table 3.9, and $Ah_{tp}(c,T)$ refers to the Ah-throughput the battery experiences during operation.

$$S\dot{O}H(c,T) = 0.2\frac{c}{3600 \cdot N(c,T)} \tag{3.5.50}$$

$$N(c,T) = \frac{Ah_{tp}(c,T)}{2 \cdot Ah_{batt}} \tag{3.5.51}$$

The last output of the battery pack subsystem, the total battery energy generated, is used to estimate the energy balance of the model. This value is measured using the battery's voltage and current, as detailed in eq.3.5.52.

$$E_{batt\_gen} = \int (V_{batt} \cdot I_{batt})\, dt \tag{3.5.52}$$

3.5.5 Electric motor

The EM employed in this study is the YASA P400HC, which operates at a DC bus voltage of 400 V. Allca-Pekarovic et. al. provided a characterization of this motor in [76], and their findings are used here to compute the EM torque and efficiency using LUTs. Illustrations of the torque curve and efficiency map are shown in fig. 3.41 and fig. 3.42, respectively.

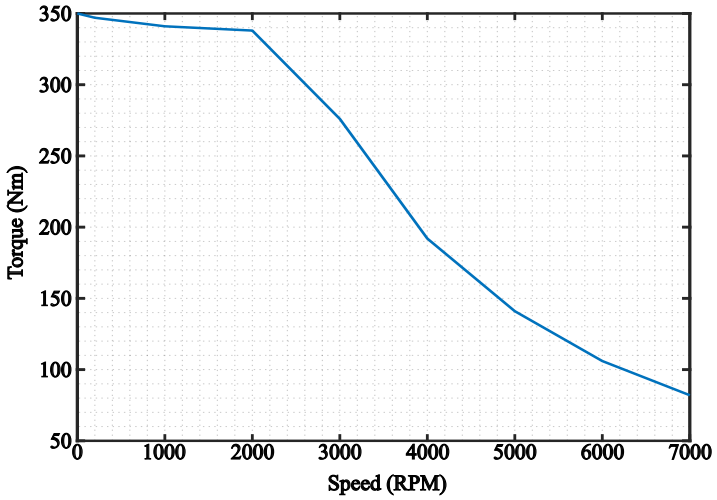

Figure 3.41: YASA P400HC torque curve

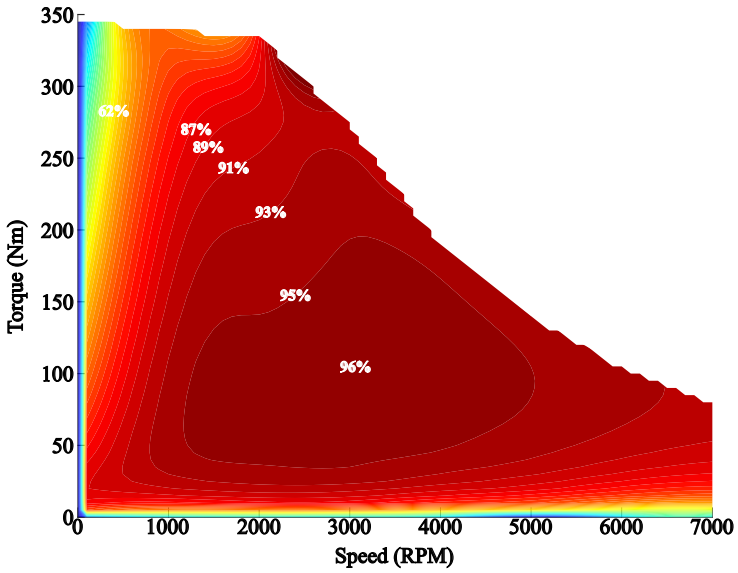

Figure 3.42: YASA P400HC efficiency map

The inputs of the EM subsystem are the controller torque demand, the battery voltage from the battery subsystem, and the final drive speed from the final drive subsystem. The outputs generated are the EM speed (same as the final drive), torque,

inertia, current, power, and total energy loss during the drive cycle.

The EM inertia is fixed at 0.1 $kg \cdot m^2$, and the torque is defined based on the torque range for the specific speed needed for the EM. This torque is then multiplied by the speed, and the signal of the results defines how the electric power is calculated, as shown in eq. 3.5.53. The eq. 3.5.54 and eq. 3.5.55 compute the EM current and the total EM energy loss, respectively.

$$\begin{cases} P_{em\_el} = \frac{P_{em\_mech}}{\eta_{em}}, P_{elec} > 0 \\ P_{em\_el} = P_{em\_mech} \cdot \eta_{em}, P_{elec} <= 0 \end{cases} \tag{3.5.53}$$

$$I_{em} = \frac{P_{em\_el}}{V_{batt}} \tag{3.5.54}$$

$$E_{em\_loss} = \int P_{em\_el} - P_{em\_mech}\, dt \tag{3.5.55}$$

3.5.6 Electric accessories

The electric accessories power demand is estimated at 500 W while the vehicle operates. Therefore, its energy consumption can be measured using eq. 3.5.56. Additionally, this power demand is combined with that of the EM to determine the total power demand of the vehicle.

$$E_{elec\_acces} = \int 500\, dt \tag{3.5.56}$$

3.5.7 Final drive

The final drive subsystem has three inputs and four outputs. The inputs include the EM inertia, the EM torque delivered from the EM subsystem, and the wheel angular speed coming from the wheels subsystem. The outputs include the powertrain's equivalent inertia, defined in eq. 3.5.57, the final drive torque, speed, and total energy loss. In eq. 3.5.57 both J_{em} and J_{fd} are equal to 0.1 $kg \cdot m^2$, and fd is the final drive ratio.

$$J_{fd\_out} = (J_{em} \cdot fd^2) + J_{fd} \tag{3.5.57}$$

The final drive ratio is defined as 6.5 based on the maximum torque of the EM and the maximum speed needed for the vehicle modelled. The maximum speed of the Opel Vivaro is 130 km/h, while the maximum speed of the drive cycles analyzed is 131.3 km/h in the WLTP. The final drive was modelled to make the vehicle reach 139 km/h (ω_{wheel_max} = 112.78 rad/s) to improve the car's robustness in different speed conditions. The eq.3.5.58 defines the final drive ratio fd, where ω_{em_max} is 7000 RPM (732.67 rad/s).

$$fd = \frac{\omega_{wheel\_max}}{\omega_{em\_max}} \tag{3.5.58}$$

The final drive torque is estimated by multiplying the EM torque T_{em} by the final drive efficiency (97%). The final drive speed is the wheel angular speed multiplied by the final drive ratio fd, and the final drive total energy loss is defined by eq. 3.5.59.

$$E_{fd} = \int (\omega_{fd} \cdot T_{em} \cdot (1 - 0.97))dt \tag{3.5.59}$$

3.5.8 Wheels

The tire selected for the FCEV model is the LT215/65R16. Its dimensions are illustrated in fig. 3.43.

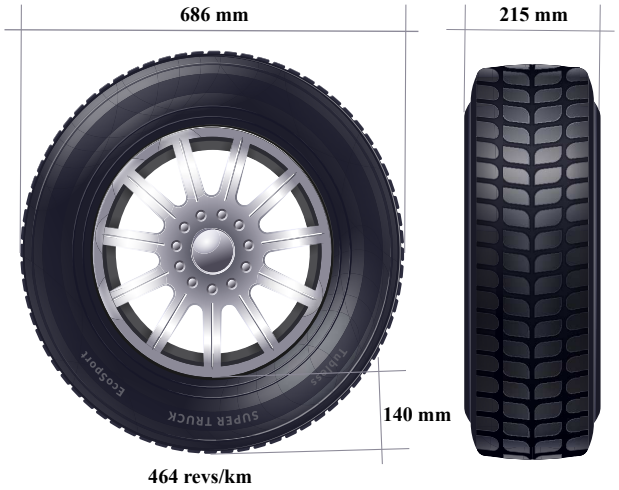

Figure 3.43: Tire dimensions

In the wheels subsystem, there are five inputs and five outputs. The inputs include the torque of the friction brake (the portion not converted into energy by regenerative braking), the vehicle move demand (set to 1 for movement and 0 for a stop), the final drive torque, the final drive inertia, and the vehicle speed from the chassis subsystem. The outputs consist of the equivalent mass, the wheel angular speed, the net force on the wheel, the rolling resistance force, and the total energy lost due to the friction brakes over the drive cycle.

The equivalent mass is defined by eq. 3.5.60, where J_w represents the inertia of each wheel, and r_w is the deformed radius of the wheels. The deformed radius is calculated as the radius depicted in fig. 3.43, adjusted by a factor of 0.95 to account for the deformation the wheels suffer due to the car's weight.

$$m_{eq} = \frac{J_{fd\_out} + (4 \cdot J_w)}{r_w^2} \tag{3.5.60}$$

The wheels' angular speed and net force are defined by eq. 3.5.61 and eq. 3.5.62, respectively. In eq.3.5.62 F_w is the force transmitted to the wheels, while F_r denotes the portion lost due to the tires' rolling resistance.

$$\omega_w = \frac{v}{r_w} \tag{3.5.61}$$

$$F_{wheel} = F_w - F_r \tag{3.5.62}$$

The total rolling resistance of the wheels is determined by eq. 3.5.63, which incorporates C_h, the surface friction coefficient. Given that the road along the drive cycle is flat and the surface is characterized as worn asphalt, α is assigned a value of 0, and C_h as 1.5 [77]. Then, the eq. 3.5.63 can be simplified and represented by eq. 3.5.64.

$$F_r = m_v \cdot g \cdot cos(\alpha) \cdot (0.0041 + 0.000018v) \cdot C_h \tag{3.5.63}$$

$$F_r = m_v \cdot g \cdot (0.00615 + 0.000027v) \tag{3.5.64}$$

The energy dissipated through the friction brakes is quantified by eq. 3.5.65, and this measurement is utilized to validate the model in the 'Main Vehicle Model Validation' subsection.

$$E_{fb} = \int \frac{-T_{fb} \cdot v}{r_w} dt \tag{3.5.65}$$

3.5.9 Chassis

In the chassis subsystem, there are two inputs and three outputs. The inputs include the wheel force and the equivalent mass derived from the wheel subsystem. The outputs include the drag force, the vehicle's speed, and the total energy used to accelerate the vehicle.

To calculate the drag force, eq. 3.5.66 is employed, where ρ_{air} represents the air density (1.23 kg/m^3), v is the vehicle speed, C_D is the drag coefficient, and A is the vehicle frontal area.

$$F_D = \frac{\rho_{air} \cdot v^2 \cdot C_D \cdot A}{2} \tag{3.5.66}$$

The sum of the drag force and rolling resistance is called road load loss, and the energy to surpass these losses, defined by eq. 3.5.67 and called here 'road load energy loss,' is used to validate the main vehicle model.

$$E_{RDL} = \int (F_D + F_r) \cdot v \; dt \tag{3.5.67}$$

The frontal area A of the vehicle was determined to be 2.1753 m^2, based on the dimensions of the Opel Vivaro as presented in fig. 3.44. Furthermore, consistent with discussions in [78], the drag coefficient for a vehicle with a frontal area similar to that of the Vivaro and a mass from 1700 to 2000 kg is estimated to be between 0.28 and 0.33. Therefore, C_D was defined here as 0.31.

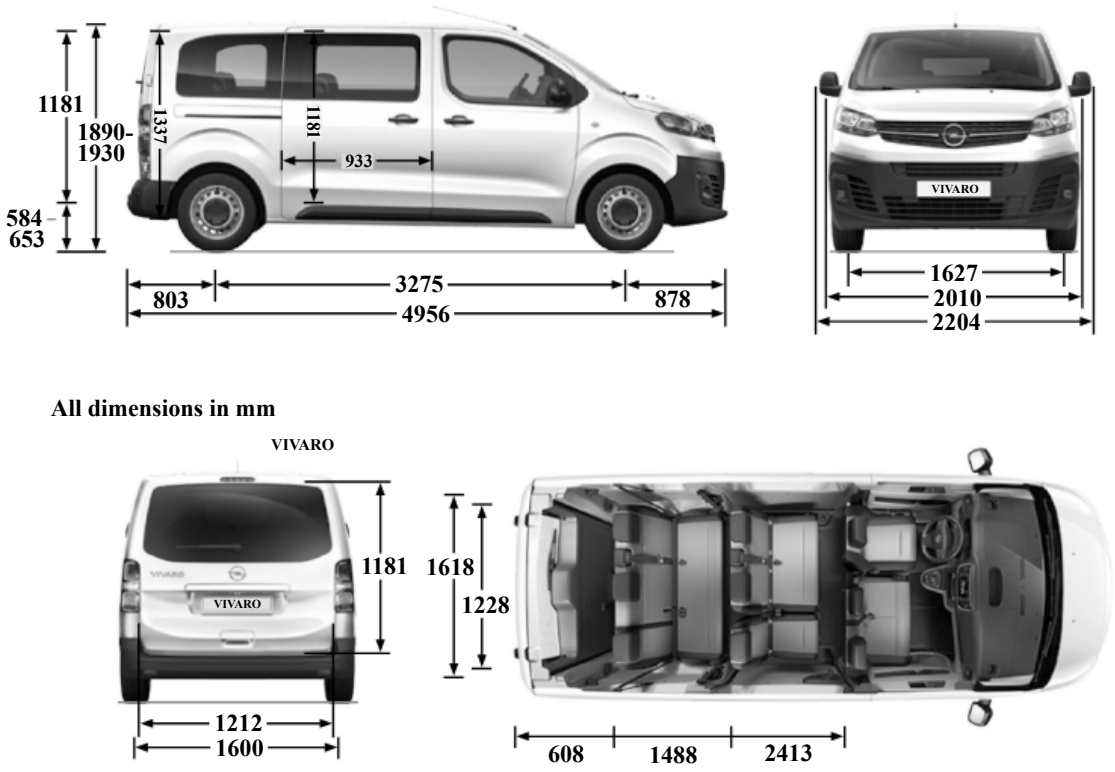

Figure 3.44: Opel vivaro dimensions [3]

Besides the losses, a portion of the energy accelerates the vehicle. This energy can be quantified using eq. 3.5.68, essential for estimating the error in the main vehicle model. In this equation, F_{net} is the net force, defined as the difference between the force in the wheel to propel the car and the drag force, as specified in eq. 3.5.69.

$$E_{accel} = \int (F_{net} \cdot v) dt \tag{3.5.68}$$

$$F_{net} = F_{wheel} - F_D \tag{3.5.69}$$

The vehicle speed is calculated by integrating the acceleration, as defined in

eq.3.5.70, where m_{eq} represents the equivalent mass coming from the wheel subsystem.

$$v = \int \frac{F_{net}}{m_{veh} + m_{eq}} \tag{3.5.70}$$

3.5.10 Main vehicle model validation (energy balance)

To validate the main vehicle model, the energy balance method is employed. This method implies that the total energy consumed and generated inside the model should closely align. A significant discrepancy between these values (error) indicates a potential logical mistake in the model or a large time step.

To model the energy balance in the main vehicle model, the following parameters are used: The total energy generated by the FC E_{FC_stack}, the total energy generated by the battery (which includes the regenerated energy) E_{batt_gen}, the total energy loss of the EM E_{em_loss}, the total energy consumed by the electric accessories E_{elec_acces}, the road load energy loss (the drag and rolling resistance losses) E_{RDL}, the energy utilized to accelerate the vehicle E_{accel}, the energy loss from friction brakes E_{fb}, and the final drive energy loss E_{fd}. The eq. 3.5.71 summarizes the main vehicle model error measured using the energy balance.

$$Error_{\%} = \frac{E_{FC\_stack} + E_{batt\_gen} - E_{em\_loss} - E_{elec\_acces} - E_{RDL} - E_{accel} - E_{fb} - E_{fd}}{E_{FC\_stack} + E_{batt\_gen}} \tag{3.5.71}$$

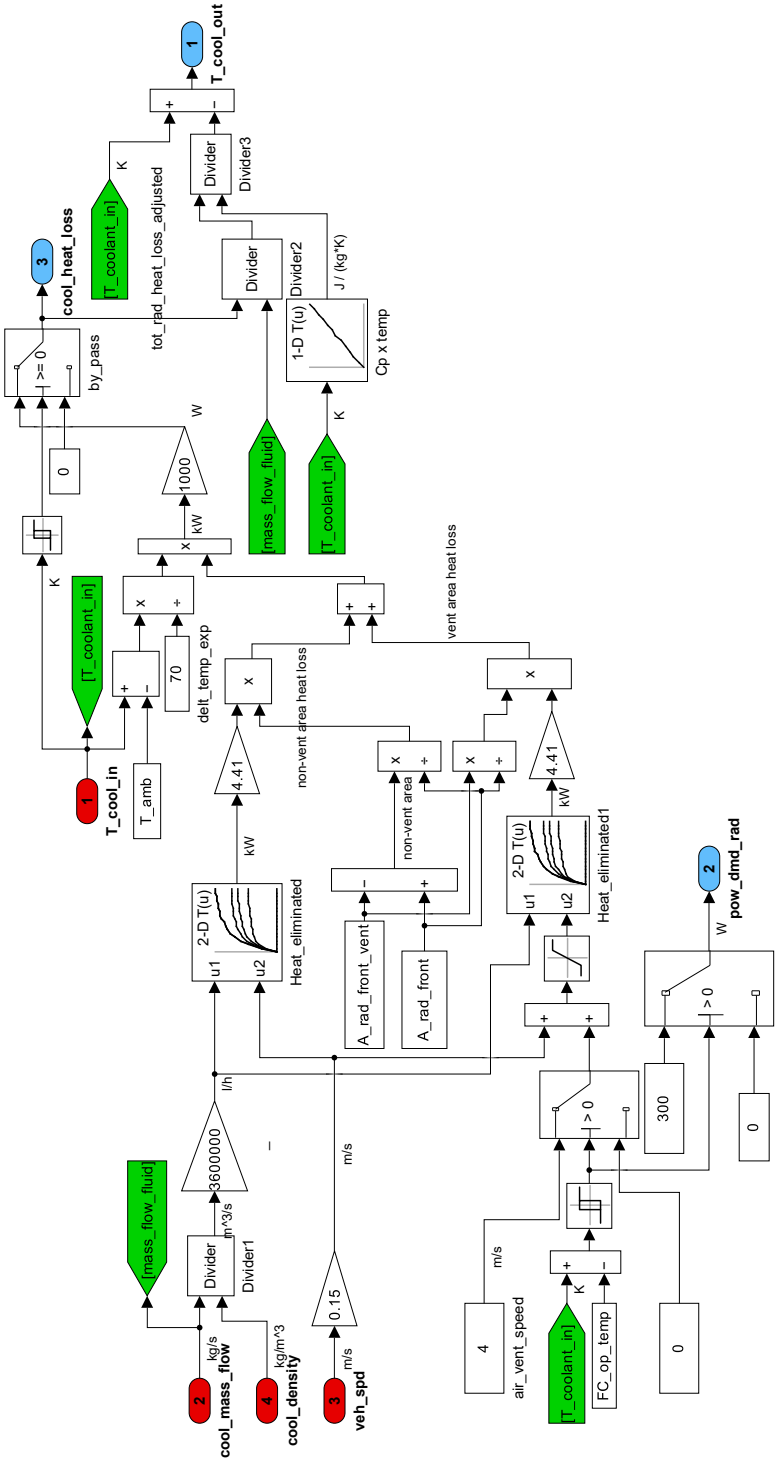

Figure 3.34: Radiator subsystem

Chapter 4

Energy Management Systems for Fuel Cell Electric Vehicles

Controlling an electrified vehicle essentially includes two groups of tasks. The first is the low or component-level control task, where each powertrain component is controlled by utilizing feedback control methods. The second one, high or supervisory control, optimizes the vehicle's energy flow while maintaining the battery SOC within a certain range of operation.

The high-level control, or EMS, receives and processes information from the vehicle (as EM rotational speed) and the driver (as vehicle speed and acceleration demand) to define a control action that is sent to the low-level control layer, which uses it to define the low-level control tasks (as the operation of the actuator). It is also responsible for selecting the best mode of operation in vehicles with multiple power sources (start-stop, power-split, etc.) [78].

Among the different energy management strategies available in the literature, two overall trends that address the energy management challenge include rule-based

and model-based optimization methods. A key feature of rule-based approaches is their efficacy in real-time scenarios. They do not involve explicit minimization or optimization but rely on rules to decide the control action to be applied.

Rules are usually chosen based on heuristics, intuition, or knowledge of the best global solutions generated with mathematical models using optimization algorithms or codes. In a model-based optimization strategy, the optimal control decisions are determined by minimizing a cost function over one specific and known driving cycle, which leads to a near-global optimal solution [78].

Although model-based optimization control methods are not applied directly in real-time (due to their preview nature and computational complexity), they constitute a valuable design tool, as they can be used to design rules for online implementation and as a benchmark. It has been seen that adopting systematic model-based optimization methods using specific objective functions to improve the energy management controllers is a good approach to getting near-optimal results in developing an EMS for the vehicle [78].

The EMS aims to determine the optimal power split between the available energy sources, but what is optimal depends on what must be optimized. In most cases, the chosen strategies focus on minimizing fuel consumption, but optimization objectives can also be minimizing pollutant emissions, maximizing battery life, or finding the best balance between multiple goals. In the case of FCEVs, it can also include the FC life.

4.1 Rule-based Energy Management Strategies

The Fuzzy Logic Controller (FLC) is a rule-based EMS that uses rules to find relations between some inputs and outputs of the controller using if-then conditions [79].

A real-time fuzzy logic strategy for FCEVs is developed in [80] to diminish FC and battery degradations while optimizing fuel consumption. In this study, the authors suggested four operational modes.

The first mode starts the vehicle with the battery solely. The second mode is charging, where the FC system independently powers the FCEV. When the SOC falls below a specified threshold, and the requested power falls within the allowed range of the FC output power, the FC meets the power demand and concurrently recharges the battery. The third mode is the FC and battery driving mode, where both the FC and the battery fulfill a portion of the power requirements to meet the driver's needs. Lastly, the fourth mode is regenerative braking, where the battery is recharged through the recovered car's inertia energy, with the EM working as a generator. This inertia energy is not entirely recovered, as part of it is dissipated through the mechanical brake of the vehicle [80].

This work optimized the fuzzy logic controller using a genetic algorithm (GA) and actual driving data. The controller developed uses the vehicle speed, the vehicle's demanded power and battery SOC as inputs, while the required power from the FC system is the output [80].

Researchers in reference [81] compared two control strategies in an FCEV: a range extender and a Fuzzy logic optimized control strategy. The optimization process was executed using GA, similar to the approach used in [80]. The range extender control strategy uses a constant current supply to recharge the battery when the SOC reaches

45%, and stop charging it when the SOC reaches 70%. These specific SOC thresholds were selected based on two primary objectives: minimizing the FC's frequent start-stop cycles to mitigate its degradation and limiting the battery degradation by avoiding significant depth of discharge. Fig. 4.1 illustrates the mentioned range extender control strategy and associated SOC boundaries in a graphical representation.

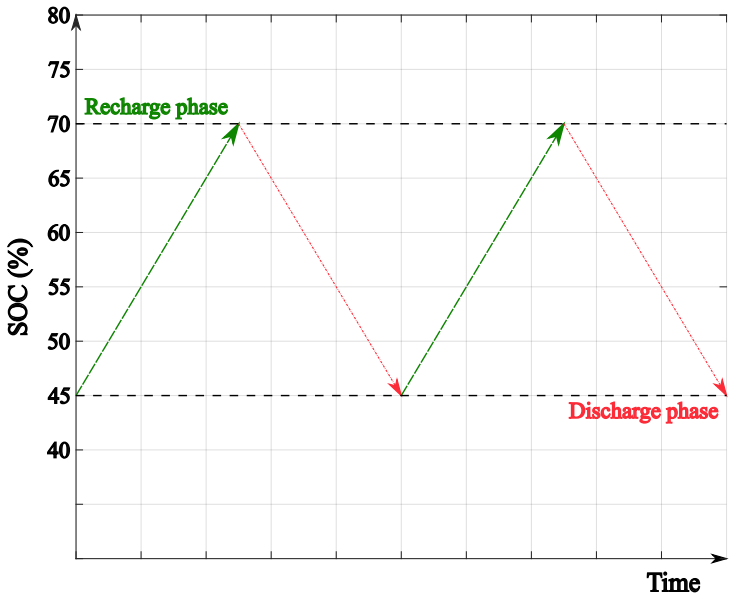

Figure 4.1: Fuel cell range extender SOC profile

About the FLC used, the inputs are the power demand of the vehicle and the battery SOC, and the output is the FC power. The only difference from the FLC in [80] is that the speed is not used as input in this case. In the results section, the authors present a comparative analysis of the control strategies, with the fuzzy control strategy enabling a range of 505 km. In comparison, the range extender control method achieved a maximum range of 485 km under the same conditions, which includes identical battery specifications, FC stack parameters, and hydrogen

mass (10 kg). In other words, the FLC strategy consumed 1.978 kg of hydrogen, while the range extender strategy consumed 2.067 kg.

It is essential to highlight that the average energy consumption results shown in [81] were validated using experimental data demonstrated in [82]. In this study, the authors reported an average energy consumption ranging from 0.7 to 0.8 kWh/km based on their experimental analysis. In contrast, in reference [81], a 0.661 kWh/km energy consumption was reported for a similar light-duty commercial vehicle.

In another study, an FC SOH-aware FLC was optimized using a GA [83], but with the primary objective of finding a harmonious balance between FC durability and the hydrogen economy. The findings show an intrinsic connection between the FCS's efficiency and the FC's net output power.

The FLC inputs and outputs presented in [83] are similar to those of [81]. For both the SOC and vehicle power demand are used as inputs and the FC power is the output. The only difference is that in [81], the FC power range is discretized into seven possible levels, while in [83], a total number of five is used. It opens more possibilities for tuning the FLC in [81].

The authors of [84] investigated the multi-objective sizing of components within an FC powertrain with an FC stack and a battery. They analyzed a Fuel Cell Electric Bus (FCB) based on some critical components. The multi-objective function employed accounts for fuel economy, battery SOH degradation, and FC SOH degradation.

Then, a two-loop framework is proposed, and an optimal EMS based on DP results is employed in the inner loop for each set of powertrain parameters. Various FC combinations and battery sizing were evaluated in the outer loop to identify a Pareto-optimal solution. The best solution is shown in their findings.

The FC lifetime formula used in [84] is the same as eq. 3.5.10 but uses different parameters. The parameters used are shown in table 4.1.

Table 4.1: FC aging coefficients

Coefficient	**Description**	**Value**	**Condition**
k1	Idling degradation	0.00356(h^{-1})	Output power less than 10% of rated power.
k2	Start-stop degradation	0.00196($cycle^{-1}$)	One start and one stop.
k3	Dynamic load degradation	0.00126(h^{-1})	Absolute value of the power change rate is larger than 10% of rated power per second.
k4	High load degradation	0.00147(h^{-1})	Higher than 90% of maximum rated power.
kp	On-road systems aging coefficient	1.47	

Given that the battery works without consuming hydrogen directly, it must use a methodology that considers the energy consumption of both the hydrogen consumed by the FC and the equivalent hydrogen consumption from the electricity utilized by the battery. If the battery were consistently maintained in a charge-sustaining state throughout its operation period, the FC's hydrogen consumption could be considered the equivalent energy consumption [84]. However, this scenario does not accurately reflect reality. Therefore, to evaluate fuel economy while considering the energy consumption of the battery, the concept of powertrain equivalent energy consumption is

used [84].

In [85], an FLC is implemented within an FC/battery powertrain featuring a variable-structured battery. The method optimizes battery performance by altering the series and parallel connections between battery sets based on charging or discharging states. The critical role of this battery pack characteristic is its capacity to absorb excess power and supply deficient power to the overall system. Configuration changes are made through switches capable of opening or closing to establish different battery set connections.

The FLC of [85] is then compared to a deterministic FLC. Unlike the deterministic controller, which prescribes a specific power output for each operational mode without considering the dynamic constraints of the FCS, the incremental FLC adjusts the power outputs even when working in the same operation mode. The failure to consider these dynamics may induce abrupt power fluctuations in the FCS, leading to anode or cathode starvation of reactants. These sudden power changes must also impact the FC SOH degradation, which is not analyzed in this study.

The incremental FLC in [85] imposes a power change limit of 4 kW/s to avoid the mentioned abrupt transitions. Results indicate that the incremental FLC maintains a battery SOC close to a constant value, particularly during drive cycles characterized by high power demand fluctuations. The incremental FLC also limits the FC operation to a high-efficiency region. The operational modes used are start mode, FC mode, battery charge, hybrid power, braking, and parking, constituting six distinct operational states. The mode selected is defined based on inputs of battery SOC, power required from the vehicle, and previous FC power output.

Usmanov et al. [86] utilized experimental data from the first generation of the FC

Toyota Mirai provided by the ANL [87] [88] to develop a simulation model and analyze various control strategies. In this study, the FC main maps, crucial for analyzing the performance of an FCEV, were not modelled based on formulas. Instead, points from the maps generated through the experimental tests (the FC stack efficiency map, FCS efficiency map, polarization curve, and hydrogen mass flow rate) were used. In this study, a polynomial approximation was employed to capture the shape of these graphs.

Regarding the control strategies implemented in [86], a rule-based approach was developed to ensure that the modelled Toyota Mirai operation closely reproduces the experimental testing outcomes. This rule-based strategy encompassed six modes of operation, which are different than what is found in the literature: Regenerative braking (mode 1), Load shift (mode 2), Only battery (mode 3), FC driving/low power (mode 4), FC driving/high power and low SOC (mode 5), and FC driving/high power and high SOC (mode 6). A description of the rules used is shown in table 4.2. The equations governing the power split for mode six are detailed in [86].

The Usmanov et al. strategy's performance varies across the drive cycles. While the differences in hydrogen consumption and SOC final values for the WLTC were minimal, with 0.5% and 1%, respectively, the discrepancies were higher for UDDS, reaching 18.1% in hydrogen consumption. The authors mention that the model's reliance on steady-state laboratory testing-derived maps needs to capture transient behaviors properly, highlighting the need for more complex models to surpass the current map-based approach and enhance simulation fidelity.

Luciani et al. [89] compared the efficacy of various rule-based strategies employed in an FCEV with an FC/battery topology. The analysis involved two main criteria:

Table 4.2: Rule-based modes of operation developed for the FC Toyota Mirai 2016

Mode	**Power demand**	**Battery SOC**	**Power Split**	**Description**
1	–	–	$P_{req} = 0\ kW$; $P_{bat} = P_{req}$	
2	$0 < P_{req} < 7\ kW$	$< 57\%$	$P_{fc} = 7\ kW$; $P_{bat} = P_{req}$ - $7\ kW$	The FC stack produces at least $7\ kW$ to avoid low efficiency zone.
3	$0 < P_{req} < 7\ kW$	$>= 57\%$	$P_{req} = 0\ kW$; $P_{bat} = P_{req}$	FC is turned off in this mode.
4	$0 < P_{req} < 11\ kW$	–	$P_{fc} = P_{req}$- P_{aux}; $P_{bat} = P_{aux}$	The FC stack provides the traction power for any battery SOC.
5	$11\ kW < P_{req}$	$< 57\%$	P_{fc}= P_{req}- P_{aux}; $P_{bat} = P_{aux}$	
6	$11\ kW < P_{req}$	$>= 57\%$	$P_{fc} = \mathrm{f}(P_{req})$; $P_{bat} = P_{req}$-P_{fc}	Described by complex linear equations [86]

FC efficiency and equivalent fuel consumption.

The first strategy in [89], the "constant power" strategy, starts with the battery generating the total power required by the driver while the FC remains idle. Then, once the battery SOC depletes to a predetermined threshold, the FC engages, providing constant power until the drive cycle ends. The second approach, termed the "Baseline Mode-based" strategy, uses a rule-based framework where the power output from the FC stack can provide power values from 0 to 50 kW. These values depend on the battery SOC and the total power demand. Finally, an FLC is deployed as the third strategy, whereby the battery SOC and the driver's power demand are used as inputs, with the FC power required being the output. The initial battery SOC across all scenarios is consistently set at 60%.

To ensure a comprehensive analysis, the simulations were conducted in low-load drive cycles, such as FTP, NEDC, and UDDS, and high-load drive cycles, such as US06 and WLTP. Comparative plots were generated across five distinct drive cycles to facilitate result comparisons, shown in fig. 4.2.

The findings reveal that, in the context of the WLTP drive cycle, fuel consumption levels for the Baseline Mode-based and FLC strategies are similar and surpass those of the constant power strategy. Moreover, across all other drive cycles, the FLC methodology consistently demonstrates the lowest fuel consumption. Regarding FCS efficiency analysis, the constant power and fuzzy-logic control methods exhibit similar results, outperforming those achieved through the Baseline Mode-based approach.

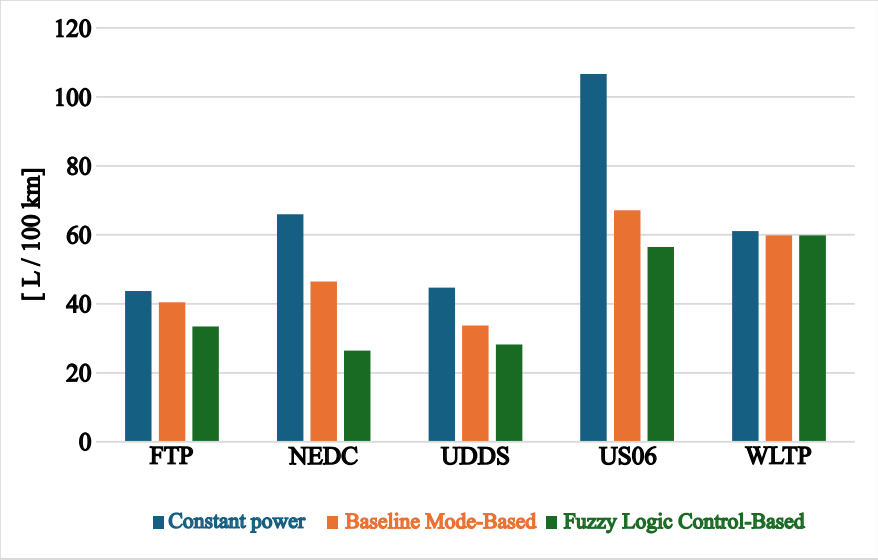

Figure 4.2: Fuel consumption for different real-time implementable EMSs

Notably, it is highlighted in this study that all strategies were categorized as

charging-sustaining. However, the FLC best maintains the battery SOC at a near-constant level. Furthermore, it is emphasized that future investigations should consider the lifetime of FCEV components [89]. Given the high influence of power dynamics on FC longevity, the FLC method may yield inferior outcomes. Thus, constraints associated with FC power dynamics could be included in the strategies for more comprehensive analyses concerning FC component longevity.

As done in other previous studies mentioned here, Yuan et al. [90] propose an optimized rule-based EMS, utilizing GA as the optimization method for the powertrain of an FCEV. The refinement of rules within this EMS is guided by criteria focusing on enhancing FC durability, battery charge sustenance, and fuel economy. The inputs utilized for power distribution decisions within the rule-based EMS, including power demand and battery SOC, are considered, and some additional ones, different from the previously mentioned, were also used. These additional ones include FC efficiency and FC power constraints, as they are essential in mitigating reactant starvation and avoiding abrupt degradation of the FC SOH.

Although the GA method utilized in [90] for optimizing the rules initially focuses solely on battery charge sustenance, it is observed that the proposed approach yielded improvements in both hydrogen consumption and system durability. Notably, the specified initial SOC range is very tolerant, allowing the battery to operate within 60% to 80% SOC. Subsequently, this range is adjusted by the GA algorithm in response to prevailing driving conditions. The GA algorithm determines the new minimum and maximum SOC values through an objective function to minimize SOC variation as much as possible. Throughout the optimization process, it is ensured that the minimum optimized SOC limit never falls below 60% and the maximum optimized

SOC never exceeds 80%.

The results show that the optimized rule-based EMS demonstrated notable improvements in hydrogen savings and reduction of battery SOC variations compared to an FLC benchmark [90]. Compared to a DP benchmark, the DP surpassed the rule-based optimized EMS in achieving minimal SOC variation and lower hydrogen consumption [90]. This outcome aligns with expectations, given that DP is renowned for its capability to yield near-global optimal control strategies.

The researchers in [91] implemented a rule-based strategy optimized using DP, consisting of three modes of operation: idle mode, running mode, and braking mode. In idle mode, the FC's power is not required to propel the vehicle, but it continues to operate to prevent FC aging, as frequent start-stops are one of the main reasons for FC SOH degradation. Additionally, the SOC of the battery is considered to determine the power requested from the FC. The battery is charged while the car operates idle when the SOC drops to nearly 50%. If the vehicle remains idle for more than 300 seconds, it is turned off to prevent hydrogen waste.

In running mode, the car can be propelled by the battery, the FC, or both, depending on the battery's SOC and power demand. The FC is limited to operating in the high-efficiency zone to reduce hydrogen consumption. When the SOC is too high, the strategy prioritizes using battery power, while when it is too low, the FC is requested to charge the battery. Otherwise, the rule-based strategy focuses on maximizing the FC's efficiency. The braking mode allows the battery to regenerate energy if the SOC is below the upper limit. Results show that the SOC trajectory of the improved rule-based EMS is closer to the DP benchmark [91].

Wang et al. [92] compared the performance of a rule-based strategy (tuned using

DP) with an MPC controller in an FC/battery FCEV. They considered the cost of hydrogen and the SOH degradation for the battery and the FC as performance parameters. Surprisingly, the findings show that the rule-based strategy outperformed MPC.

The optimization objective function used in this study differs from what is commonly seen in the literature. As shown in [92], this objective function considers three factors contributing to the FC SOH degradation: the number of start-stops, the FC power fluctuation, and the decay of the platinum electrochemically active surface area (ECSA), which depends on the rate of change of FC power. All the parameters used in the mentioned objective function are quantified as a cost in USD and are shown in table 4.3.

In the mentioned table, c_{H_2} is the hydrogen price based on the American DOE, c_{fc} is the cost associated with the decay of the platinum ECSA, c_{pfc} is the coefficient related to the FC power load variation, c_{fch} is the cost associated with FC degradation under high power load, c_{bat} is the cost of battery degradation, and c_{cyl} is the cost of FC degradation due to start-stop cycles.

Table 4.3: Cost parameters for optimization objective function

Cost factors	**Value ($)**
c_{H_2}	2 (kg^{-1})
c_{fc}	3642.35
c_{pfc}	$1.1493 \cdot 10^{-4} (kW^{-1})$
c_{fch}	$1.8994 \cdot 10^{-4} (s^{-1})$
c_{bat}	3125
c_{cyl}	$2.4421 \cdot 10^{-4}$

Wang et al. [92] explains that the rule-based method performs better because the FC exhibits less power variation than when the vehicle operates with the MPC strategy despite having similar average power, which causes degradation in the FC. It is noted that extending the MPC time horizon (30 seconds is used in the simulations) could enhance its performance. Still, its computational cost would be prohibitively high for real-time implementation.

The rules of an FCEV must be chosen according to its implementation priorities. For example, the ones that allow the car to cover more range must differ from those used to decrease FC SOH degradation. As DP, Pontryagin's minimum principle (PMP) can optimize offline the rules of a rule-based EMS according to its primary goal. For instance, Liu et al. [93] presented a rule-learning method with optimized rules to minimize hydrogen consumption using PMP, where a repeated Incremental Pruning to Produce Error Reduction (RIPPER) algorithm extracts rules from the optimal PMP offline EMS benchmark.

The FC power is the output of the rule-based EMS and is defined based on the cluster of the vehicle speed and acceleration (which highly influence the FC power) and battery SOC [93]. All four terms mentioned are clustered using a k-means algorithm, which is an iterative process for assigning each data sample to groups, where the data points are clustered based on specific similar features.

Tables 4.4 and 4.5 summarize critical characteristics of the rule-based strategies presented in the references of this subsection. Table 4.5 is located at the end of this chapter.

Table 4.4: Rule-based methods characteristics - part 1

Reference	**Controller inputs**	**Controller outputs**	**Number of modes**
[80]	SOC; Vehicle speed; Vehicle power demand	FC power	4
[81]	SOC; Vehicle power demand	FC power (Assume 7 different values)	
[83]	SOC; Vehicle power demand	FC power (Assume 5 different values)	
[85]	SOC; Vehicle power demand; FC previous power	FC power variation	6
[86]	SOC; Vehicle power demand	FC power	6
[89]	SOC; Vehicle power demand	FC power	
[90]	SOC; Vehicle power demand; FC efficiency; FC power dynamic limits	FC power	6
[91]	SOC; Vehicle power demand	FC power	3
[92]	SOC	FC power	2
[93]	SOC; Vehicle speed; Vehicle acceleration	FC power	

4.2 Dynamic programming-based Energy Management Strategies

DP is a mathematical method developed by Richard Bellman in the 1950s [94], used to find the optimal solution for a problem by breaking it into subproblems and solving it in the backward direction (from the last state to the beginning).

It is proved that DP is a powerful tool for optimizing control strategies in electrified vehicles. DP has been used to find a near-global optimal sequence of control decisions. The results can be used as a benchmark (to analyze whether another control strategy is the best possible) or to optimize real-time methods. Unfortunately, there are some challenges when implementing DP, as is its computational cost.

Researchers have been making efforts to overcome it with various innovative approaches. Kim et al. [95] introduced a co-optimization method that formulates the DP problem using one discrete variable and one continuous variable to define the power split. This approach significantly reduces the computational cost associated with DP. However, despite these advancements, a widely accepted solution still needs to be discovered.

The publication [96] proposes a DP code to optimize hybrid vehicles and a broad spectrum of alternative systems. The authors go through essential DP-related formulas and concepts, such as state, control, and input variables, providing a lucid elucidation of the underlying principles and further clarifying their developed code's operational logic. Besides, they provide two illustrative examples to explain the DP logic: the first, an elementary demonstration related to the reproduction of fishes but valuable to understanding the fundamentals of the DP code, and the second, a

depiction of a parallel HEV featuring a cost function geared toward fuel consumption minimization.

To allow the reproducibility of their methods, the authors provide all pertinent codes utilized in their study [96]. This work has emerged as a resource for numerous researchers aiming to develop DP algorithms for electrified vehicle applications for the most diverse optimization objectives. Notably, the applicability of this methodology transcends conventional boundaries, being used to optimize powertrains that use alternative energy sources, such as FCs. For instance, it can be used to develop other DP codes to minimize the SOH degradation of FCs and batteries and reduce equivalent hydrogen energy consumption in FCEVs.

The DP methodology operates based on the fundamentals of evaluating all feasible control and state variable combinations at each discrete time step. Authors in [36] employed DP to optimize energy efficiency in a long-haul heavy-duty truck with an FC/battery powertrain. Specifically, they utilized the power change of the FC as a control variable and the FC's power output and the battery's SOC as the state variables. Different from what is employed in hybrid vehicles with engines and EM, when applied to FCEVs, DP usually involves at least three variables in total, considering both control and state variables.

An essential parameter to consider during the application of DP is the discretization step. In the study shown in [36], a discretization step of 5% of the maximum power output of the FCS was used for the control variable to find a good balance between precision and computational grid size (which directly impacts the computational cost). It was observed that increasing the discretization step beyond 5% led to

a marginal degradation in predicted hydrogen economy performance accuracy. Conversely, decreasing the discretization step extensively increased computational costs, improving the hydrogen economy just a little [36]. The cost function that must be minimized inside the DP algorithm includes hydrogen consumption and the number of start-stops of the FC, as it is one of the significant degradation generator factors.

In [97], Researchers employed a DP code to optimize the power split between the PEMFC and the battery aiming while guaranteeing the vehicle's dynamic performance. It that work, the goal was to reduce the operational cost of an FCB operating in the drive cycle China Typical City Bus Cycle (CTCBC). In the process, a cost function was used with several variables, including the hydrogen cost consumed by FC, the electricity cost for charging the battery, and an associated penalty cost variable, which deviates from zero when the SOC constraints are violated.

Moreover, reference [97] documents an interesting finding related to comparing the power split method, implemented through DP, against various strategies for Charge-depleting-Charge-sustaining (CDCS) methods, each utilizing distinct sustaining SOC levels. The investigation demonstrated that employing the power split method proposed results in lower costs, offering a reason for the limited adoption of CDCS in FCEVs with an FC/battery topology.

Besides conventional FCEVs, FCs have also been extensively studied for applications in trains. In reference [98], the authors employed DP to find optimal control trajectories for a train with an FC/battery topology (similar to those used in FCEVs) in three different drive cycles and different weather conditions (summer and winter). Even with a powertrain similar to FCEVs, it is essential to highlight the main differences in the operational conditions, like the very distinct driving cycle profiles.

Notably, train applications operate under conditions very different from typical road traffic and are characterized by reduced frequency of accelerations and decelerations.

Due to the computationally intensive nature of DP, the computational load increases exponentially with the number of states and control variables. In the literature, when employing DP to devise offline control strategies for hybrid vehicles, it is often observed that only the battery SOC is utilized as a state variable. However, for FCEVs with a FC/battery configuration, at least two state variables are usually used due to the power dynamic constraints associated with FCs, which increase the computational load when applying DP for FCEV optimization. Therefore, in the study [98], the battery SOC and the FC power output of the previous time step are used as state variables, and the variation of the FC power is used as the control variable.

A minimum FC power of 10% of the maximum FC power is used as a constraint, which is not so commonly seen when DP is used in the optimization of FCEVs. It is mentioned that this value is used to avoid the shutdown of the FC. Besides, it is interesting to note that 2.5% of the maximum FC power is used as FC power dynamic limits, much lower than those used for conventional FCEVs. It is understandable, as trains do not face constant and unexpected accelerations and decelerations. Furthermore, regarding the cost functions employed, the parameters considered are hydrogen consumption, a penalty associated with FC aging due to rapid power changing, and a term related to the final SOC state. Interestingly, in the results presented in [98], the battery SOC remains relatively constant in both summer and winter along all three drive cycles.

In another study proposed in [99], researchers present a DP method designed to

optimize gear selection and subsequently optimize both gear selection and torque. This method addresses several challenges associated with DP, including interpolation leakage, dimension disaster, standardization issues, and the Markov problem. Furthermore, it demonstrates versatility by applying to EVs and HEVs, with potential adaptability to FCEVs, as explored in a subsequent publication [22].

In the research presented in [22], the adapted DP method presented in [99] was used to optimize the control strategy of a FC/battery FCEV. Two ways to develop the DP strategy are proposed: one with two state variables, called control strategy 1 (battery SOC and FC power change rate), and another with three state variables (the former ones and the FC state), which is called control strategy 2. In this case, the FC state can be represented by one or zero (when the FC is on and off, respectively).

Some uncommon approaches, including the FC temperature, can also be found in the literature. For example, the study proposed in [37] analyzes the effects of the FC stack aging and temperature on the optimal energy management of an FCEV equipped with an FC/battery topology. In this investigation, a DP code is employed to assess the equivalent hydrogen consumption of the vehicle. Specifically, the DP method was developed using a distinctive approach, utilizing two control variables, the FC current and the cooling fan duty cycle (which regulates the FC stack temperature), alongside three state variables, including the battery SOC, the FC power, and the FC temperature.

Notably, in [37], the analysis does not span the entire lifespan of the FC stack but instead considers two levels of FC SOH, categorized as "new" and "aged." Additionally, the DP cost function relies solely on the equivalent hydrogen consumption. The author discusses that more comprehensive results could be achieved by integrating

a cost function encompassing FC stack and battery SOH degradation. Furthermore, the power limit constraints of the PEMFC are defined in this paper as a 10% rise and a 30% fall. The findings of this research reveal that the temperature dimension inclusion can improve fuel economy.

The literature also found some insightful investigations applying DP to lower-level control of FCEVs. In the study conducted in [63], a DP code was used to find the global optimal control strategy for the radiator fan and coolant valve (components of the FC system accessories), aiming to mitigate hydrogen consumption. This comprehensive analysis was made in various ambient temperatures and driving mission lengths.

Moreover, comparative studies were performed in [63] against a baseline strategy. The findings reveal interesting findings. Specifically, it was observed that under mild and high ambient temperatures, longer driving missions achieve a hydrogen-saving potential closer to the optimal DP benchmark. Conversely, the hydrogen-saving potential was higher in colder ambient conditions for medium-length driving missions.

About the variables selected for implementing DP to the problem, the control variables selected are the ratio of stack gross power and FC system request power, the operational state of the radiator fan (limited to on or off modes), and the coolant mass flow regulated by the coolant pump. Meanwhile, the state variables are the FC stack and liquid coolant temperatures [63].

Besides the applications mentioned previously, DP has also found applications in research about the sizing of FCEV powertrains. Even though not the focus of this review, it will be mentioned here due to one interesting finding.

A study was conducted [100] to determine the optimal sizing for an FC and battery

in an FCB using DP, for which an objective function considering hydrogen consumption and FC aging is used. Eight different combinations of FC and battery sizes were investigated, and in two of the three drive cycles analyzed, the best option is very similar to the sizes used in the Opel Vivaro (An FC of 40 kW and a battery of 11 kWh).

It is clear that DP is a handy tool, but it is not so simple to develop from scratch. To overcome this issue, users can use an open-source MATLAB toolbox called DynaProg [101]. DynaProg promises a relatively low computational cost compared to other DP approaches available. This is a highlight of DynaProg, since computational cost is one of the main issues when researchers use DP.

To facilitate the application of DynaProg for electrified powertrains, an example of using it for a P2 hybrid vehicle is shown in [101], which can be adapted for FCEVs and then used to find the optimal control strategies for different situations.

4.3 Other EMSs available in the literature

Besides the Rule-based and DP methods, MPC and Reinforcement Learning are two other control strategy methods commonly studied in current literature.

MPC is a methodology that uses a system model to predict future outputs over a limited time horizon [102].

Among the examples of MPC implementation for FCEVs, Haubensak et al. [103] proposed a double-layer hierarchical MPC to enhance the performance of a fuel cell bus. The MPC planning layer considers the fuel cell's optimal power trajectory and temperature. Meanwhile, the secondary layer focuses on optimizing the pressure and stoichiometry. In the proposed method, the control signals are sent from both layers

simultaneously to the vehicle plant, with the secondary layer receiving a reference signal from the planning layer as input. The authors propose implementing SOH degradation in future work.

In other intriguing studies on MPC for FCEVs, researchers in [54] implemented a fuzzy control EMS in an FCEV characterized by a fuel cell/battery, introducing a novel approach: a charge-sustaining multi-objective model-predictive-based fuzzy control system.

Recently, the application of Reinforcement Learning for FCEVs has also grown. Reinforcement learning (RL) problems involve mapping situations to actions so that a reward signal can be maximized. As in other machine learning techniques, it doesn't tell the learner what actions to take, but instead, it discovers the actions yielding the most reward by trying them out [104].

Many studies have used RL successfully to improve the operation not only of HEVs, such as in [105], but also in FCEVs.

As documented in [106], researchers employed a Deep Q-Network (DQN) algorithm to optimize an FCEV bus featuring a fuel cell/battery configuration. The primary objectives of this optimization were the simultaneous minimization of hydrogen consumption and system degradation.

The cost function utilized encompasses several vital components, namely, the acquisition cost associated with the FC (along with its DC/DC converter) and the battery, the hydrogen cost, and the equivalent hydrogen cost of the electricity given by the battery, which depends on the variation in its SOC. Moreover, the results section claims significant operational cost improvements for the FCS and battery, although with a slightly elevated fuel consumption rate.

Another study conducted by Jia et al. [107] employed a Twin Delayed Deep Deterministic Policy Gradient (TD3) algorithm to propose a health-aware EMS for an FCB. This research focused on balancing air-conditioning control and battery SOH degradation to optimize the system cost while maintaining cabin comfort. The authors mention that the TD3 algorithm, an RL method, can mitigate the overestimation issue of another reinforcement learning method: The Deep Deterministic Policy Gradient (DDPG). Moreover, the TD3 algorithm demonstrated remarkably improved training efficiency compared to the so-called DDPG-comfort strategy [107].

To conclude, some other interesting EMS not widely explored can also be found, such as the implementation of Wavelet-transform-based EMS, which is used to mitigate abrupt fluctuations in the FC power, as presented in [47]. Moreover, applications of NNs combined with DP [108] or GA [109] and min-max game theory [71] can also be found in the literature.

Table 4.5: Rule-based methods characteristics - part 2

Reference	**Modes**	**Optimization method**	**Optimization criteria**
[80]	Battery solely; FC solely; Battery and FC together; Regenerative braking	GA	Hydrogen consumption; Battery SOH degradation; FC SOH degradation
[81]	Membership function	GA	Hydrogen consumption
[83]	Membership function	GA	Hydrogen consumption; FC SOH degradation
[85]	Start-mode, FC solely; Battery charging; Battery and FC together; Regenerative braking; Parking	No-optimized	
[86]	Battery and FC together; Battery Solely; FC solely (low power); FC solely (High power and low SOC); FC solely (High power and high SOC); Regenerative braking	Optimized using polynomials to reproduce experimental curves	
[89]	Membership function	No-optimized	
[90]		GA	Hydrogen consumption; FC SOH degradation
[91]	Idle mode; Running mode (can be battery solely, FC solely, or both); Regenerative braking	DP	Hydrogen consumption
[92]	Battery solely; Battery and FC together	DP	Hydrogen consumption; Battery SOH degradation; FC SOH degradation
[93]	Membership function	PMP	Hydrogen consumption

Chapter 5

State-of-Health Aware Energy Management System for the Fuel Cell Electric Van

5.1 Rule-based Energy Management system

Rule-based EMSs have been extensively utilized due to their real-time implementability, relatively low complexity, and low computational demands. Due to these advantages, they were initially adopted for controlling the modelled FCEV.

5.1.1 Rule-based Energy Management system development

The chosen approach is based on operational modes. A total of five modes are employed. The EMS subsystems determine the operational mode and manage the power distribution between the battery and the FC. These subsystems are integrated within

the controller subsystem of the main vehicle model. Figs. 5.1 and 5.2 illustrate the blocks that define the operational modes.

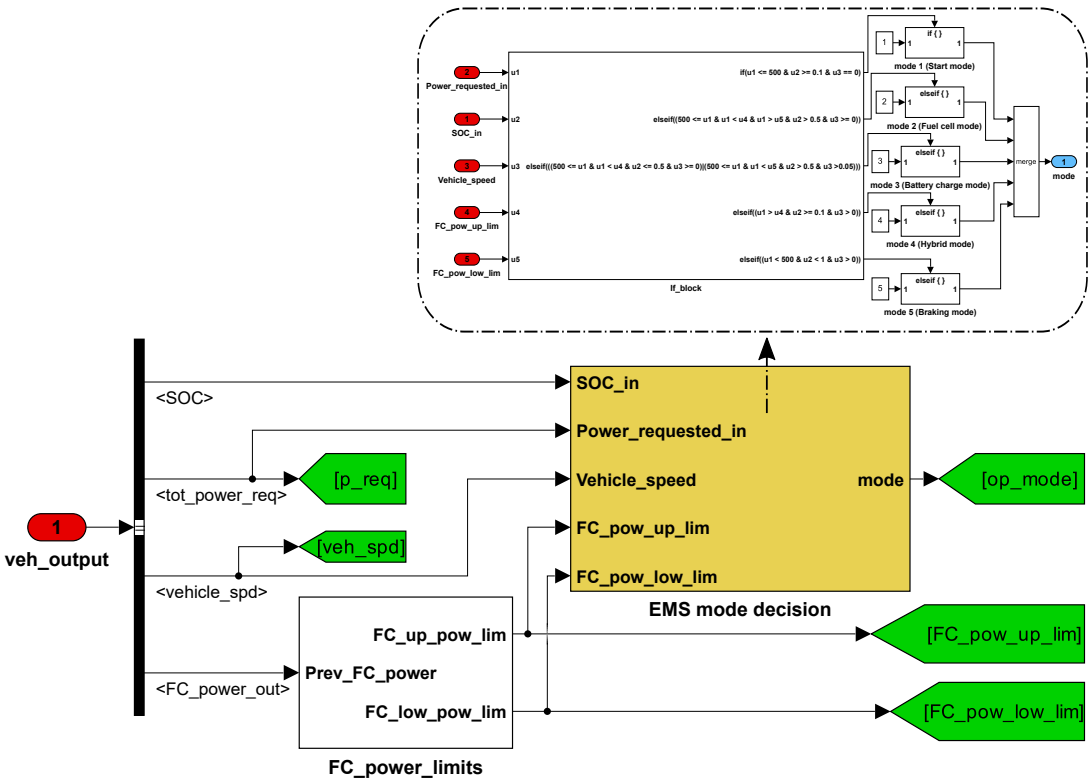

Figure 5.1: EMS operation mode subsystem inside the controller - layer 1

In fig. 5.2, an 'if' block activates one of the five corresponding action blocks at each time step. Consequently, a number from 1 to 5 is transmitted to the merge block at each time step, which outputs the most recently received number. Table 5.1 summarizes the conditions for activating each mode of operation. In fig. 5.2, u_1, u_2, u_3, u_4, and u_5 represent the vehicle power demand (combined demand from the EM and electrical accessories), the battery SOC, the vehicle speed, the upper power limit of the FC, and the lower power limit, respectively.

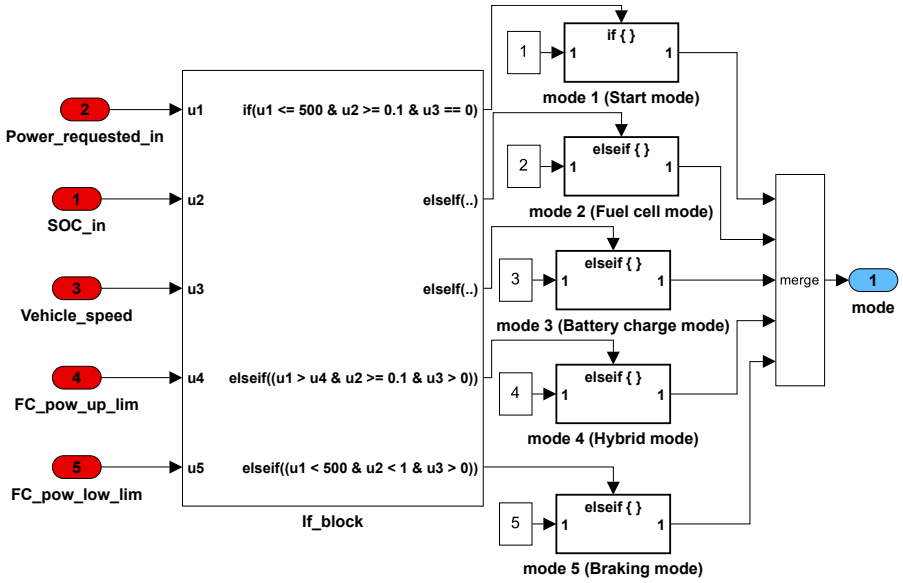

Figure 5.2: EMS operation mode subsystem inside the controller - layer 2

The Start Mode is activated when the vehicle begins operation, typically at the start of the drive cycle. When the vehicle demands a power level that the FC can supply without exceeding its power dynamic limits and maximum power limits, the FC or the battery charge mode is selected. This decision depends on the battery's SOC. The battery charging mode is used if the SOC is below the predetermined charge-sustaining level of 50%. Otherwise, the FC mode is selected. Additionally, if the vehicle's power demand suddenly falls below the lower power limit of the FC, the battery charge mode is employed. Consequently, the power difference between the FC's lower power limit and the vehicle's power demand is directed to the battery for charging.

The Hybrid Mode is utilized when the FC alone cannot meet the vehicle's total power demand due to its dynamic power limits or maximum power limit. In these

situations, the battery supplies the remaining required power. Furthermore, the Braking Mode is employed when the vehicle needs to brake, identified by a power demand lower than the power demand of the electrical accessories.

Table 5.1: Rule-based EMS modes of operation conditions

Mode of Operation	**Condition**	**Mode Index**
Start Mode	If ($P_{\text{req}} \leq 500$) & (SOC ≥ 0.1) & ($\text{veh}_{\text{spd}} = 0$)	1
Fuel Cell Mode	else if ($P_{\text{req}} \geq 500$) & ($FC_{\text{pow\_low\_lim}} < P_{\text{req}} < FC_{\text{pow\_up\_lim}}$) & (SOC > 0.5) & ($\text{veh}_{\text{spd}} \geq 0$)	2
Battery Charge Mode	else if (($FC_{\text{pow\_up\_lim}} > P_{\text{req}} \geq 500$) & (SOC ≤ 0.5) & ($\text{veh}_{\text{spd}} \geq 0$)) | ($FC_{\text{pow\_low\_lim}} > P_{\text{req}} \geq 500$) & (SOC > 0.5) & ($\text{veh}_{\text{spd}} > 0$)	3
Hybrid Mode	else if ($P_{\text{req}} > FC_{\text{pow\_up\_lim}}$) & (SOC ≥ 0.1) & ($\text{veh}_{\text{spd}} > 0$)	4
Braking Mode	else if ($P_{\text{req}} < 500$) & (SOC < 1) & ($\text{veh}_{\text{spd}} > 0$)	5

Once the mode of operation is chosen, it determines the amount of power the FC and battery must generate. Fig. 5.3 illustrates the subsystems employed for this purpose.

The power generated by the FC at a specific time step is calculated using the subsystem depicted in fig. 5.4. Similar to the subsystem used to define the mode of operation, an 'if' block activates one of five corresponding 'if-action' blocks. Unlike

the mode-defining subsystem, which requires multiple inputs and input combinations, this subsystem uses a single input for the 'if' block, which can take one of five values. Each value is responsible for activating one of the 'if-action' blocks.

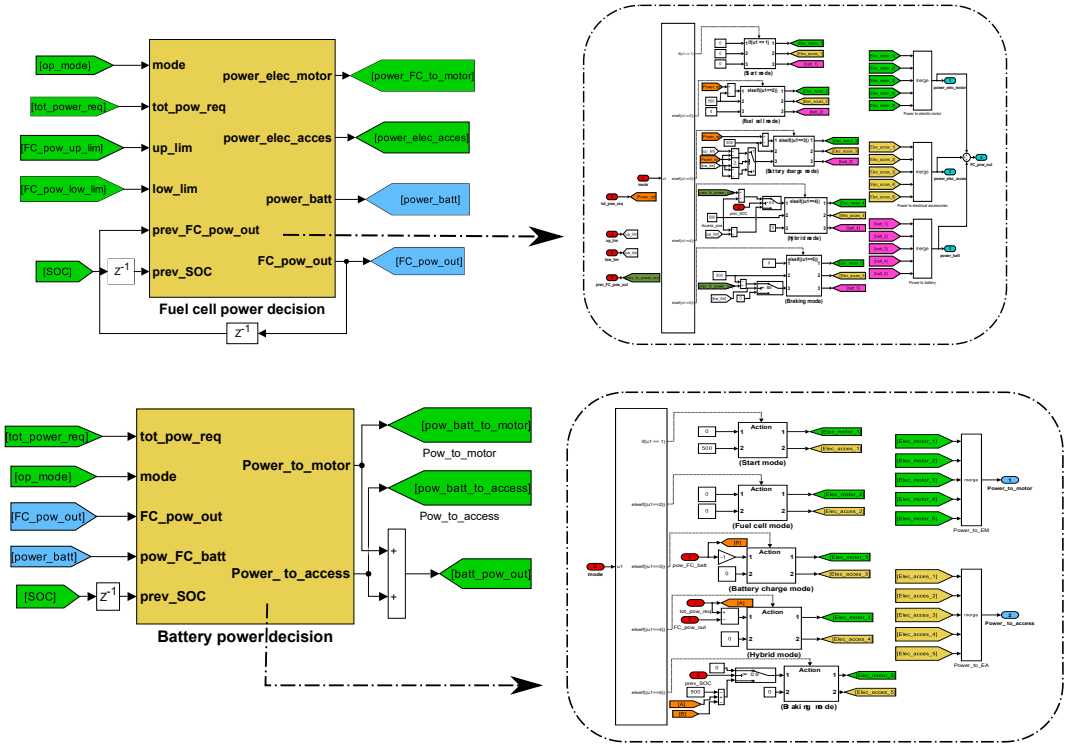

Figure 5.3: Fuel cell and battery power calculator subsystems - layer 1

In the main vehicle model developed, the FC can provide power to the electric accessories, motor, and battery, so each if-action block outputs three values when activated, one for each destination mentioned. If, in one specific situation, the FC must not send power for one of those three, it outputs zero. In the start mode, for example, the car is idling, and the EM and battery don't require any power, while the battery must feed the accessories, so three zeros are outputted by the subsystem

of fig. 5.4.

The FC can supply power to the electric accessories, EM, and battery in the main vehicle model developed. Consequently, when activated, each 'if-action' block outputs three values, one for each of the destinations above. If, in a specific situation, the FC should not supply power to one or more of these destinations, it outputs zero for those channels. For instance, in the Start Mode, where the car is idling, neither the EM nor the battery requires power, while the battery needs to power the accessories. Therefore, the subsystem depicted in fig. 5.4 outputs three zeros.

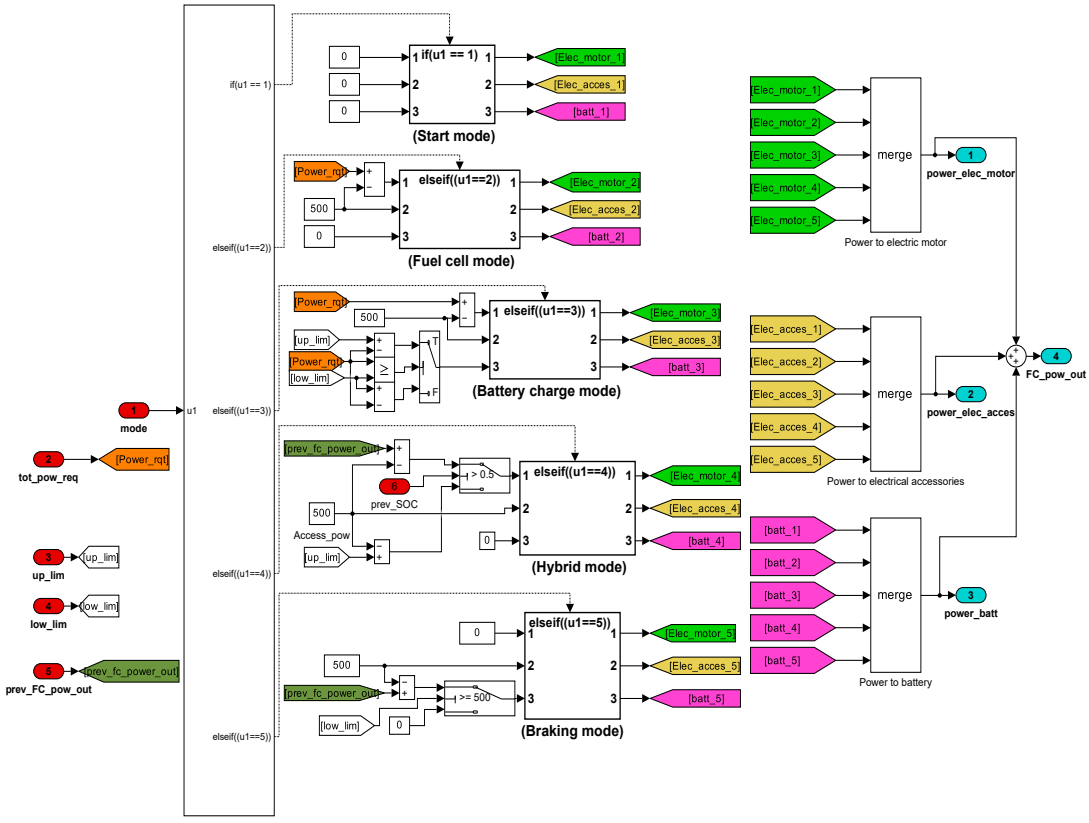

Figure 5.4: Fuel cell power calculator subsystem - layer 2

From Mode 2 to Mode 5, the FC powers the electrical accessories. As previously discussed, this approach mitigates the aging of FCs, as frequent start-stop cycles accelerate the degradation of the FC. Therefore, once the FC begins its operation, it remains active until the conclusion of the drive cycle to avoid unnecessary starts and stops.

In mode 3, the FC generates the entire vehicle power demand. The power directed to the battery varies according to eq. 5.1.1. In this equation, P_{up_lim} represents the upper power limit of the FC, P_{low_lim} is the lower power limit, P_{FC_batt} is the power transferred from the FC to the battery, and P_{veh_dmd} is the vehicle power demand. This logic is applied because if the SOC is below the charge-sustaining level, the FC aims to quickly restore the SOC to 50%. Furthermore, when the vehicle power demand suddenly decreases, and the FC output cannot be reduced quickly due to established constraints, the FC will produce the minimum power possible. Simultaneously, any surplus power that the EM and electrical accessories do not require is utilized to charge the battery, ensuring that no energy is wasted.

$$\begin{cases} P_{FC\_batt} = P_{up\_lim} - P_{veh\_dmd}, P_{veh\_dmd} >= P_{up\_lim} \\ P_{FC\_batt} = P_{low\_lim} - P_{veh\_dmd}, P_{veh\_dmd} < P_{up\_lim} \end{cases} \tag{5.1.1}$$

In mode 4, the Hybrid mode, the power generated by the FC depends on the battery's SOC, as outlined in eq. 5.1.2. Here, P_{FC_out} and $P_{prev\_FC\_out}$ represent the total FC power output at the current and previous time steps, respectively. When the SOC is above the charge-sustaining level, the FC power output remains constant (or equal to the previous time step's output, according to the logic shown in fig. 5.4. This stability in power output helps prevent FC aging, which is one of the main causes of

degradation, as discussed in previous chapters. Moreover, when the SOC falls below the charge-sustaining level, the FC delivers the maximum power possible to avoid excessive battery discharge.

$$\begin{cases} P_{FC\_out} = P_{prev\_FC\_out}, SOC > 0.5 \\ P_{FC\_out} = P_{up\_lim}, SOC <= 0.5 \end{cases} \tag{5.1.2}$$

In Mode 5, the Braking Mode, the EMS attempts to regulate the FC to generate only the power demand of the electrical accessories. However, if the FC is producing a high level of power and the vehicle suddenly needs to brake, the FC's power output can only be reduced slowly due to the constraints imposed by its lower power limit. Under these circumstances, the FC will generate the minimum power possible, and any excess power not required by the electrical accessories will be used to charge the battery.

5.1.2 Rule-based Energy Management system discussion and results

Before running the main vehicle model in a loop to analyze the degradation of the FC and battery over time, this model was run once in each drive cycle using different time step values.

Estimating the lifespan of the FCEV is computationally intensive, requiring the model to be run thousands of times to simulate the EOL conditions for the FC or battery. To manage this, increasing the simulation's time step can significantly reduce computational costs. However, this also impacts the accuracy of the simulations. A careful balance between accuracy and computational efficiency is necessary, achieved

using the energy balance method described in a previous chapter. To evaluate this, four-time step values ($1s$, $0.1s$, $0.01s$, $0.001s$) were applied to determine the energy balance in the main vehicle model across different drive cycles, with the findings detailed in table 5.2.

Table 5.2: Energy balance error percentage for multiple time steps

Time step	**WLTP**	**HWFET**	**UDDS**	**FTP-75**
$1s$	990%	279.5%	3712%	1823%
$0.1s$	3.487%	0.88%	6.862%	6.912%
$0.01s$	0.4523%	0.1426%	0.8785%	0.8812%
$0.001s$	0.1872%	0.06114%	0.3524%	0.3533%

Table 5.2 illustrates that using time steps of 1 second and 0.1 seconds results in poor accuracy. On the other hand, while providing high accuracy, a time step of 0.001 seconds requires over a week to complete each drive cycle simulation until the EOL for the FC or battery. For instance, a simulation run at 0.001 seconds for the WLTP drive cycle progressed less than 10% after one full day. Consequently, a time step of 0.01 seconds was chosen for the analysis. This allows completing the simulation of each drive cycle within approximately two days while maintaining a satisfactory accuracy level.

Single drive cycle run with rule-based EMS

After executing the main vehicle model across each drive cycle, the following observations were made. The vehicle speed was analyzed to verify the FCEV capability to follow all the specified drive cycles accurately. Figs. 5.5, 5.6, and 5.7 illustrate these

results.

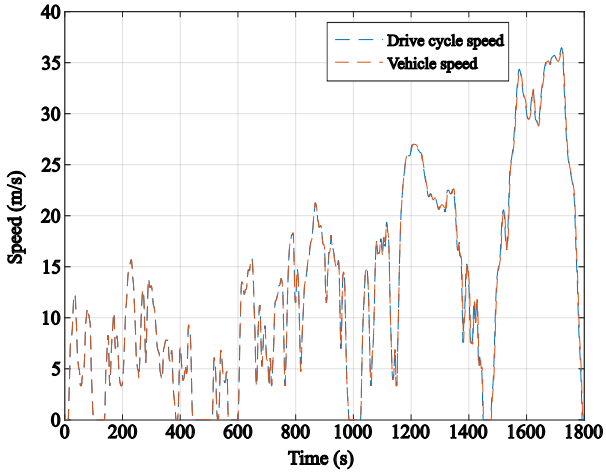

Figure 5.5: Vehicle speed profile in WLTP

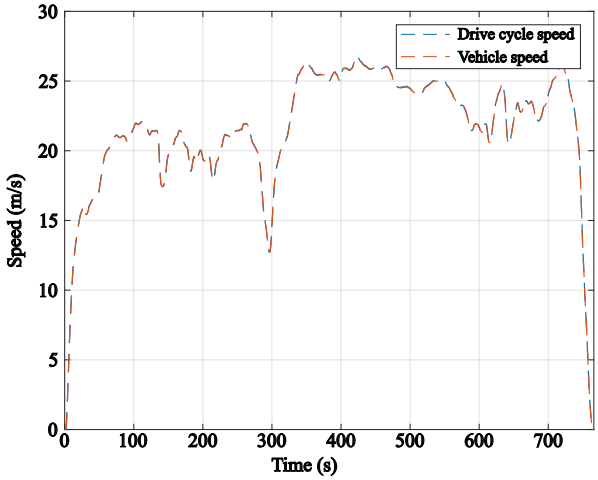

Figure 5.6: Vehicle speed profile in HEFET

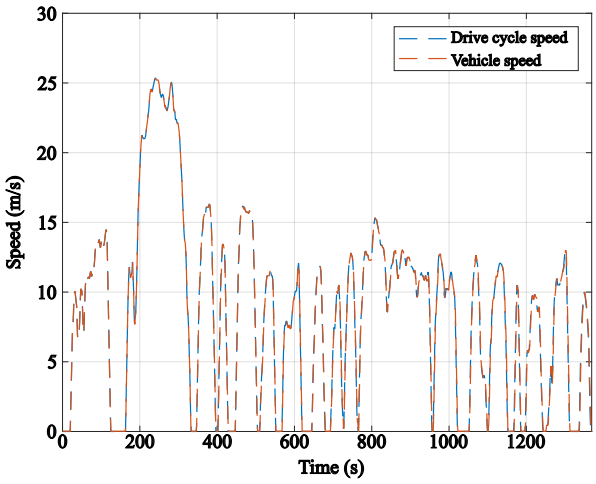

Figure 5.7: Vehicle speed profile in UDDS

The figs. 5.8, 5.9, and 5.10 display the results for the power demand alongside the power supplied by both the FC and the battery. In fig. 5.8, it can be noted that between seconds 300 and 400 the battery provides most of the power demand despite this power demand being below the FC's peak power. This is due to the dynamic power limits applied to preserve the FC and prevent reactant starvation. Correspondingly, in the same time frame shown fig. 5.5, it is observed that although the average vehicle speed is low, there are frequent and sharp accelerations and decelerations. This pattern explains why the battery is required to supply significant amounts of power.

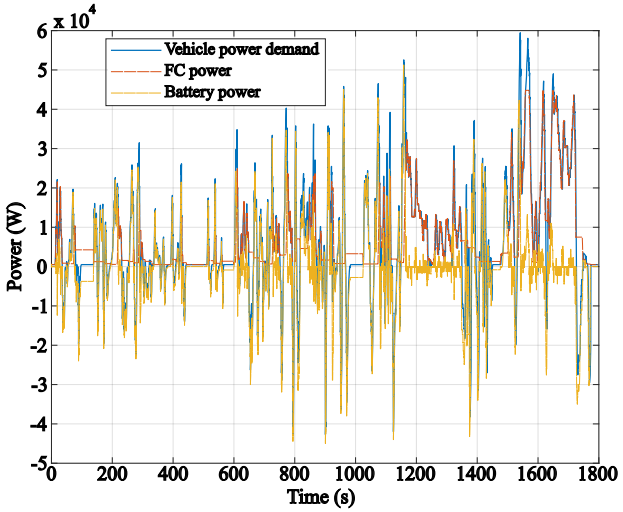

Figure 5.8: Power profiles in WLTP

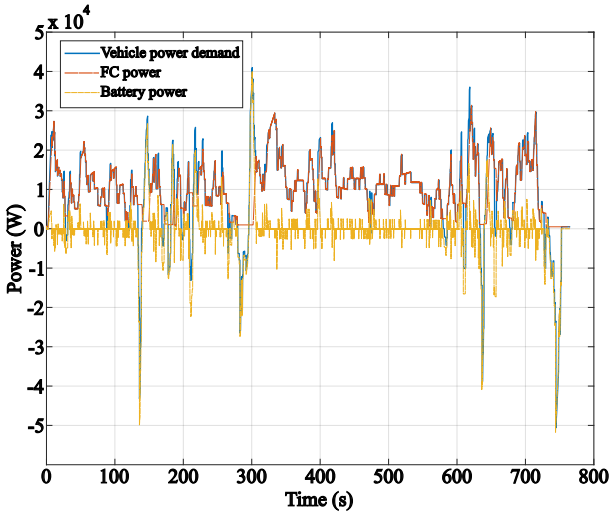

Figure 5.9: Power profiles in HWFET

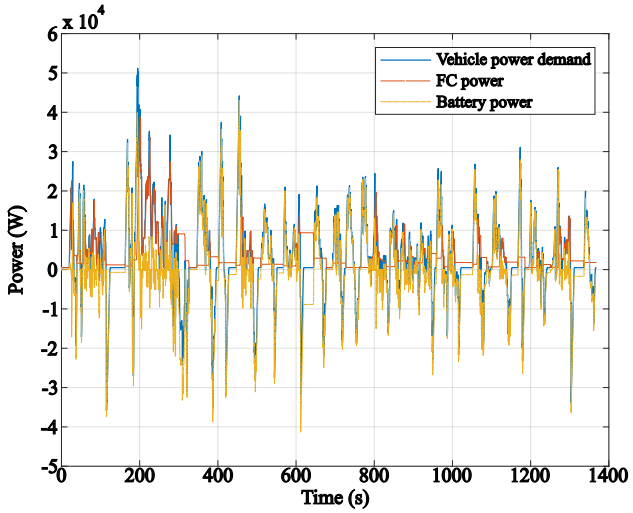

Figure 5.10: Power profiles in UDDS

To ensure the charge-sustaining operation, the strategy must maintain the battery's SOC around 50%. Maintaining this value in the proposed powertrain is challenging, primarily due to the dynamic limitations of the FC and its relatively small size.

When the vehicle experiences sudden changes in power demand, and the FC may not always be able to meet the entire power requirement, the SOC must drop as the battery discharges. Figs. 5.11, 5.12, 5.13 illustrate the SOC trajectories for the analyzed drive cycles. Notably, in fig. 5.11, there is a significant drop in SOC between seconds 1400 and 1600, which coincides with a high average speed and increased power demand, as shown in fig. 5.5.

Furthermore, fig. 5.8 shows that the power demand often exceeds 45 kW in the mentioned time region, surpassing the FC's peak power. Towards the end of the drive cycle, the SOC rises again as the vehicle decelerates from 35 m/s to 0 m/s. The SOC stabilizes near the end of the cycle due to the activation of friction brakes, which

dissipate some braking energy to prevent the SOC from rising above 51%.

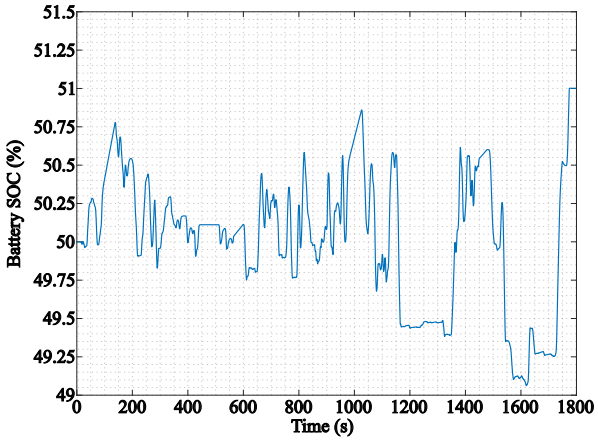

Figure 5.11: Battery SOC in WLTP drive cycle

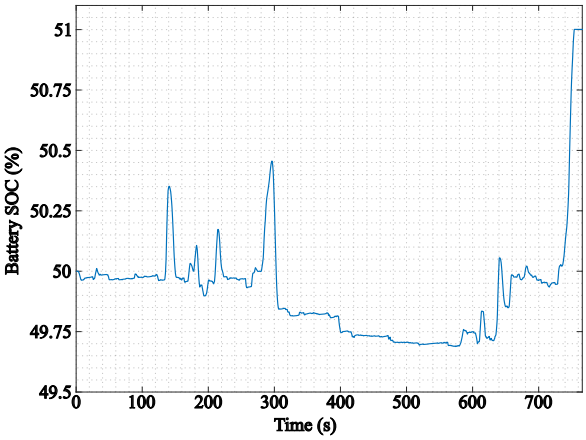

Figure 5.12: Battery SOC in HWFET drive cycle

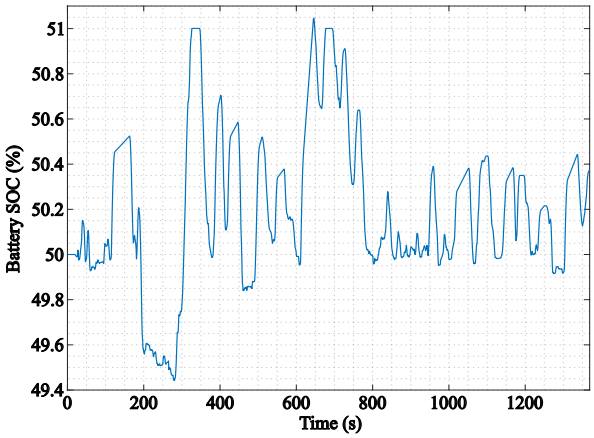

Figure 5.13: Battery SOC in UDDS drive cycle

Figs. 5.14, 5.15, and 5.16 illustrate the operation modes employed during different drive cycles. When operating in the WLTP and UDDS drive cycles, as the vehicle faces more frequent braking mode use than in the HWFET cycle, it results in more need for the braking mode. Additionally, the smoother accelerations in HWFET reduce the frequency at which the battery needs to be used, unlike in the WLTP and UDDS cycles, where more frequent and abrupt accelerations occur.

Figs. 5.17, 5.18, and 5.19 display the variation in the SOH for both the FC and the battery across different drive cycles at their BOL. At the start of each drive cycle, a vertical line indicates a sudden aging event, which consistently occurs due to the initiation or shutdown of the FC operation.

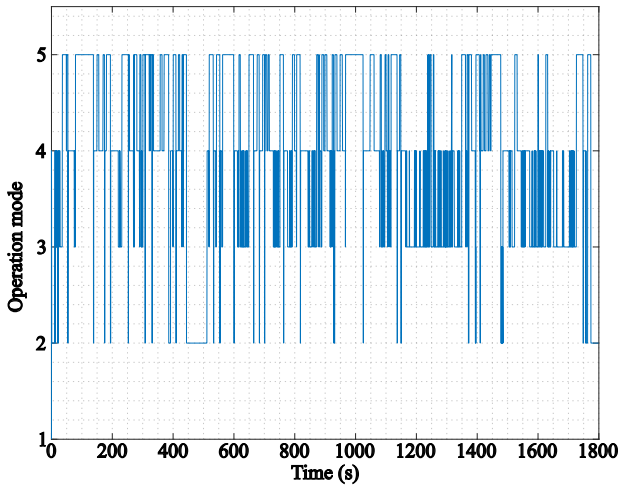

Figure 5.14: Operation modes used during the WLTP drive cycle

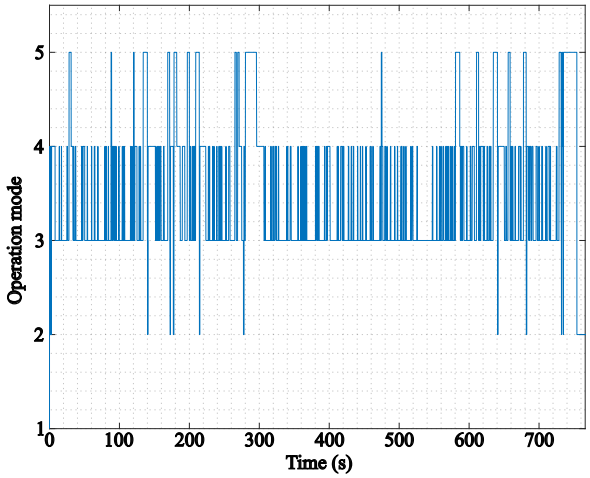

Figure 5.15: Operation modes used during the HWFET drive cycle

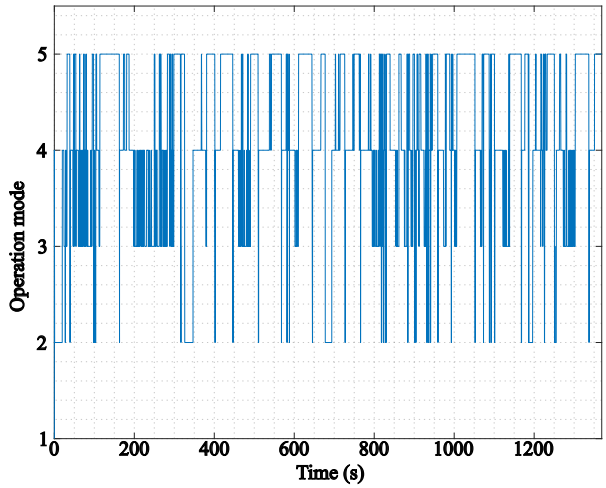

Figure 5.16: Operation modes used during the UDDS drive cycle

Additionally, it is observed that the battery experiences more aging after a single run of the WLTP and UDDS cycles compared to the HWFET cycle. It happens not only due to the longer duration of these cycles but primarily because the battery is subjected to higher demands in the WLTP and UDDS cycles. The vehicle can operate for a long time with the applied control strategy, as the aging of the components is very small after one drive cycle.

Finally, the hydrogen consumed to complete the driving mission is displayed in figs. 5.20, 5.21, and 5.22.

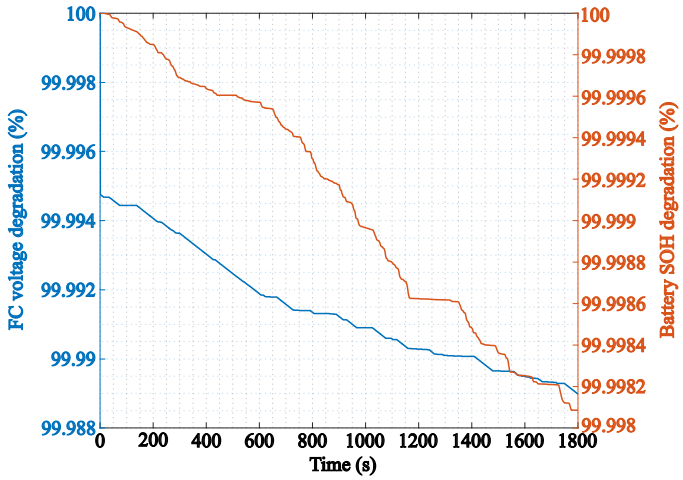

Figure 5.17: Degradation of FC and battery after one run of WLTP

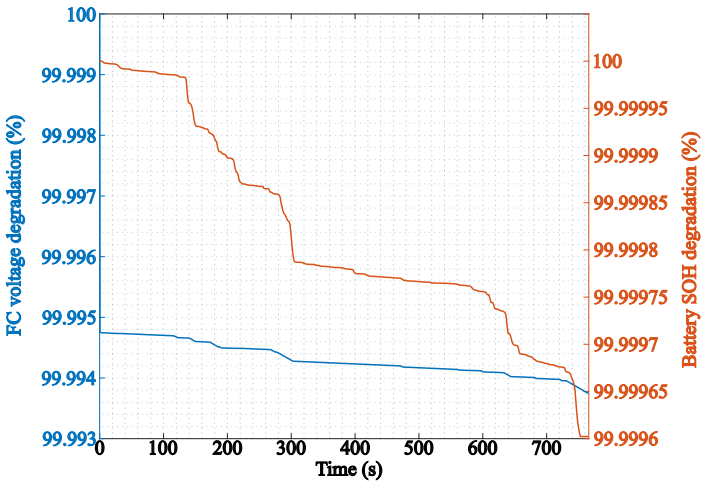

Figure 5.18: Degradation of FC and battery after one run of HWFET

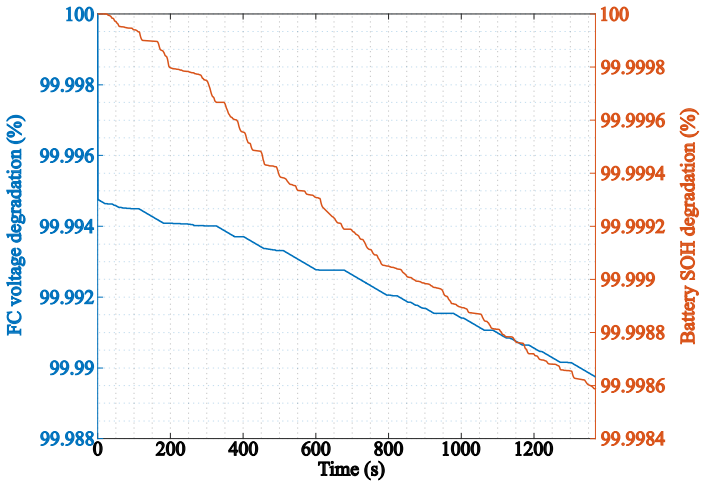

Figure 5.19: Degradation of FC and battery after one run of UDDS

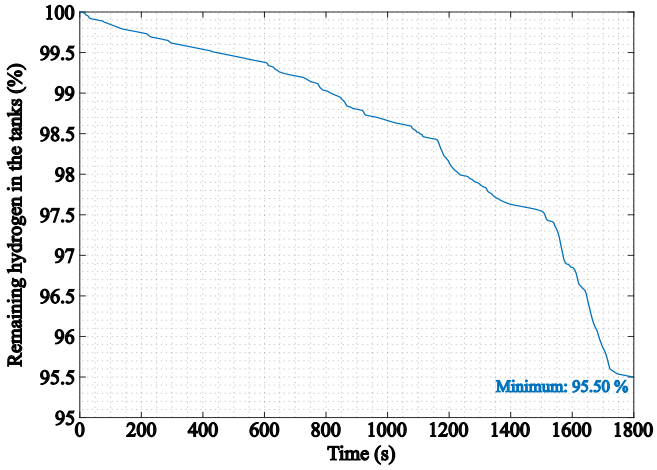

Figure 5.20: Hydrogen consumption in WLTP

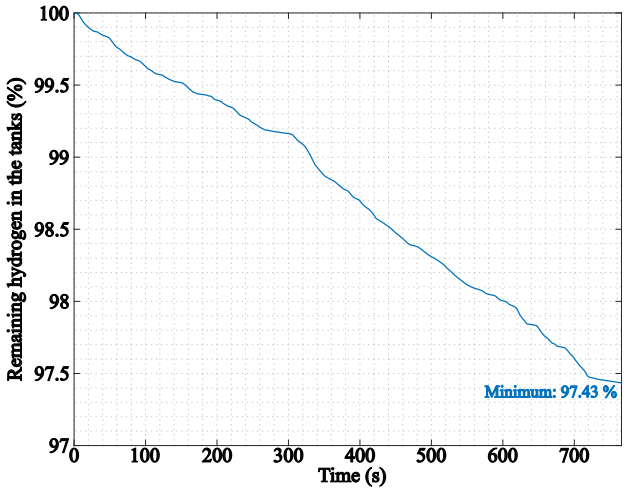

Figure 5.21: Hydrogen consumption in HWFET

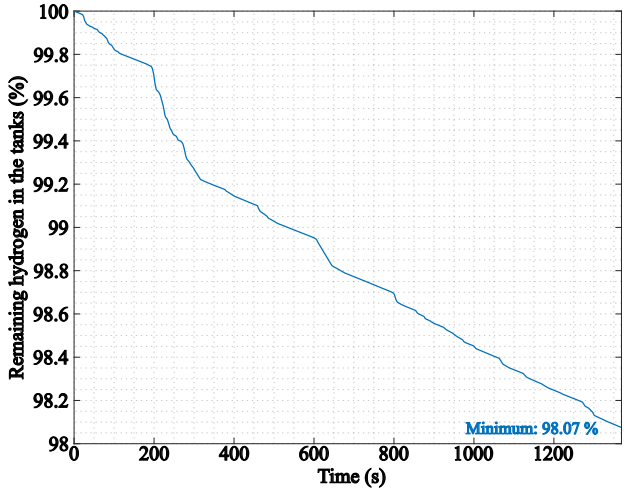

Figure 5.22: Hydrogen consumption in UDDS

Table 5.3 summarizes the range of the modelled FCEV based on consumption. This table shows how a more aggressive drive cycle can sharply harm the car's performance, while highway scenarios are favourable to avoid hydrogen consumption.

Table 5.3: Range of the FCEV for multiple drive cycles in the FC and battery BOL

Drive Cycle	**Distance (km)**	**Range (km)**	**Hydrogen Consumption (l/ 100 km)**
WLTP	23.26	528.17	14.64
HWFET	16.45	674.98	11.45
UDDS	12	641.81	12.044

After analyzing the performance of the main vehicle model through a single run of each drive cycle, starting from the BOL for both the FC and battery, the model was subsequently run in a loop. After each drive cycle's completion, the values of battery SOH degradation, FC SOH degradation, and the final SOC are recorded in this loop. These values are then used as the starting conditions for the next run drive cycle run. Such iterative runs impact the behavior of the FCEV, as the FC's polarization and efficiency curves and the battery's resistance and OCV curves will change over time. This looping process continues until the FC or battery reaches the EOL.

After reaching the EOL of each component, the results were computed. Firstly, to guarantee that after each single run of the main vehicle model in the mentioned loop, the error was still small, these values were saved. From fig. 5.23, it is possible to see that the energy balance values are still very similar to the initial one and even become smaller along the simulations.

The energy balance error is checked each time the driving mission ends within the loop to ensure accuracy throughout the simulations. Fig. 5.23 shows that the energy balance values remained close to their initial levels and decreased slightly as

the simulations progressed.

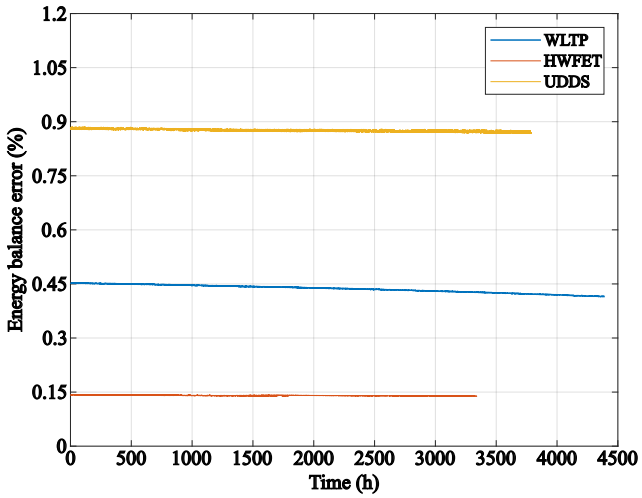

Figure 5.23: Energy balance error after operating in each drive cycle until reach the FC EOL

The SOC at the end of each driving mission is recorded and displayed in fig. 5.24. This measurement is crucial because the vehicle needs to be able to follow the drive cycles while there is hydrogen in the tanks. This will only be possible if the battery can support the FC when the power demand exceeds what the FC can provide.

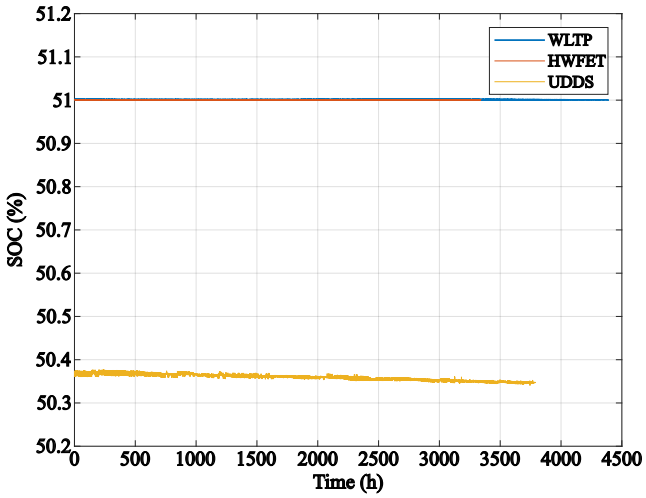

Figure 5.24: SOC at the end of the drive cycle

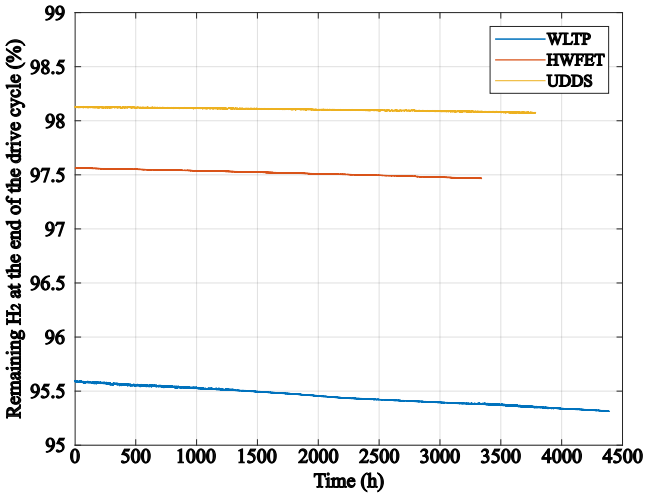

Figure 5.25: Remaining hydrogen after completing the drive cycle

The remaining hydrogen percentage was recorded to estimate how the FCEV range changes as the FC and battery degrade. Fig. 5.25 illustrates the curve of the remaining hydrogen percentage after each drive cycle, which falls slightly along the time. A more pronounced drop is observed in the WLTP drive cycle.

Table 5.4 presents the critical values for the FCEV at the EOL of the FC.

It is observed that although the FC reaches its EOL first in all three drive cycles, the battery experiences more pronounced aging during the WLTP cycle. This is expected, as the battery is utilized more frequently in this drive cycle. Moreover, in the HWFET cycle, the battery retains considerable life, not reaching even half its lifespan after the EOL of the FC.

Table 5.4: Parameters at the EOL of the FC

Drive Cycle	**Hours of Operation**	**Total Distance (km)**	**Number of Cycles**	**Range at the FC EOL (km)**	**Hydrogen Consumption (l/100 km)**
WLTP	4392.5	204,339.1	8785	496.4	15.57
HWFET	3337.1	258,330.8	15704	649.53	11.9
UDDS	3786.91	119,499.28	9958	623.34	12.4

5.2 Implementation of Dynamic Programming

5.2.1 Dynamic Programming code development

A DP code was written to find the FCEV model's optimal control and state trajectories. The DynaProg MATLAB toolbox was used to solve this problem.

In total, three state variables and one control variable are used. The state variables are the battery SOC, the FC power of the previous time step, and the FC voltage. The control variable is the FC power variation. These variables are defined in eq. 5.2.1, where x defines the state variables and u the control variables.

$$x = \begin{bmatrix} SOC \\ P_{FC_{-1}} \\ V_{FC} \end{bmatrix}, u = \begin{bmatrix} \Delta P_{FC} \end{bmatrix} \tag{5.2.1}$$

As discussed previously, the DP problem involves discretization. As shown for the main vehicle model, smaller time steps give more accurate results. In the case of DP, smaller time steps give trajectories closer to the real optimal. On the other hand, the computational capacity is a challenge for DP implementation, so the time step used in DP must be chosen accurately and can not be excessively short. Moreover, this computational cost increases exponentially as the number of states and control variables increases, and four variables (as used here) is a relatively high number when compared to other DP codes used for electrified vehicle applications in the literature. The time step for the DP code using DynaProg here was 0.5 s.

Another critical factor when implementing DP is the number of grids of each variable. The number of grids for the SOC is shown in table 5.5, and the other variables are shown in table 5.6.

Table 5.5: DP SOC grids used

Initial SOC	**Number of grids**	**Lower grid boundary**	**Upper grid boundary**	**Interval**
40%	160	0.37	0.53	0.001
50%	160	0.42	0.58	0.001
60%	160	0.47	0.63	0.001

Table 5.6: Variables number of grids

Variable	**Number of grids**
Previous FC power	500
FC voltage	80
Δ FC power	80

The DP code needs an objective function (or cost function) to find the optimal trajectories. It is used to estimate the stage cost, defined as the cost of going from one state in one time step to another state in the next time step. This value is used to find the sequence of control actions with the lowest final cost. The stage cost is estimated here using the objective function shown in eq. 5.2.2.

The objective function considers the cost in USD of the hydrogen consumed by the FC, the aging cost associated with the FC, and the aging cost associated with the battery. These costs and their respective references are described in table 5.7.

$$L = \int_{t}^{t+0.5} (\dot{c}_{batt} + \dot{c}_{FC} + \dot{c}_{H_2})\, dt \tag{5.2.2}$$

The hydrogen cost, the FC cost, and the battery cost are defined from eq. 5.2.3, 5.2.4, and 5.2.5, where m_{H_2} is the mass of the hydrogen consumed, ΔSOH_{FC} is the change of the FC SOH, and ΔSOH_{batt} is the change in the battery SOH.

Additionally, in eq. 5.2.4 the value $44,884$ represents the maximum FC output power at its BOL, and the number 10 is used to scale the degradation percentage because it is assumed that the FC reaches its EOL after 10% of SOH degradation, as mentioned in a previous chapter.

$$c_{H_2} = \frac{2 \cdot m_{H_2}}{1000} \tag{5.2.3}$$

$$c_{FC} = \frac{\Delta SOH_{FC} \cdot 40 \cdot 44884}{10 \cdot 1000} \tag{5.2.4}$$

$$c_{batt} = \frac{\Delta SOH_{batt} \cdot 125 \cdot 10.8}{0.2} \tag{5.2.5}$$

Table 5.7: Costs used in the DP objective function

Variable	**Cost**	**Unit**	**Reference**
Hydrogen fuel	2	USD/kg	[110]
Fuel cell	40	USD/kW	[111]
Battery	125	USD/kWh	[112]

5.2.2 Offline optimal control of EMS through Dynamic Programming

The DP optimal trajectories in all drive cycles and for different initial SOC levels were found and are shown below.

The purpose of using DP here is to generate state and control action values that will be used as samples for training a NN, which will be discussed in the following subsection. Additionally, the NN aims to maintain the vehicle's SOC at a sustaining level of 50%, similar to the rule-based method based on operation modes. Therefore, the DP code should be executed with initial SOC values set to 50% to find the optimal control trajectories. Other initial SOC values were also considered to enhance

the robustness of the results. This aspect will be further explained in the following subsection.

Firstly, the optimal SOC trajectories for the WLTP drive cycle for the various initial SOC values are demonstrated in fig. 5.26.

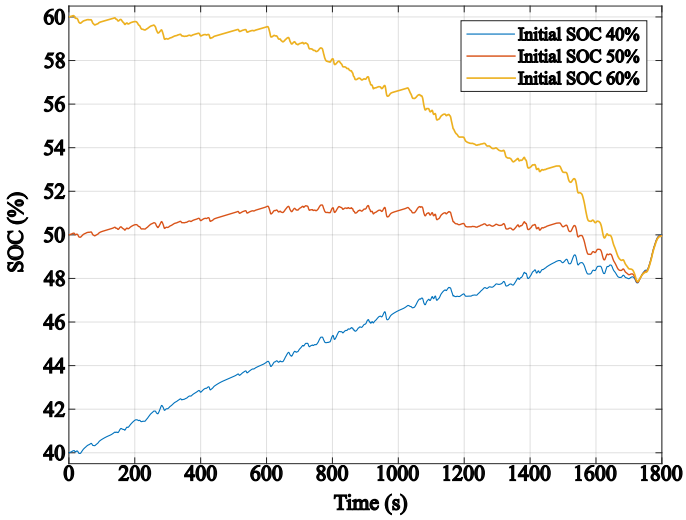

Figure 5.26: WLTP optimal SOC trajectories for 40%, 50%, and 60% initial SOC

Next, the optimal FC voltage trajectories are shown in fig. 5.27 below.

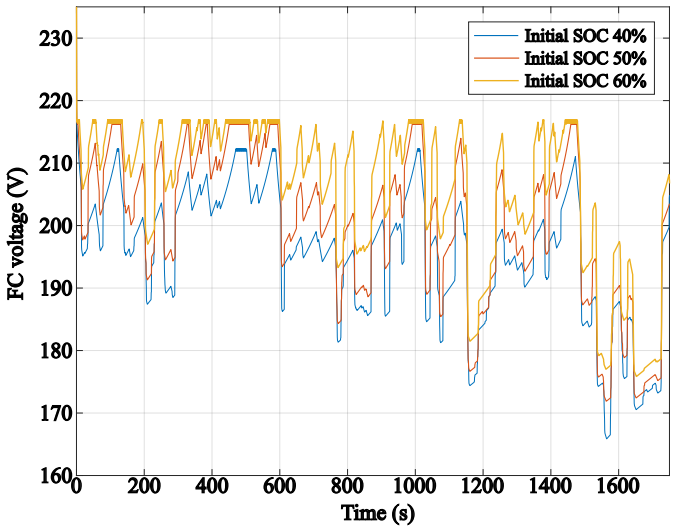

Figure 5.27: WLTP optimal FC voltage trajectories for 40%, 50%, and 60% initial SOC

The FC power trajectories, representing the values of the FC's previous power state variable, are shown in Fig. 5.28.

Compared to the profile shown in fig. 5.8, the FC power now exhibits smoother variations, which helps to reduce SOH degradation. Additionally, unlike what is observed in fig. 5.8, the FC power never reaches 40 kW, which contributes to avoiding aging associated with high-power regions and lower efficiency zones, thereby saving hydrogen.

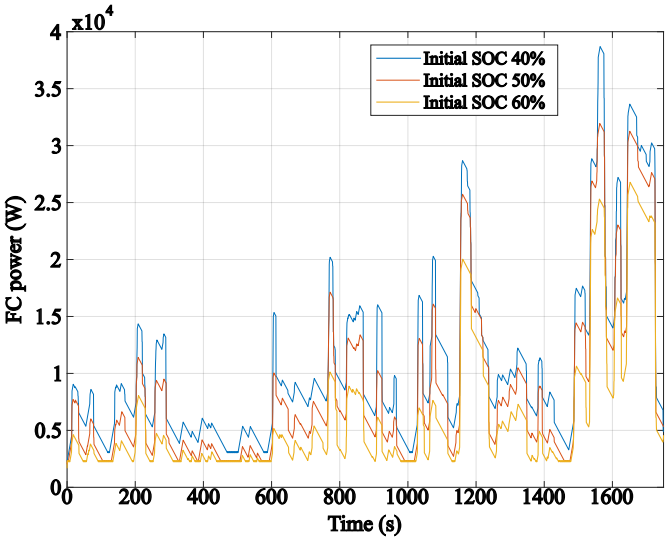

Figure 5.28: WLTP optimal FC power trajectories for 40%, 50%, and 60% initial SOC

Finally, the optimal FC power variation trajectories, representing the optimal DP control actions, are shown in fig. 5.29. The values are reasonable, with FC power changes limited to a 10% increase and a 30% decrease per second, as discussed in a previous chapter. Given that the DP code runs with a time step of 0.5 seconds and the maximum FC power is 44,884 W, these variations are constrained between -6,732 W and 2,244 W. These limits are respected in the DP results.

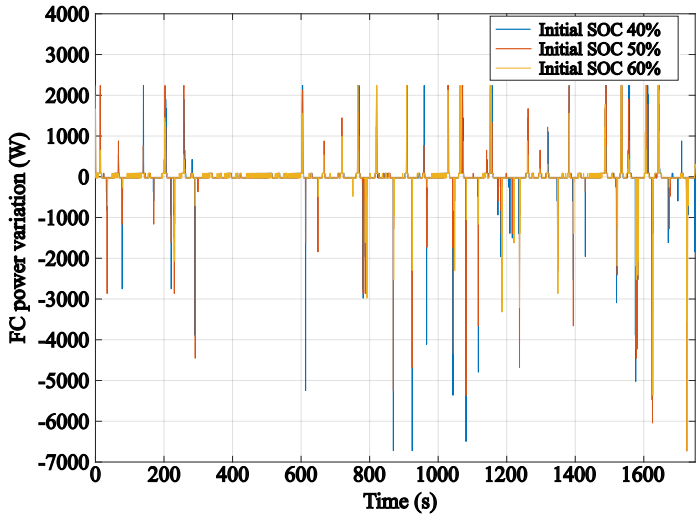

Figure 5.29: WLTP optimal FC power variation trajectories for 40%, 50%, and 60% initial SOC

The plots for the same variables shown for the WLTP drive cycle are shown for the HWFET and UDDS drive cycles below. The optimal SOC trajectories, FC voltage trajectories, FC power trajectories, and the optimal control trajectories for the HWFET drive cycle are shown in figs. 5.30, 5.31, 5.32, and 5.33, respectively. These parameters in the same order for the UDDS drive cycle are shown in figs. 5.34, 5.35, 5.36, and 5.37 below.

In the DP results for the UDDS drive cycle, it can be observed that the FC voltage remains high throughout most of the cycle. This is because the UDDS drive cycle demands less power than the other ones, and the battery SOC must deplete 10% until the cycle's end. Therefore, the FC voltage must stay high to allow the battery to discharge and reach the final required SOC level. As shown previously, high voltage regions in FCs correspond to lower power production, which justifies these values.

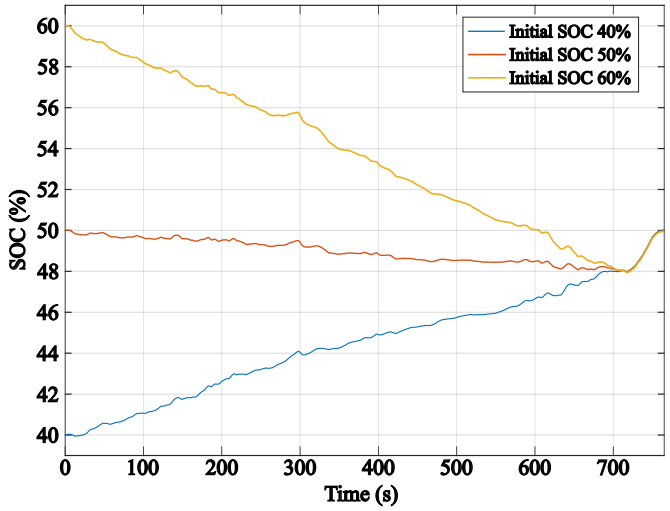

Figure 5.30: HWFET optimal SOC trajectories for 40%, 50%, and 60% initial SOC

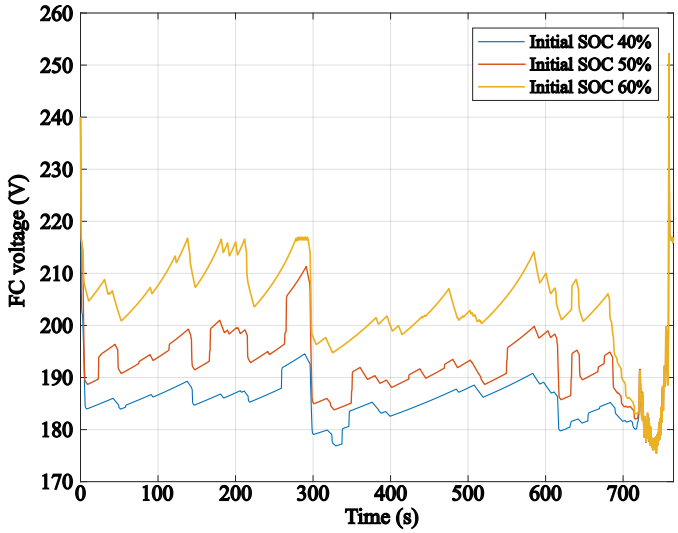

Figure 5.31: HWFET optimal FC voltage trajectories for 40%, 50%, and 60% initial SOC

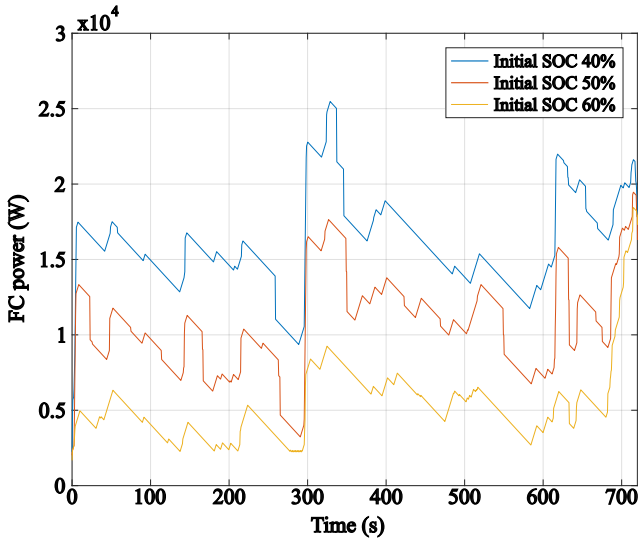

Figure 5.32: HWFET optimal FC power trajectories for 40%, 50%, and 60% initial SOC

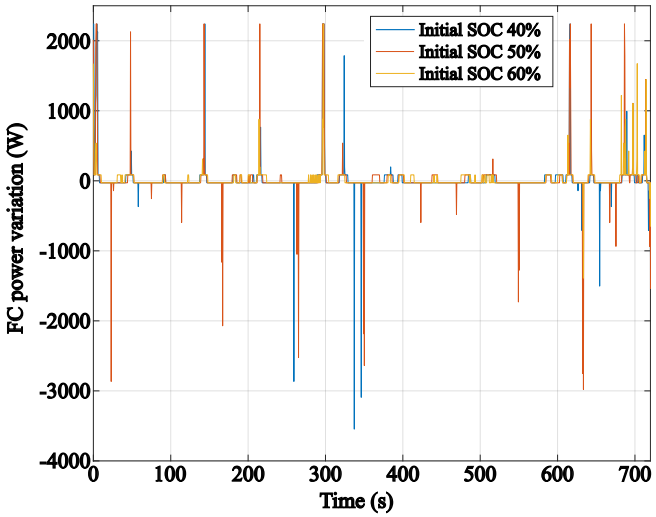

Figure 5.33: HWFET optimal FC power variation trajectories for 40%, 50%, and 60% initial SOC

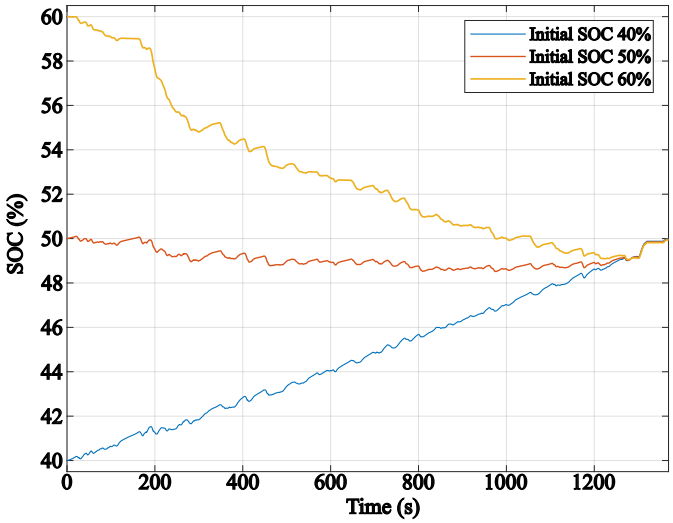

Figure 5.34: UDDS optimal FC SOC trajectories for 40%, 50%, and 60% initial SOC

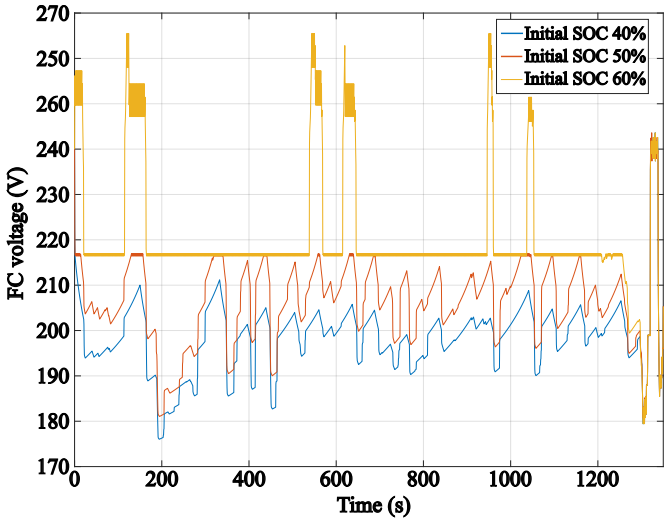

Figure 5.35: UDDS optimal FC voltage trajectories for 40%, 50%, and 60% initial SOC

Fig. 5.36 illustrates the mentioned low power values. Even though the FC avoid turning off due to the aging that would be generated. When the initial SOC is 50%

or 40%, the FC experiences lower voltage values, as it needs to produce more power to ensure the battery finishes the drive cycle with a SOC close to 50%.

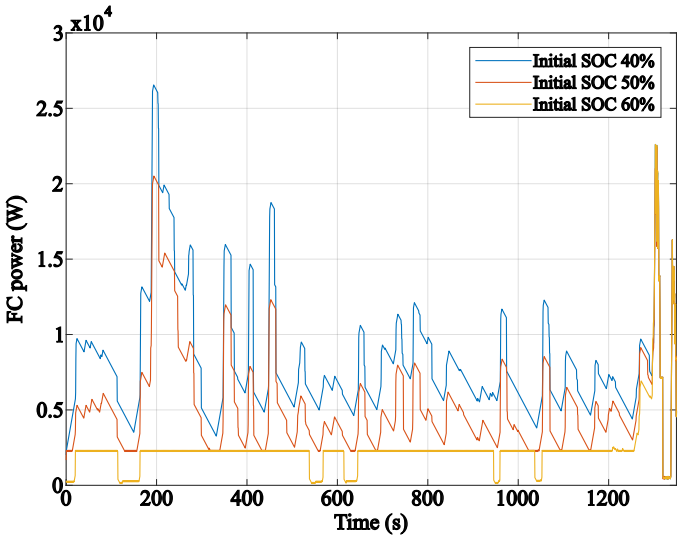

Figure 5.36: UDDS optimal FC power trajectories for 40%, 50%, and 60% initial SOC

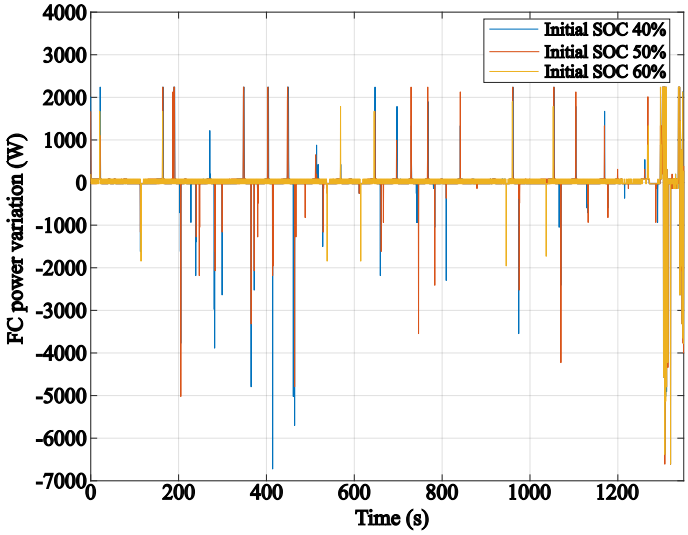

Figure 5.37: UDDS optimal FC power variation trajectories for 40%, 50%, and 60% initial SOC

5.3 Optimized controller for real-time implementation through Neural Network training

As mentioned in the previous section, the DP code is run from three different initial SOCs for each drive cycle. If only initial SOCs of 50% were used, the NN could not be trained across a wide range of SOC values. This is because starting from 50% makes the SOC vary slightly for all the drive cycles analyzed. The problem emerges once the LUTs to control the FCEV are created from the NN results and applied to the FCEV. When tested in the main vehicle model, the vehicle operates differently than in the DP. More specifically, the SOC reached regions where the NN was not trained. Therefore, using two additional initial SOC values ensures the NN is trained over a broader range.

5.3.1 Neural network LUT-based real-time controller development

As the DP results are executed three times per drive cycle, each using time steps of 0.5 seconds, 23,610 samples will be generated, divided according to table 5.8. These samples are utilized to train, validate, and test the NN. The network generated is then used to create two 2-D LUTs. The distribution of the samples is as follows: 80% are allocated for training, 15% for validation, and 5% for testing.

Table 5.8: Samples generated from DP to the NN per drive cycle

Drive cycle	**Cycle duration**	**Samples generated**
WLTP	1800	10800
HWFET	766	4596
UDDS	1369	8214

The inputs to the NN include the vehicle speed, battery SOC, FC power from the previous time step, and vehicle power demand. The NN output is the variation in FC power, which also serves as the control variable in the DP code.

A two-branch NN is utilized, with inputs grouped into two pairs. The first branch uses the SOC and previous FC power values, while the second handles vehicle speed and vehicle power demand. Both branches use the same output, which is the variation in FC power.

Before training the NN, the samples must be shuffled to avoid overfitting. Besides, the data must be normalized before training the NN. Here the z-score method was used to do it, which is described by eq. 5.3.1. In this equation, x is the observed value of the sample, μ is the sample's mean, and α is the standard deviation of the sample. After training the NN, the output values are denormalized by isolating x in eq. 5.3.1 before creating the LUTs that control the FC and battery in the main vehicle model.

$$Z = \frac{x - \mu}{\alpha} \tag{5.3.1}$$

Finally, the two generated LUTs are illustrated in fig. 5.38, which shows inputs of SOC and FC power, and fig. 5.39, which use vehicle speed and vehicle power demand

as inputs.

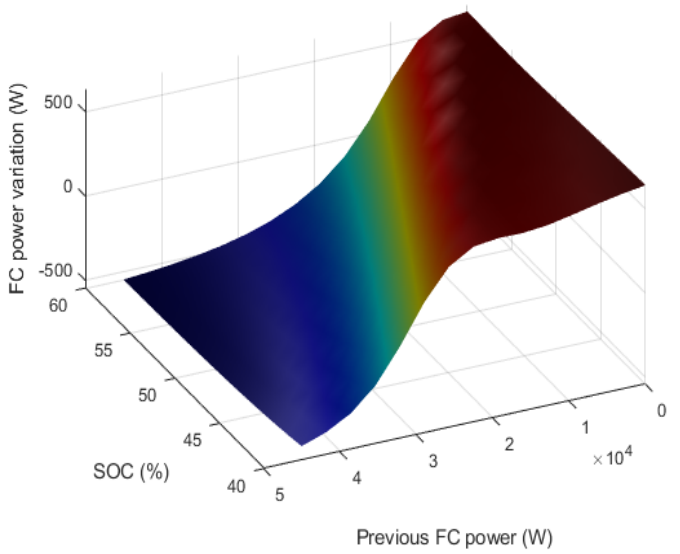

(a) View 1

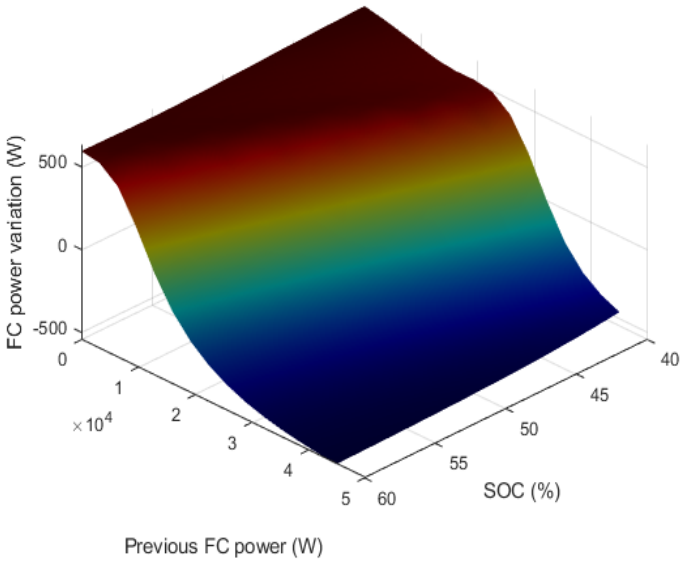

(b) View 2

Figure 5.38: First LUT generated to define the FC power variation from SOC and previous FC power inputs

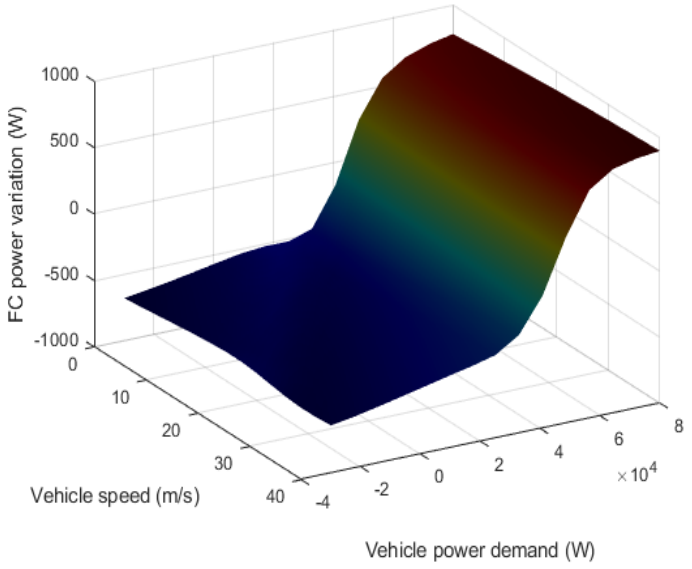

(a) View 1

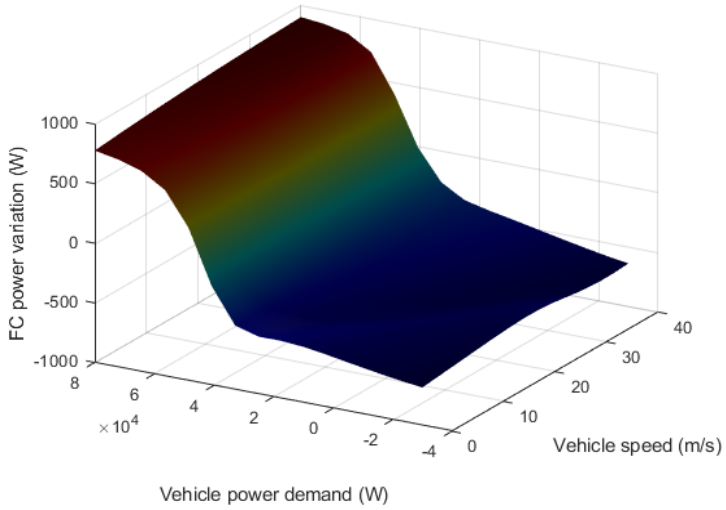

(b) View 2

Figure 5.39: Second LUT generated to define the FC power variation from vehicle speed and vehicle power demand

To generate these tables, grids were created for each of the inputs using 15 values for each of them. All possible combinations for the values of each pair of inputs were

used to predict the output of the NN net, creating the LUTs. The range of the values tested is shown in table 5.9.

To generate these LUTs, grids were created for each input using 15 different values. All possible combinations of the two input pairs were then used to predict the NN output, thereby creating the LUTs. The range of values tested is shown in table 5.9.

Table 5.9: Inputs grids details to predict LUTs output values

Input	**Lower grid value**	**Higher grid value**	**Interval**
Vehicle speed (m/s)	0	40	2.857
Battery SOC (dec)	0.4	0.6	0.01423
Previous FC power (W)	0	45000	3,214.29
Vehicle power demand (W)	-30000	80000	7,857.143

Once the Luts are generated, they can be inserted into the main vehicle model. To do so, the subsystems shown in figs. 5.2 and 5.3 were replaced by the subsystem shown in figs. 5.40 and 5.41.

To properly define the sum of the LUTs outputs, both outputs must be multiplied by two coefficients whose sum equals one, as shown in eq. 5.3.2. This is why the gain blocks equal to 0.545 and 0.455 are used. Additionally, the DP code uses a time step of 0.5 s, whereas the main vehicle model simulation uses a time step of 0.01 s. Therefore, the value must be adjusted since the NN predicts variations in FC power for a 0.5 s interval.

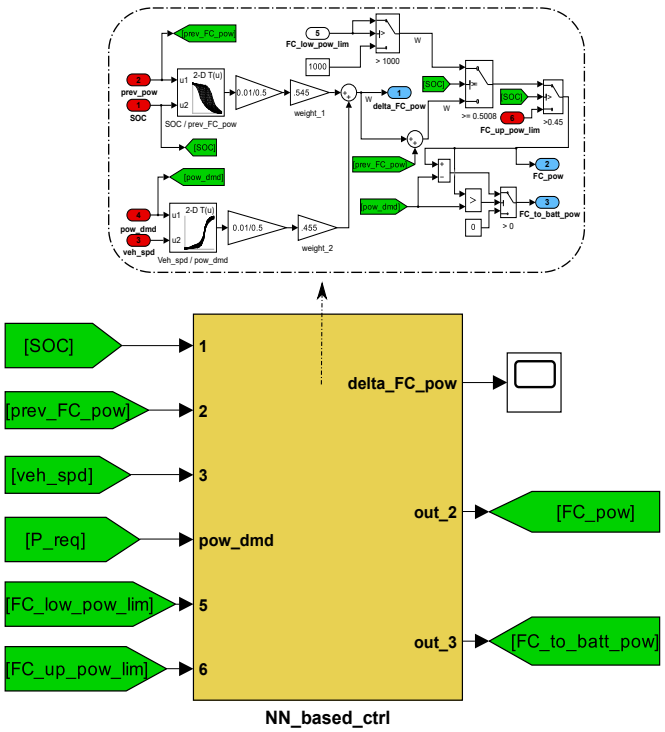

Figure 5.40: LUT-based EMS inside the controller subsystem of the main vehicle model - Layer 1

Some constraints are also applied to avoid the SOC going down excessively or increasing excessively. When the battery SOC increases over 50.8%, the FC output power goes to 1000 W. It makes the battery SOC decrease and, at the same time, prevents the FC from shutting down or operating in a zone of efficiency too low. On the other hand, when the SOC goes below 45%, the FC is requested to output the maximum power possible to prevent the battery from discharging excessively. Otherwise, while the battery SOC is between 45% and 50.8%, the FC power output is determined exclusively by the LUTs.

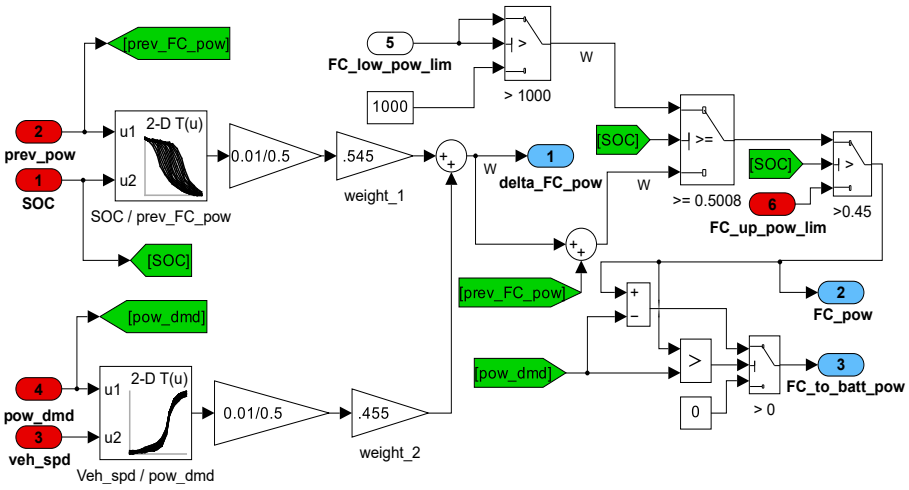

Figure 5.41: LUT-based EMS inside the controller subsystem of the main vehicle model - Layer 2

In the eq. 5.3.2, the ΔP_{FC_out} is the variation in the FC power output in the main vehicle model.

$$\begin{cases} (\alpha \cdot \Delta P_{FC\_LUT\_1}) + (\beta \cdot \Delta P_{FC\_LUT\_2}) = \Delta P_{FC\_out} \\ \alpha + \beta = 1 \end{cases} \tag{5.3.2}$$

As seen in fig. 5.41, certain constraints are applied to prevent the SOC from dropping too low or rising too high. When the battery SOC exceeds 50.8%, the FC output power is set to 1000 W to decrease the SOC while avoiding shutting down the FC or operating it at a too-low-efficiency zone. On the other hand, when the SOC falls below 45%, the FC must output the maximum power possible to prevent excessive battery discharge. When the battery SOC is between 45% and 50.8%, the FC power output is determined exclusively by the LUTs.

5.3.2 Neural network LUT-based real-time controller results and discussion

The outcomes of the main vehicle model running one time in each drive cycle with LUTs generated are shown below. First, figs. 5.42, 5.43, and 5.44 demonstrate that the vehicle follows precisely the drive cycles with the strategy implemented.

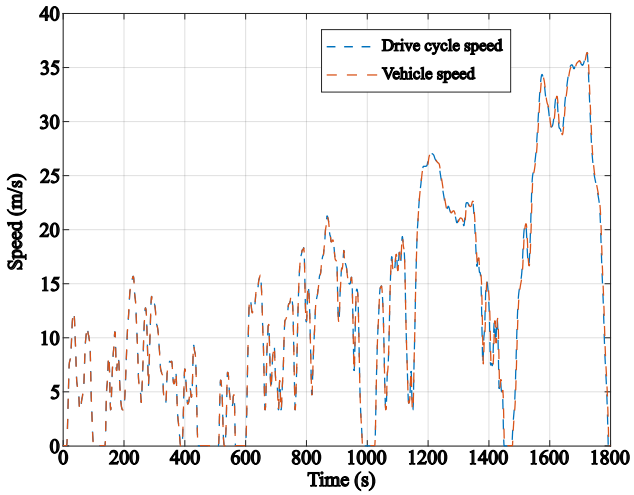

Figure 5.42: Vehicle speed profile with the LUT-based control strategy in WLTP

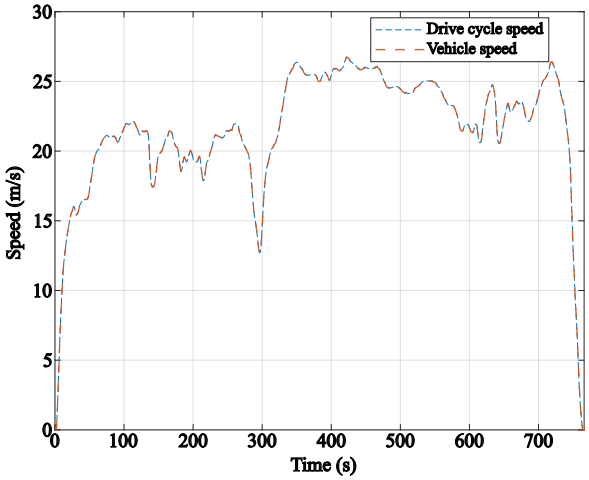

Figure 5.43: Vehicle speed profile with the LUT-based control strategy in HWFET

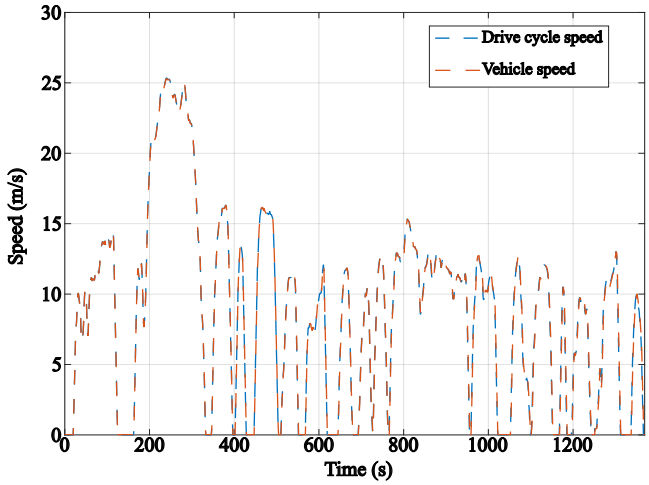

Figure 5.44: Vehicle speed profile with the LUT-based control strategy in UDDS

Figs. 5.45, 5.46, and 5.47 illustrate the power trajectories when the vehicle is controlled using the LUTs. These plots demonstrate how the controller makes the FC power variation smoother, avoiding unnecessary aging due to frequent and sharp power changes.

It can be observed now that the FC always operates in medium to low-power regions. The high-speed region in the WLTP drive cycle is the only period where the FC generates more than 20 kW. It helps to avoid aging caused by the high-power regions. Moreover, in the HWFET, the FC faces long periods operating between 10 and 20 kW with small power variation, which benefits energy consumption and FC duration.

It can now be observed that the FC consistently operates in medium to low-power regions. The FC only generates more than 20 kW during the high-speed segment of the WLTP drive cycle. This helps to avoid aging caused by high-power operations. In the HWFET cycle, the FC operates for extended periods between 10 and 20 kW with minimal power variation, benefiting energy consumption, as this region has high

efficiency and FC longevity.

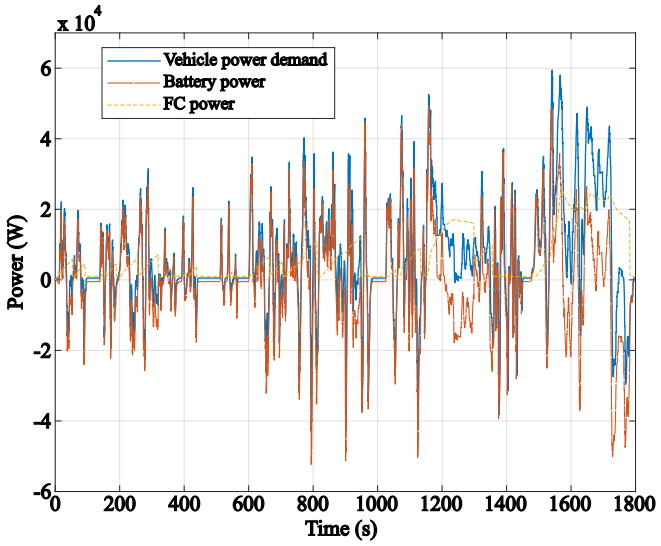

Figure 5.45: Power profiles with the LUT-based control strategy in WLTP

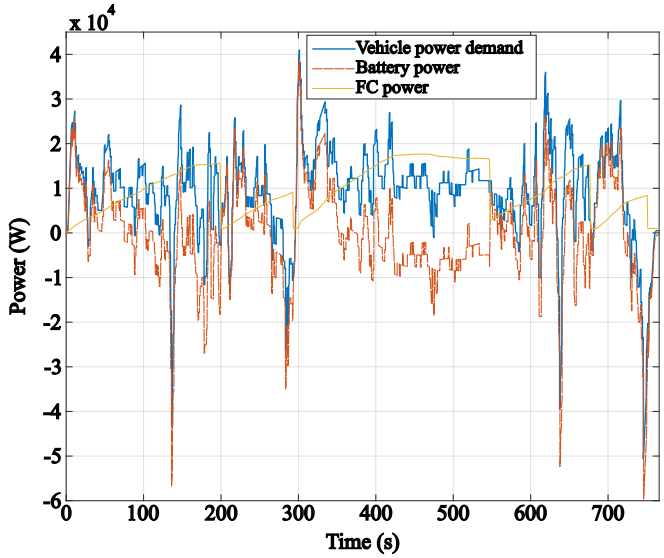

Figure 5.46: Power profiles with the LUT-based control strategy in HWFET

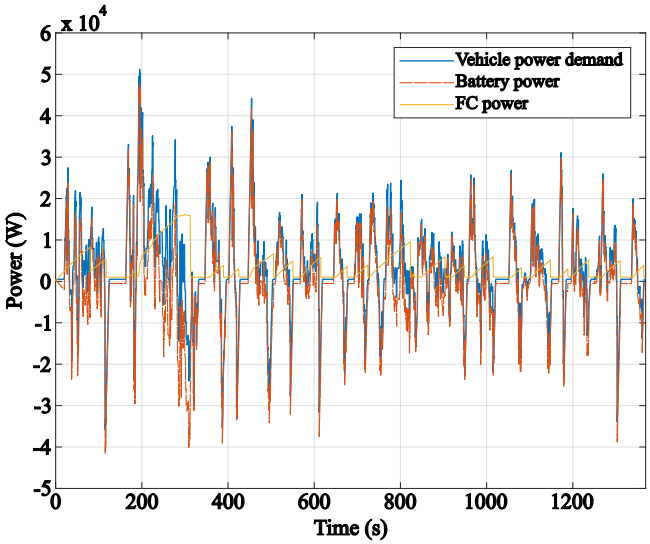

Figure 5.47: Power profiles with the LUT-based control strategy in UDDS

The SOC trajectories when the vehicle runs each drive cycle one time with the LUTs are shown in figs. 5.48, 5.48, and 5.48. Now, the SOC varies more, reaching almost 45% in the WLTP drive cycle. It is not a big issue, as the SOC level can reach 50% again at the end of the drive cycle.

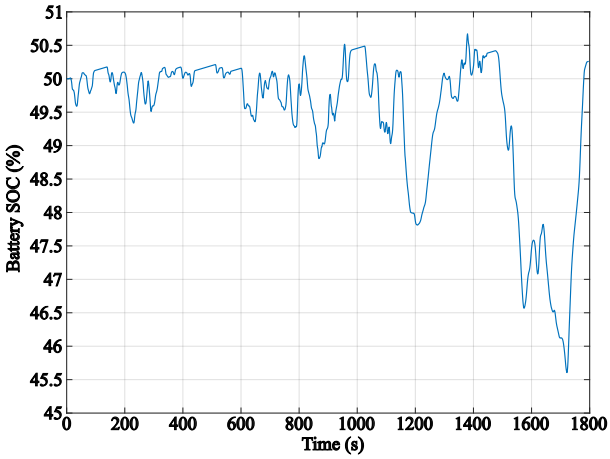

Figure 5.48: Battery SOC trajectory in WLTP with the LUT-based control strategy

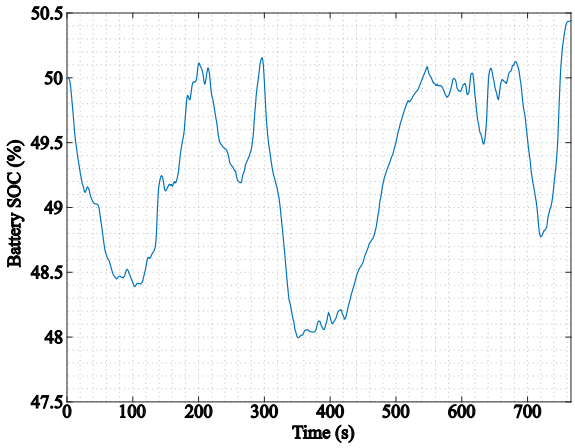

Figure 5.49: Battery SOC trajectory in HWFET with the LUT-based control strategy

In UDDS, the battery SOC only faces a more pronounced drop at the beginning of the drive cycle when the vehicle demands more power. After 400 seconds, the SOC stays very close to 50% during all the drive cycles.

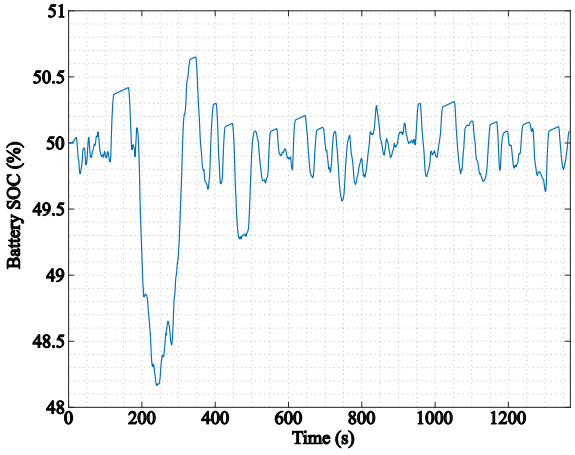

Figure 5.50: Battery SOC trajectory in UDDS with the LUT-based control strategy

The FC and battery SOH depletion trajectories for one drive cycle run with the LUTs can be seen in figs. 5.51, 5.52, and 5.53. Compared with the previous rule-based

method, the FC SOH does not deplete as fast as before. Mainly for the HWFET drive cycle, the FC SOH level remains almost constant in periods where the FC power varies slightly.

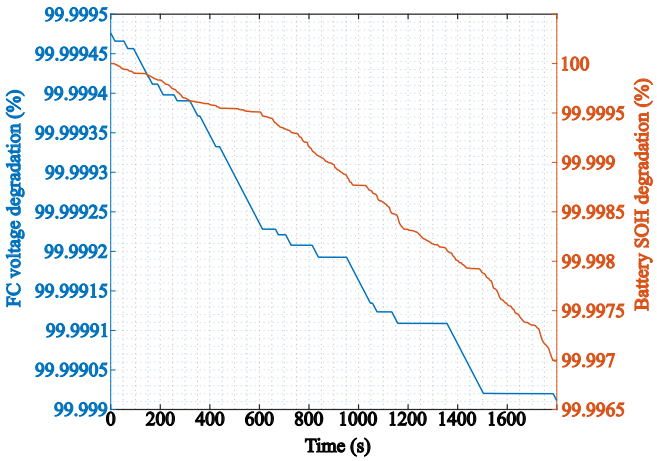

Figure 5.51: Degradation of FC and Battery after one run of WLTP with the LUT-based control strategy

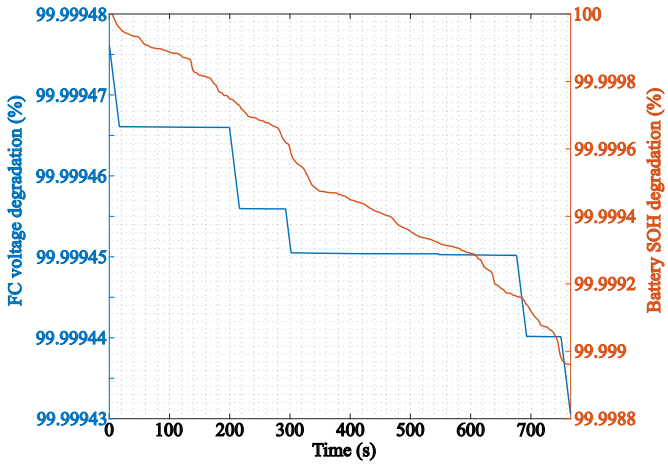

Figure 5.52: Degradation of FC and Battery after one run of HWFET with the LUT-based control strategy

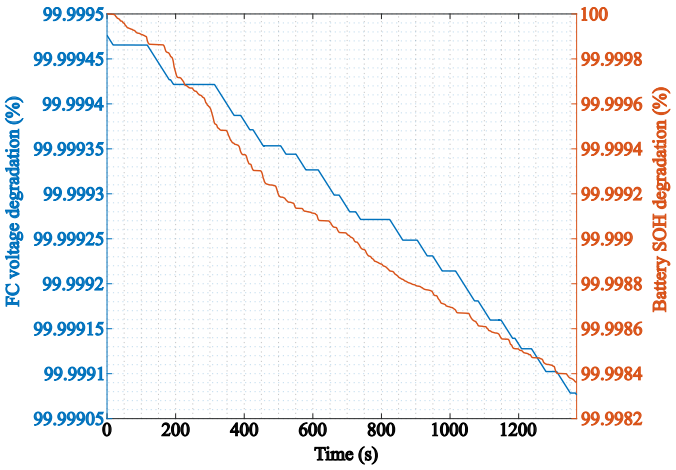

Figure 5.53: Degradation of FC and Battery after one run of UDDS with the LUT-based control strategy

Finally, the hydrogen consumption curves with the LUT-based control strategy can be seen in figs. 5.54, 5.55, and 5.56. Compared with the previous rule-based strategy results, hydrogen consumption decreased considerably in all drive cycles.

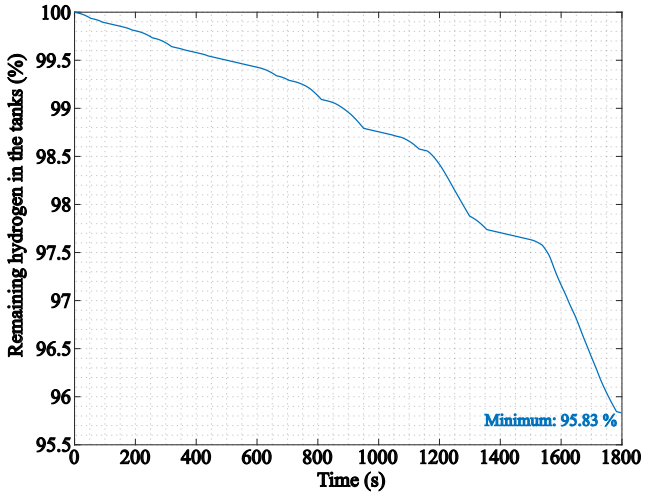

Figure 5.54: Hydrogen consumption in WLTP with the LUT-based control strategy

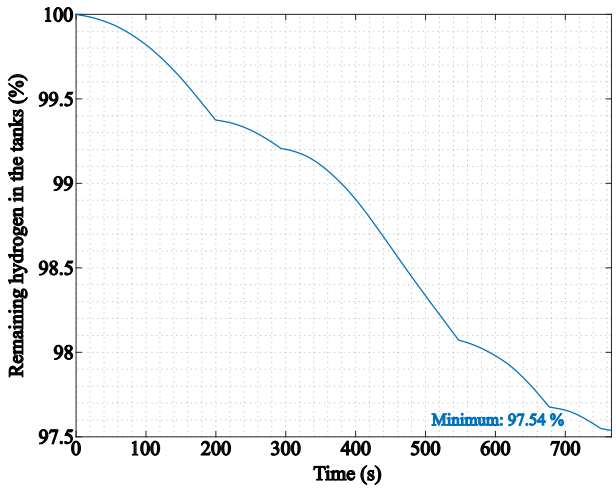

Figure 5.55: Hydrogen consumption in HWFET with the LUT-based control strategy

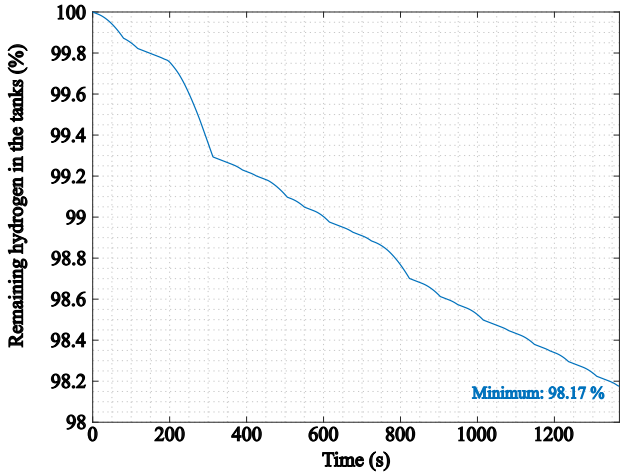

Figure 5.56: Hydrogen consumption in UDDS with the LUT-based control strategy

The estimated range of the modelled FC electric van is shown below in table 5.10. Higher values of range are achieved for all the drive cycles.

Table 5.10: Range of the FCEV for multiple drive cycles in the FC and battery BOL

Drive Cycle	**Distance (km)**	**Range (km)**	**Hydrogen consumption (l/100 km)**
WLTP	23.26	561.64	13.76
HWFET	16.45	672.8	11.489
UDDS	12	658.83	11.733

Compared to the first proposed rule-based strategy at the FC EOL, the car demonstrates higher range numbers for the WLTP and UDDS drive cycles but achieves a lower range in the HWFET drive cycle. These results are summarized in table 5.11.

Table 5.11: Parameters at the EOL of the FC operating with the NN-based strategy

Drive cycle	**Hours of operation**	**Total distance (km)**	**Number of cycles**	**Range at the FC EOL (km)**	**Hydrogen consumption (l/ 100 km)**
WLTP	5092	236,880	10184	535.61	14.43
HWFET	3653.8	282,847	17172	621.46	12.438
UDDS	4137.04	168,604	10879	633.78	12.197

Table 5.12 compares the performance of the two real-time implemented strategies, LUT-based and the first rule-based, focusing on vehicle autonomy and durability. Notably, the LUT-based strategy enables the FCEV to travel longer distances before refuelling under the WLTP and UDDS drive cycles. However, the HWFET drive cycle performs slightly worse at the BOL than at the EOL regarding distance before

refuelling. Additionally, the LUT-based strategy consistently allows the vehicle to operate significantly longer before the FC needs replacement across all drive cycles.

Table 5.12: Advantages of the LUT-based Strategy Compared to the rule-based Strategy

Drive cycle	**Range at the BOL**	**Range at the EOL**	**Hours of operation**
WLTP	6.34%	7.9%	15.92%
HWFET	- 0.997%	- 4.32%	9.49%
UDDS	2.65%	1.67%	9.25%

Chapter 6

Conclusions and future work

The FCEV model developed in this study predicts hydrogen consumption and range depletion over the lifespan of powertrain components, considering the evolving characteristics of the FC and battery. This approach yields more realistic results than many existing studies that do not consider these changes. The research demonstrates that integrating feed-forward NN predictions with DP results can enhance the FCEV's range in most situations and reduce the aging of components, thus extending the vehicle's operational time without refuelling compared to the initially implemented rule-based strategy. The comparison was conducted at the BOL of the FC and battery and the EOL of the FC. The LUT-based strategy generally outperforms the rule-based strategy in the WLTP and UDDS drive cycles regarding range before the need to refuelling. However, in the HWFET cycle, the rule-based strategy allows the car to operate slightly longer at the BOL, increasing this advantage at the EOL. One possible explanation is the significantly fewer samples from the HWFET used to train the NN due to the HWFET's shorter duration compared to the WLTP and UDDS by 57.45% and 44.05%, respectively.

When comparing the decay in range over the lifespan of the FC, the rule-based strategy shows a decay of 6.015% in WLTP, 3.77% in HWFET, and 2.878% in UDDS along the life of the FC and battery. Meanwhile, the LUT-based strategy exhibits a decay 4.635% in WLTP, 7.631% in HWFET, and 3.802% in UDDS. Thus, the LUT-based strategy performs better in two analyzed drive cycles.

When comparing the total operational hours of the vehicle across each drive cycle before the FC needs replacement, the LUT-based strategy outperforms the first rule-based in all three drive cycles. Specifically, it shows improvements of 15.92% in the WLTP, 9.49% in HWFET, and 9.25% in UDDS.

Despite implementing power variation limits for the FC, it's observed that FC power still fluctuates significantly at times when using the rule-based strategy. In contrast, the LUT-based strategy ensures smoother power variations. This smoother operation helps preserve the FC, contributing to more operational hours before the EOL is reached.

It can also be observed that, independently of which of the two real-time implementable strategies adopted, there is a similar trend in hydrogen consumption in all the drive cycles. In WLTP, the consumption tends to be higher close to the end of the drive cycle, while in HWFET it tends to be stable along the drive cycle, and in UDDS it tends to be higher in the beginning.

Future research will focus on training the NN with additional inputs to reduce hydrogen consumption further and slow down FC and battery degradation.

Additionally, implementing the developed control strategy on a physical controller and using a real battery cell to replace the virtual battery pack with specifications from this study could confirm if the simulated SOC trajectories are consistent with

real-world results.

Moreover, implementing the FCS model in the main vehicle model and developing a controller with both supervisory control and low-level control to not only control the power between the FC and battery but also the turn on and turn off of the radiator fan, open and close of the radiator the by-pass valve, and analyzing the operation from cold-start to enhance the range of the vehicle, could improve further the hydrogen consumption results.

Further experimental studies on FC aging, including tracking changes in polarization and efficiency curves over time and incorporating these findings into the model, could significantly improve its accuracy and reliability.

Lastly, integrating the FCS model into the main vehicle model and developing a dual-level control strategy (supervisory and low-level control) to enhance hydrogen efficiency could be done. This system would manage the power distribution between the FC and battery, operate the radiator fan, and regulate the radiator bypass valve. Analyzing operations from a cold start could provide more realistic results.

References

[1] The Detroit News, "Stellantis to sell hydrogen-powered commercial vans this year in europe." https://www.detroitnews.com, 2021. Accessed: 2024-02-05.

[2] Stellantis, "Opel vivaro-e hydrogen: Plug-in fuel cell electric vehicle offers zero emissions and quick refuelling." https://www.media.stellantis.com/em-en/opel/media-library/press-images/366517, 2024. Accessed: 2024-03-07.

[3] Opel, "Opel vivaro combi electric price and spec guide." https://www.opel.ie/content/dam/opel/ireland/vehicles, 2023. Accessed: 2024-01-24.

[4] S. Aminzadegan, M. Shahriari, F. Mehranfar, and B. Abramović, "Factors affecting the emission of pollutants in different types of transportation: A literature review," *Energy Reports*, vol. 8, pp. 2508–2529, 2022.

[5] F. Perera and K. Nadeau, "Climate change, fossil-fuel pollution, and children's health," *New England Journal of Medicine*, vol. 386, no. 24, pp. 2303–2314, 2022.

[6] M. Hossain, L. Kumar, M. El Haj Assad, and R. Alayi, "Advancements and future prospects of electric vehicle technologies: a comprehensive review," *Complexity*, vol. 2022, no. 1, p. 3304796, 2022.

[7] W. Zhou, C. J. Cleaver, C. F. Dunant, J. M. Allwood, and J. Lin, "Cost, range anxiety and future electricity supply: A review of how today's technology trends may influence the future uptake of bevs," *Renewable and Sustainable Energy Reviews*, vol. 173, p. 113074, 2023.

[8] A. König, L. Nicoletti, D. Schröder, S. Wolff, A. Waclaw, and M. Lienkamp, "An overview of parameter and cost for battery electric vehicles," *World Electric Vehicle Journal*, vol. 12, no. 1, p. 21, 2021.

[9] R. Guo, F. Wang, M. A. Rhamdhani, Y. Xu, and W. Shen, "Managing the surge: a comprehensive review of the entire disposal framework for retired lithium-ion batteries from electric vehicles," *Journal of Energy Chemistry*, 2024.

[10] P. Point, "How long to charge an electric car." `https://pod-point.com/guides/driver/how-long-to-charge-an-electric-car`, 2024. Accessed: 2024-07-22.

[11] H. Sahin, "Hydrogen refueling of a fuel cell electric vehicle," *International Journal of Hydrogen Energy*, 2024.

[12] Nikola Motor, "Walmart canada becomes the first major retailer in canada to introduce a hydrogen fuel cell electric semi-truck." `https://www.nikolamotor.com`, June 2024. Accessed: 2024-06-29.

[13] Toyota Canada, "Toyota canada and edmonton international airport (yeg) partner to bring 100 zero-emission hydrogen fuel cell electric vehicles to alberta roadways." `https://www.toyota.ca/toyota/en/about/news`, July 2023. Accessed: 2023-12-23.

[14] H. H. Cho, V. Strezov, and T. J. Evans, "A review on global warming potential, challenges and opportunities of renewable hydrogen production technologies," *Sustainable Materials and Technologies*, vol. 35, p. e00567, 2023.

[15] X. Li, K. Han, and Y. Song, "Dynamic behaviors of pem fuel cells under load changes," *International Journal of Hydrogen Energy*, vol. 45, no. 39, pp. 20312–20320, 2020.

[16] National Renewable Energy Laboratory, "Fuel cell electric vehicle durability and fuel cell performance." `https://www.nrel.gov/docs/fy19osti/73011.pdf`, 2019. Accessed: 03/01/2024.

[17] Alternative Fuels Data Center, "Alternative fueling station locator." `https://afdc.energy.gov/stations#/find/nearest?fuel=HY`, 2024. Accessed: 2024-06-17.

[18] J. Bauman and M. Kazerani, "A comparative study of fuel-cell–battery, fuel-cell–ultracapacitor, and fuel-cell–battery–ultracapacitor vehicles," *IEEE Transactions on Vehicular Technology*, vol. 57, no. 2, pp. 760–769, 2008.

[19] M. İnci, M. Büyük, M. H. Demir, and G. İlbey, "A review and research on fuel cell electric vehicles: Topologies, power electronic converters, energy management methods, technical challenges, marketing and future aspects," *Renewable and Sustainable Energy Reviews*, vol. 137, p. 110648, 2021.

[20] R. T. Doucette and M. D. McCulloch, "A comparison of high-speed flywheels, batteries, and ultracapacitors on the bases of cost and fuel economy as the

energy storage system in a fuel cell based hybrid electric vehicle," *Journal of Power Sources*, vol. 196, no. 3, pp. 1163–1170, 2011.

[21] H. Lohse-Busch, K. Stutenberg, M. Duoba, X. Liu, A. Elgowainy, M. Wang, T. Wallner, B. Richard, and M. Christenson, "Automotive fuel cell stack and system efficiency and fuel consumption based on vehicle testing on a chassis dynamometer at minus 18 °c to positive 35 °c temperatures," *International Journal of Hydrogen Energy*, vol. 45, no. 1, pp. 861–872, 2020.

[22] W. Zhou, L. Yang, Y. Cai, and T. Ying, "Dynamic programming for new energy vehicles based on their work modes part ii: Fuel cell electric vehicles," *Journal of Power Sources*, vol. 407, pp. 92–104, 2018.

[23] P. Yu, M. Li, Y. Wang, and Z. Chen, "Fuel cell hybrid electric vehicles: A review of topologies and energy management strategies," *World Electric Vehicle Journal*, vol. 13, no. 9, 2022.

[24] M. Waseem, M. Amir, G. S. Lakshmi, S. Harivardhagini, and M. Ahmad, "Fuel cell-based hybrid electric vehicles: An integrated review of current status, key challenges, recommended policies, and future prospects," *Green Energy and Intelligent Transportation*, vol. 2, no. 6, p. 100121, 2023.

[25] Stellantis, "Hydrogen fuel cell zero emission." `https://www.stellantis.com/content/dam/stellantis-corporate/news/media-events/HYDROGEN-FUEL-CELL-ZERO-EMISSION_PRESSKIT.pdf`, 2021. Accessed: 2023-12-21.

[26] Hyundai Motor America, "2023 hyundai nexo fuel cell - specifications and features." http://www.hyundaiusa.com/us/en/vehicles/nexo/compare-specs, 2023. Accessed: 2023-12-21.

[27] Toyota Motor Corporation, "2024 toyota mirai - mpg, other features, and pricing." https://www.toyota.com/mirai/2024/features/mpg_other_price/3002/3003, 2024. Accessed: 2024-05-14.

[28] Honda Motor Company, "2021 clarity fuel cell specifications and features." https://hondanews.com/en-US/honda-automobiles/releases, 2021. Accessed: 2024-06-06.

[29] Nikola Corporation, "Nikola tre fcev - hydrogen fuel cell electric vehicle." https://www.nikolamotor.com/tre-fcev, 2023. Accessed: 2024-06-02.

[30] Stellantis, "Hydrogen fuel cell technology." https://www.stellantis.com/en/technology/hydrogen-fuel-cell-technology, 2023. Accessed: 2024-06-01.

[31] Symbio, "Stackpack 40 fuel cell." https://www.symbio.one/en/hydrogen-solutions/our-h2motive-range/stackpack-40-fuel-cell. Accessed: 2024-06-03.

[32] European Automobile Manufacturers' Association, "What is wltp and how will it work?." https://www.wltpfacts.eu/what-is-wltp-how-will-it-work/, 2023. Accessed: 2024-01-22.

[33] TransportPolicy.net, "International: Light-duty: Worldwide harmonized light vehicles test procedure (wltp)." https://www.transportpolicy.net/standard, 2023. Accessed: 2024-03-02.

[34] J. Desantes, R. Novella, B. Pla, and M. Lopez-Juarez, "A modeling framework for predicting the effect of the operating conditions and component sizing on fuel cell degradation and performance for automotive applications," *Applied Energy*, vol. 317, p. 119137, 2022.

[35] Y. Guezennec, T.-Y. Choi, G. Paganelli, and G. Rizzoni, "Supervisory control of fuel cell vehicles and its link to overall system efficiency and low-level control requirements," in *Proceedings of the 2003 American Control Conference, 2003.*, vol. 3, pp. 2055–2061, IEEE, 2003.

[36] P. G. Anselma and G. Belingardi, "Fuel cell electrified propulsion systems for long-haul heavy-duty trucks: present and future cost-oriented sizing," *Applied Energy*, vol. 321, p. 119354, 2022.

[37] M. Kandidayeni, A. Macias, L. Boulon, and S. Kelouwani, "Investigating the impact of ageing and thermal management of a fuel cell system on energy management strategies," *Applied Energy*, vol. 274, p. 115293, 2020.

[38] *Fuel Cell Systems Explained*, ch. 2, pp. 27–41. John Wiley & Sons, Ltd, 2018.

[39] A. C. Codina, "System level modelling of fuel cell driven electric vehicles," 2017.

[40] C. Spiegel, "Chapter 3 - fuel cell electrochemistry," in *PEM Fuel Cell Modeling and Simulation Using Matlab* (C. Spiegel, ed.), pp. 49–76, Burlington: Academic Press, 2008.

[41] *Operational Fuel-Cell Voltages*, ch. 3, pp. 43–68. John Wiley & Sons, Ltd, 2018.

[42] A. Kongkanand, W. Gu, and M. F. Mathias, "Proton-exchange membrane fuel

cells with low-pt content," *Fuel Cells and Hydrogen Production. Encyclopedia of Sustainability Science and Technology Series*.

[43] J. Bernard, S. Delprat, F. N. Buchi, and T. M. Guerra, "Fuel-cell hybrid powertrain: Toward minimization of hydrogen consumption," *IEEE Transactions on Vehicular Technology*, vol. 58, no. 7, pp. 3168–3176, 2009.

[44] J. Hoeflinger and P. Hofmann, "Air mass flow and pressure optimisation of a pem fuel cell range extender system," *international journal of hydrogen energy*, vol. 45, no. 53, pp. 29246–29258, 2020.

[45] U.S. Department of Energy, "Types of fuel cells." `https://www.energy.gov/eere/fuelcells/types-fuel-cells`, 2019. Accessed: 2024-02-13.

[46] P. Pei, Q. Chang, and T. Tang, "A quick evaluating method for automotive fuel cell lifetime," *International Journal of Hydrogen Energy*, vol. 33, no. 14, pp. 3829–3836, 2008.

[47] K. Song, H. Chen, P. Wen, T. Zhang, B. Zhang, and T. Zhang, "A comprehensive evaluation framework to evaluate energy management strategies of fuel cell electric vehicles," *Electrochimica Acta*, vol. 292, pp. 960–973, 2018.

[48] Y. Liu, J. Li, Z. Chen, D. Qin, and Y. Zhang, "Research on a multi-objective hierarchical prediction energy management strategy for range extended fuel cell vehicles," *Journal of Power Sources*, vol. 429, pp. 55–66, 2019.

[49] H. Chen, P. Pei, and M. Song, "Lifetime prediction and the economic lifetime of proton exchange membrane fuel cells," *Applied Energy*, vol. 142, pp. 154–163, 2015.

[50] T. Takahashi, T. Ikeda, K. Murata, O. Hotaka, S. Hasegawa, Y. Tachikawa, M. Nishihara, J. Matsuda, T. Kitahara, S. M. Lyth, *et al.*, "Accelerated durability testing of fuel cell stacks for commercial automotive applications: A case study," *Journal of The Electrochemical Society*, vol. 169, no. 4, p. 044523, 2022.

[51] G. Wang, F. Huang, Y. Yu, S. Wen, and Z. Tu, "Degradation behavior of a proton exchange membrane fuel cell stack under dynamic cycles between idling and rated condition," *International journal of hydrogen energy*, vol. 43, no. 9, pp. 4471–4481, 2018.

[52] D. Bezmalinovic, B. Simic, and F. Barbir, "Characterization of pem fuel cell degradation by polarization change curves," *Journal of Power Sources*, vol. 294, pp. 82–87, 2015.

[53] K. Song, Y. Ding, X. Hu, H. Xu, Y. Wang, and J. Cao, "Degradation adaptive energy management strategy using fuel cell state-of-health for fuel economy improvement of hybrid electric vehicle," *Applied Energy*, vol. 285, p. 116413, 2021.

[54] D. Shen, C.-C. Lim, and P. Shi, "Fuzzy model based control for energy management and optimization in fuel cell vehicles," *IEEE transactions on vehicular technology*, vol. 69, no. 12, pp. 14674–14688, 2020.

[55] J. Xu, C. Zhang, R. Fan, H. Bao, Y. Wang, S. Huang, C. S. Chin, and C. Li, "Modelling and control of vehicle integrated thermal management system of pem fuel cell vehicle," *Energy*, vol. 199, p. 117495, 2020.

[56] H. Lohse-Busch, K. Stutenberg, M. Duoba, X. Liu, A. Elgowainy, M. Wang,

T. Wallner, B. Richard, and M. Christenson, "Automotive fuel cell stack and system efficiency and fuel consumption based on vehicle testing on a chassis dynamometer at minus 18 c to positive 35 c temperatures," *International Journal of Hydrogen Energy*, vol. 45, no. 1, pp. 861–872, 2020.

[57] B. Jian and H. Wang, "Hardware-in-the-loop real-time validation of fuel cell electric vehicle power system based on multi-stack fuel cell construction," *Journal of Cleaner Production*, vol. 331, p. 129807, 2022.

[58] Y. Zhou, H. Li, A. Ravey, and M.-C. Péra, "An integrated predictive energy management for light-duty range-extended plug-in fuel cell electric vehicle," *Journal of Power Sources*, vol. 451, p. 227780, 2020.

[59] A. Omran, A. Lucchesi, D. Smith, A. Alaswad, A. Amiri, T. Wilberforce, J. R. Sodré, and A. Olabi, "Mathematical model of a proton-exchange membrane (pem) fuel cell," *International Journal of Thermofluids*, vol. 11, p. 100110, 2021.

[60] H. Xiao, L. Shikun, S. Ke, G. Yuan, and Z. Tong, "Novel fuzzy control energy management strategy for fuel cell hybrid electric vehicles considering state of health. energies 2021-01; 14 (20): 6481."

[61] W. Gao, Z. Hu, H. Huang, L. Xu, C. Fang, J. Li, C. Wang, and M. Ouyang, "All-condition economy evaluation method for fuel cell systems: System efficiency contour map," *eTransportation*, vol. 9, p. 100127, 2021.

[62] S. Pardhi, S. Chakraborty, D.-D. Tran, M. El Baghdadi, S. Wilkins, and O. Hegazy, "A review of fuel cell powertrains for long-haul heavy-duty vehicles:

Technology, hydrogen, energy and thermal management solutions," *Energies*, vol. 15, no. 24, p. 9557, 2022.

[63] P. G. Anselma, S. Luciani, and A. Tonoli, "Dynamic programming for thermal management of automotive fuel cell systems: Investigating hydrogen saving potential," *IEEE Access*, 2023.

[64] World Nuclear Association, "Heat values of various fuels." `https://www.world-nuclear.org/information-library/facts-and-figures/heat-values-of-various-fuels.aspx`, 2020. Accessed: 2024-02-10.

[65] CORECHEM Inc., "Ethylene glycol / water mixture properties." `https://corecheminc.com/ethylene-glycol-water-mixture-properties/`, 2024. Accessed: 2024-03-02.

[66] A. Szałek, I. Pielecha, and W. Cieslik, "Fuel cell electric vehicle (fcev) energy flow analysis in real driving conditions (rdc)," *Energies*, vol. 14, no. 16, p. 5018, 2021.

[67] Y. Li, P. Pei, Z. Ma, P. Ren, and H. Huang, "Analysis of air compression, progress of compressor and control for optimal energy efficiency in proton exchange membrane fuel cell," *Renewable and Sustainable Energy Reviews*, vol. 133, p. 110304, 2020.

[68] Rotrex, "Rotrex fuel cell compressor." `https://rotrex-fuel-cell-compressor.com/`. Accessed: 2024-01-18.

[69] I. Principe, *Thermal Modelling of a Fuel Cell System for an Electric Vehicle*. PhD thesis, Politecnico di Torino, 2021.

[70] S. D. Gurski, *Cold-start effects on performance and efficiency for vehicle fuel cell systems*. PhD thesis, Virginia Tech, 2002.

[71] W. Zou, J. Li, Q. Yang, X. Wan, Y. He, and H. Lan, "A real-time energy management approach with fuel cell and battery competition-synergy control for the fuel cell vehicle," *Applied Energy*, vol. 334, p. 120667, 2023.

[72] "Samsung 30t specifications sheet." `https://www.imrbatteries.com/content/samsung_30T.pdf`, 2017. Accessed: February 2024.

[73] S. Ebbesen, P. Elbert, and L. Guzzella, "Battery state-of-health perceptive energy management for hybrid electric vehicles," *IEEE Transactions on Vehicular technology*, vol. 61, no. 7, pp. 2893–2900, 2012.

[74] T. S. Miranda, A. Biswas, and A. Emadi, "Electric bus state-of-health aware cost analysis given energy consumption and initial battery purchase price," in *2023 IEEE Transportation Electrification Conference and Expo, Asia-Pacific (ITEC Asia-Pacific)*, pp. 1–8, IEEE, 2023.

[75] P. G. Anselma, P. Kollmeyer, J. Lempert, Z. Zhao, G. Belingardi, and A. Emadi, "Battery state-of-health sensitive energy management of hybrid electric vehicles: Lifetime prediction and ageing experimental validation," *Applied Energy*, vol. 285, p. 116440, 2021.

[76] A. Allca-Pekarovic, P. J. Kollmeyer, A. Forsyth, and A. Emadi, "Experimental characterization and modeling of a yasa p400 axial flux pm traction machine for performance analysis of a chevy bolt ev," *IEEE Transactions on Industry Applications*, 2023.

[77] P. Ahmadi, S. H. Torabi, H. Afsaneh, Y. Sadegheih, H. Ganjehsarabi, and M. Ashjaee, "The effects of driving patterns and pem fuel cell degradation on the lifecycle assessment of hydrogen fuel cell vehicles," *International Journal of Hydrogen Energy*, vol. 45, no. 5, pp. 3595–3608, 2020.

[78] S. Onori, L. Serrao, and G. Rizzoni, *Hybrid electric vehicles: Energy management strategies*, vol. 13. Springer, 2016.

[79] A. El Zerk and M. Ouassaid, "Real-time fuzzy logic based energy management system for microgrid using hardware in the loop," *Energies*, vol. 16, no. 5, p. 2244, 2023.

[80] M. K. Dayeni, A. Macias, C. Depature, L. Boulon, S. Kelouwani, and H. Chaoui, "Real-time fuzzy logic strategy scheme for energetic macroscopic representation of a fuel cell/battery vehicle," in *2017 IEEE Vehicle Power and Propulsion Conference (VPPC)*, pp. 1–6, IEEE, 2017.

[81] L. Bartolucci, E. Cennamo, S. Cordiner, V. Mulone, F. Pasqualini, and M. A. Boot, "Digital twin of a hydrogen fuel cell hybrid electric vehicle: Effect of the control strategy on energy efficiency," *International journal of hydrogen energy*, vol. 48, no. 54, pp. 20971–20985, 2023.

[82] L. Andaloro, G. Napoli, S. Micari, G. Dispenza, F. Sergi, P. Fragiacomo, and V. Antonucci, "Experimental activities on a pefc based powertrain for a hybrid electric minibus," *International Journal of Hydrogen Energy*, vol. 45, no. 58, pp. 34011–34023, 2020.

[83] X. Hu, S. Liu, K. Song, Y. Gao, and T. Zhang, "Novel fuzzy control energy

management strategy for fuel cell hybrid electric vehicles considering state of health," *Energies*, vol. 14, no. 20, p. 6481, 2021.

[84] L. Xu, C. D. Mueller, J. Li, M. Ouyang, and Z. Hu, "Multi-objective component sizing based on optimal energy management strategy of fuel cell electric vehicles," *Applied energy*, vol. 157, pp. 664–674, 2015.

[85] Y. Shen, P. Cui, X. Wang, X. Han, and Y.-X. Wang, "Variable structure battery-based fuel cell hybrid power system and its incremental fuzzy logic energy management strategy," *International Journal of Hydrogen Energy*, vol. 45, no. 21, pp. 12130–12142, 2020.

[86] U. Usmanov, S. Ruzimov, A. Tonoli, and A. Mukhitdinov, "Modeling, simulation and control strategy optimization of fuel cell hybrid electric vehicle," *Vehicles*, vol. 5, no. 2, pp. 464–481, 2023.

[87] Argonne National Laboratory, "D3 2016 toyota mirai." `https://www.anl.gov/taps/d3-2016-toyota-mirai`, 2016. Accessed: January 2024.

[88] Argonne National Laboratory, "Technology assessment of a fuel cell vehicle: 2017 toyota mirai," Technical Report, Argonne National Laboratory, 2018. Accessed: January 2024.

[89] S. Luciani and A. Tonoli, "Control strategy assessment for improving pem fuel cell system efficiency in fuel cell hybrid vehicles," *Energies*, vol. 15, no. 6, p. 2004, 2022.

[90] H.-B. Yuan, W.-J. Zou, S. Jung, and Y.-B. Kim, "Optimized rule-based energy management for a polymer electrolyte membrane fuel cell/battery hybrid power

system using a genetic algorithm," *International Journal of Hydrogen Energy*, vol. 47, no. 12, pp. 7932–7948, 2022.

[91] C. Du, S. Huang, Y. Jiang, D. Wu, and Y. Li, "Optimization of energy management strategy for fuel cell hybrid electric vehicles based on dynamic programming," *Energies*, vol. 15, no. 12, p. 4325, 2022.

[92] Y. Wang, S. G. Advani, and A. K. Prasad, "A comparison of rule-based and model predictive controller-based power management strategies for fuel cell/battery hybrid vehicles considering degradation," *International Journal of Hydrogen Energy*, vol. 45, no. 58, pp. 33948–33956, 2020.

[93] Y. Liu, J. Liu, D. Qin, G. Li, Z. Chen, and Y. Zhang, "Online energy management strategy of fuel cell hybrid electric vehicles based on rule learning," *Journal of Cleaner Production*, vol. 260, p. 121017, 2020.

[94] R. Bellman and E. Lee, "History and development of dynamic programming," *IEEE Control Systems Magazine*, vol. 4, no. 4, pp. 24–28, 1984.

[95] Y. Kim, M. Figueroa-Santos, N. Prakash, S. Baek, J. B. Siegel, and D. M. Rizzo, "Co-optimization of speed trajectory and power management for a fuel-cell/battery electric vehicle," *Applied Energy*, vol. 260, p. 114254, 2020.

[96] O. Sundstrom and L. Guzzella, "A generic dynamic programming matlab function," in *2009 IEEE control applications,(CCA) & intelligent control,(ISIC)*, pp. 1625–1630, IEEE, 2009.

[97] L. Xu, M. Ouyang, J. Li, and F. Yang, "Dynamic programming algorithm for

minimizing operating cost of a pem fuel cell vehicle," in *2012 IEEE international symposium on industrial electronics*, pp. 1490–1495, IEEE, 2012.

[98] H. Peng, J. Li, A. Thul, K. Deng, C. Ünlübayir, L. Löwenstein, and K. Hameyer, "A scalable, causal, adaptive rule-based energy management for fuel cell hybrid railway vehicles learned from results of dynamic programming," *Etransportation*, vol. 4, p. 100057, 2020.

[99] W. Zhou, L. Yang, Y. Cai, and T. Ying, "Dynamic programming for new energy vehicles based on their work modes part i: Electric vehicles and hybrid electric vehicles," *Journal of power sources*, vol. 406, pp. 151–166, 2018.

[100] Y. Wang, S. J. Moura, S. G. Advani, and A. K. Prasad, "Optimization of powerplant component size on board a fuel cell/battery hybrid bus for fuel economy and system durability," *International Journal of Hydrogen Energy*, vol. 44, no. 33, pp. 18283–18292, 2019.

[101] F. Miretti, D. Misul, and E. Spessa, "Dynaprog: Deterministic dynamic programming solver for finite horizon multi-stage decision problems," *SoftwareX*, vol. 14, p. 100690, 2021.

[102] A. Ferrara, M. Okoli, S. Jakubek, and C. Hametner, "Energy management of heavy-duty fuel cell electric vehicles: Model predictive control for fuel consumption and lifetime optimization," *IFAC-PapersOnLine*, vol. 53, no. 2, pp. 14205–14210, 2020.

[103] L. Haubensak, S. Strahl, J. Braun, and T. Faulwasser, "Towards real-time

capable optimal control for fuel cell vehicles using hierarchical economic mpc," *Applied Energy*, vol. 366, p. 123223, 2024.

[104] R. S. Sutton and A. G. Barto, *Reinforcement learning: An introduction*. MIT press, 2018.

[105] H. Wang, H. He, Y. Bai, and H. Yue, "Parameterized deep q-network based energy management with balanced energy economy and battery life for hybrid electric vehicles," *Applied energy*, vol. 320, p. 119270, 2022.

[106] J. Li, H. Wang, H. He, Z. Wei, Q. Yang, and P. Igic, "Battery optimal sizing under a synergistic framework with dqn-based power managements for the fuel cell hybrid powertrain," *IEEE Transactions on Transportation Electrification*, vol. 8, no. 1, pp. 36–47, 2021.

[107] C. Jia, K. Li, H. He, J. Zhou, J. Li, and Z. Wei, "Health-aware energy management strategy for fuel cell hybrid bus considering air-conditioning control based on td3 algorithm," *Energy*, vol. 283, p. 128462, 2023.

[108] G. Romano, "Energy management strategy of fuel cell hybrid electric vehicle based on dynamic programming and neural networks," master's thesis, Politecnico di Torino, 2021.

[109] D. Min, Z. Song, H. Chen, T. Wang, and T. Zhang, "Genetic algorithm optimized neural network based fuel cell hybrid electric vehicle energy management strategy under start-stop condition," *Applied Energy*, vol. 306, p. 118036, 2022.

[110] A. Manzotti, E. Quattrocchi, A. Curcio, S. C. Kwok, M. Santarelli, and

F. Ciucci, "Membraneless electrolyzers for the production of low-cost, high-purity green hydrogen: A techno-economic analysis," *Energy Conversion and Management*, vol. 254, p. 115156, 2022.

[111] U.S. Department of Energy, "Fuel cell system cost - 2017." `https://www.hydrogen.energy.gov/docs/hydrogenprogramlibraries/pdfs/17007_fuel_cell_system_cost_2017.pdf`, 2017. Accessed: 2024-04-01.

[112] M. Wentker, M. Greenwood, and J. Leker, "A bottom-up approach to lithium-ion battery cost modeling with a focus on cathode active materials," *Energies*, vol. 12, no. 3, p. 504, 2019.